

On the Evaluation of Regional Climate Model Simulations over South America

DISSERTATION

zur Erlangung des akademischen Grades

doctor rerum naturalium

(Dr. rer. nat.)

im Fach Physik

in der Spezialisierung Theoretische Physik

eingereicht an der

Mathematisch-Naturwissenschaftlichen Fakultät
der Humboldt-Universität zu Berlin

von

Stefan Lange

Präsident der Humboldt-Universität zu Berlin:
Prof. Dr. Jan-Hendrik Olbertz

Dekan der Mathematisch-Naturwissenschaftlichen Fakultät:
Prof. Dr. Elmar Kulke

Gutachter:

Prof. Dr. Dr. h.c. mult. Jürgen Kurths

Prof. Dr. Valerio Lucarini

Dr. Sin Chan Chou

Tag der mündlichen Prüfung:

13. Oktober 2015

To Jan Hendrik Feldhoff, who has left us much too early.

Abstract

This dissertation is about regional climate modeling over South America, the analysis of model sensitivities to cloud parameterizations, and the development of novel model evaluation techniques based on climate networks.

In the first part we focus on simulations with the COnsortium for Small scale MOdeling weather prediction model in CLimate Mode (COSMO-CLM) and provide the first thorough evaluation of this dynamical regional climate model over South America. We analyze the sensitivity of simulated tropical precipitation to the parametrization of cumulus convection versus subgrid-scale clouds in the radiation scheme and find them to be of similar magnitude. It is shown that model runs with different representations of subgrid-scale clouds in the radiation scheme produce substantially different cloud ice and liquid water contents. This impacts surface radiation budgets and in turn convection and precipitation. Considering all evaluated variables in synopsis, the model performs best with the nondefault cumulus convection scheme from the Integrated Forecasting System Cy33r1 and with the nondefault statistical scheme for subgrid-scale clouds in the radiation scheme. Despite several remaining deficiencies, such as a poor simulation of the diurnal cycle of precipitation, a severe underestimation of the frequency of heavy precipitation events, and a substantial austral summer warm bias over northern Argentina, this new setup considerably reduces long-standing model biases, which have plagued COSMO-CLM across tropical domains.

In the second part we introduce new performance metrics for climate model evaluation with respect to spatial covariabilities. In essence, these metrics consist of dissimilarity measures for climate networks constructed from simulations and observations. We develop both local and global network dissimilarity measures to facilitate the depiction of local dissimilarities in the form of bias maps as well as the aggregation of those local to global dissimilarities for the purposes of climate model intercomparison and ranking. To cover as wide a range of applications as possible, our measures are defined for directed as well as for undirected climate networks with and without edge weights and/or node weights. In order to demonstrate their capabilities, we employ them for a comparison of regional climate simulations with COSMO-CLM and with the STatistical Analogue Resampling Scheme (STARS) over South America. In the first of two such studies, simulations are both driven by and evaluated against reanalysis data, and the evaluation is carried out for different variables and seasons. We quantify model performances with the new bivariate metrics as well as with conventional univariate root-mean-square errors of climatological mean values and variances. While we mostly find agreement in model ranking according to the different metrics, there are also cases in which the network structure is reproduced better by a model which is less favored by a conventional measure or vice versa. This demonstrates the complementarity of the different model evaluation approaches. In the second study, we focus on monsoon season precipitation networks and evaluate the COSMO-CLM and STARS simulations against Tropical Rainfall Measuring Mission 3B42 V7 observations. We consider climate networks based on positive and based on negative rank correlations between rainfall anomaly time series at different locations as well as based on spatial synchronizations of extreme rain events. We find greater differences in model performance between network types for a fixed but arbitrary climate model than between climate models for a fixed but arbitrary network type and identify two sources of uncertainty in this respect. Firstly, interannual climate variability limits fidelity, particularly in the case of the extreme event network, and secondly, larger geographical link lengths render link misplacements more likely, most notably in the case of the anticorrelation network. Both contributions are quantified using suitable ensembles of bootstrap and random networks.

Zusammenfassung

Diese Dissertation beschäftigt sich mit regionaler Klimamodellierung über Südamerika, der Analyse von Modellsensitivitäten bezüglich Wolkenparametrisierungen und der Entwicklung neuer Methoden zur Modellevaluierung mithilfe von Klimanetzwerken.

Im ersten Teil konzentrieren wir uns auf das COnsortium for Small scale MOdeling model in CLimate Mode (COSMO-CLM) und führen die erste umfassende Evaluierung dieses regionalen Klimamodells über Südamerika durch. Es stellt sich heraus, dass die untersuchten Abhängigkeiten simulierter tropischer Niederschläge von den Parametrisierungen feuchter Konvektion sowie subgitterskaliger Wolken im Strahlungsschema von ähnlicher Größenordnung sind. Weiterhin führen Modellläufe mit verschiedenen Parametrisierungen subgitterskaliger Wolken im Strahlungsschema zu substanzial verschiedenen Wolkenwasser- und eisgehalten. Dies führt zu veränderten Strahlungsbudgets, was wiederum Veränderungen in konvektiver Aktivität und im Niederschlag nach sich zieht. Insgesamt erhält man die besten Simulationsergebnisse bei Verwendung des Konvektionsschemas des Integrated Forecasting System Cy33r1 und der statistischen Parametrisierung subgitterskaliger Wolken im Strahlungsschema. Mit der neuen Konfiguration verringern sich, trotz verbleibender Mängel wie einer ungenauen Wiedergabe des mittleren Niederschlagstagesgangs, einer beträchtlichen Unterschätzung der Häufigkeit von Starkniederschlagsereignissen und deutlich zu hoher Sommertemperaturen über Nordargentinien, die typischen und seit langer Zeit bestehenden systematischen Modellfehler des COSMO-CLM in tropischen Breiten.

Im zweiten Teil führen wir neue Metriken für die Evaluierung von Klimamodellen bezüglich räumlicher Kovariabilitäten ein. Im Kern bestehen diese Metriken aus Unterschiedsmaßen für den Vergleich von simulierten mit beobachteten Klimanetzwerken. Wir entwickeln lokale und globale Unterschiedsmaße zum Zwecke der Darstellung lokaler Unterschiede in Form von Fehlerkarten beziehungsweise der Rangordnung von Modellen durch Zusammenfassung lokaler zu globalen Netzwerkunterschieden. Zur Abdeckung eines möglichst breiten Anwendungsspektrums sind unsere Maße sowohl für gerichtete als auch für ungerichtete Netzwerke mit und ohne Kanten- und/oder Knotengewichten definiert. Zu Demonstrationszwecken verwenden wir die neuen Metriken für einen Vergleich regionaler Klimasimulationen mit COSMO-CLM und mit dem STatistical Analogue Resampling Scheme (STARS) über Südamerika. In der ersten zweier solcher Studien nutzen wir Reanalysedaten sowohl für den Antrieb der Simulationen als auch als Referenz für deren Evaluierung, die für verschiedene Variablen und Jahreszeiten durchgeführt wird. Die Leistungsfähigkeit der Modelle wird sowohl mit den neuen bivariaten Metriken als auch mithilfe von konventionellen univariaten mittleren quadratischen Abweichungen in klimatologischen Mittelwerten und Varianzen quantifiziert. Während die sich gemäß der verschiedenen Metriken ergebenden Modellrangfolgen weitestgehend übereinstimmen, finden wir auch Fälle, in denen die Netzwerkstruktur von einem Modell besser wiedergegeben wird, das gemäß einer konventionellen Metrik schlechter abschneidet oder umgekehrt, was die Komplementarität der verschiedenen Evaluierungsmethoden demonstriert. In der zweiten Studie konzentrieren wir uns auf Niederschlagsnetzwerke während der Monsunperiode und evaluieren die COSMO-CLM- und STARS-Simulationen gegen Beobachtungen der Tropical Rainfall Measuring Mission 3B42 V7. Wir konstruieren Klimanetzwerke basierend auf positiven und negativen räumlichen Rangkorrelationen zwischen Niederschlagsanomaliezeitreihen sowie basierend auf räumlichen Synchronisationen von Extremniederschlagsereignissen. Wir finden größere Wiedergabetreueunterschiede zwischen Netzwerktypen bei festem Modell als zwischen Modellen bei festem Netzwerktyp und identifizieren diesbezüglich zwei Unsicherheitsquellen. Zum einen begrenzt die natürliche jährliche Klimavariabilität die Wiedergabetreue, insbesondere im Fall des Extremereignisnetzwerks. Zum anderen führen größere geografische Kantenlängen zu einer erhöhten Wahrscheinlichkeit fehlerhafter Kantenanordnung, insbesondere im Fall des Antikorrelationsnetzwerks. Beide Beiträge quantifizieren wir mit geeigneten Ensembles von Bootstrap- und Zufallsnetzwerken.

Publications

This dissertation is largely based on results that were published in three peer-reviewed articles. Part I builds on

Lange, S., B. Rockel, J. Volkholz, and B. Bookhagen (2015a), *Regional climate model sensitivities to parametrizations of convection and non-precipitating subgrid-scale clouds over South America*, *Climate Dynamics*, 44(9–10):2839–2857, doi: 10.1007/s00382-014-2199-0,

and Part II is basically a blend of

Feldhoff, J. H., S. Lange, J. Volkholz, J. F. Donges, J. Kurths, and F.-W. Gerstengarbe (2015), *Complex networks for climate model evaluation with application to statistical versus dynamical modeling of South American climate*, *Climate Dynamics*, 44(5–6):1567–1581, doi: 10.1007/s00382-014-2182-9

and

Lange, S., J. F. Donges, J. Volkholz, and J. Kurths (2015b), *Local difference measures between complex networks for dynamical system model evaluation*, *PLoS ONE*, 10(4):e0118088, doi: 10.1371/journal.pone.0118088.

Contents

Preface	17
I Regional Climate Model Sensitivities to Parameterizations of Cumulus Convection and Stratiform Subgrid-Scale Clouds over South America	19
1 Introduction I	21
2 Numerical Atmospheric Modeling and Meteorological Reanalysis	25
3 Parameterization of Clouds	29
3.1 Parameterization of Stratiform Clouds	30
3.1.1 A Relative Humidity Scheme	31
3.1.2 A Statistical Scheme	33
3.2 Cloud Cover Fraction and Cloud Liquid Water and Ice Content	35
3.3 Parameterization of Cumuliform Clouds	37
3.3.1 The Tiedtke Scheme	38
3.3.2 The IFS Scheme	42
4 Dynamical Downscaling and CCLM	43
5 What We Talk about When We Talk about Climate Model Evaluation	45
6 The Sensitivity Study: Preliminaries	47
6.1 Study Design	47
6.2 The South American Climate	48
6.3 Observational Data	49
7 The Sensitivity Study: Results	51
7.1 Seasonal Mean Values	51
7.1.1 Precipitation	51
7.1.2 Total Cloud Cover	54
7.1.3 Surface Shortwave Net Radiation	55
7.1.4 Surface Longwave Net Radiation	56
7.1.5 2 m Temperature	57
7.1.6 Low-Level Circulation	58
7.2 Amazonia	59
7.2.1 Seasonal Cycles	59
7.2.2 Diurnal Cycles	61

7.2.3	Precipitation Intensities	62
7.2.4	Cloud Profiles	63
8	Summary and Discussion I	65
II	Complex Networks for Climate Model Evaluation with Application to Dynamical versus Statistical Regional Climate Modeling over South America	67
9	Introduction II	69
10	Network Theory	71
10.1	Climate Network Construction	71
10.2	Dissimilarity Measures for Climate Networks	73
10.2.1	Simple Graphs	73
10.2.2	Edge-Weighted Graphs	77
10.2.3	Node-Weighted Graphs	78
10.2.4	Directed Graphs	80
10.2.5	Normalization to Network Size	80
10.3	Random Network Models	81
11	Statistical Downscaling and STARS	83
12	Bivariate versus Univariate Climate Model Evaluation	85
12.1	Study Design	85
12.1.1	Climate Model Simulations	85
12.1.2	Network Construction	86
12.1.3	Bivariate and Univariate Model Error Measures	87
12.1.4	A Fairer Model Intercomparison with Bootstraps	88
12.2	Results	89
12.2.1	Bivariate Evaluation	89
12.2.2	Bivariate versus Univariate Evaluation	91
12.2.3	Sensitivity to Network Construction Parameters	91
13	Precipitation Climate Networks of the South American Monsoon System	93
13.1	Study Design	93
13.1.1	Precipitation Reference Data	93
13.1.2	Network Construction	95
13.2	Results	97
13.2.1	Network Topologies	97
13.2.2	Global Network Dissimilarities	100
13.2.3	Local Network Dissimilarities	104
14	Summary and Discussion II	107
	Bibliography	111

Figures and Tables

2.1	Grid Types Used for Numerical Atmospheric Modeling	27
3.1	Cumuliform versus Stratiform Clouds	31
3.2	Relative Humidity Subgrid-Scale Cloud Scheme Functions	32
3.3	What Is Subgrid-Scale Condensation	34
3.4	Cumulus Cloud Ensemble and Bulk Cloud Model	38
3.5	Cumulus Convection Skew-T Diagram	40
4.1	Coordinate System of CCLM	44
6.1	Model Setups of CCLM Sensitivity Study	47
6.2	CORDEX South America Domain for CCLM Sensitivity Study	48
6.3	LBA Flux Tower Specifications	50
7.1	Mean Precipitation versus TRMM	52
7.2	Mean Total Cloud Cover versus ISCCP	54
7.3	Mean Surface Net Shortwave Radiation versus SRB	55
7.4	Mean Surface Net Longwave Radiation versus SRB	56
7.5	Mean 2 m Temperature versus CRU	57
7.6	Mean 850 hPa Geopotential and Wind versus ERA-Interim	58
7.7	Seasonal Cycles at Flux Towers in DJF	60
7.8	Diurnal Cycles at Flux Towers in DJF	61
7.9	Precipitation Intensity Statistics over Amazonia in DJF	63
7.10	Vertical Cloud Profiles over Amazonia in DJF	64
9.1	What Is a Climate Network	70
10.1	Climate Network Types	72
10.2	Local Hamming Distance and Degree-Conditional Neighborhood Dissimilarity	75
10.3	Cumulative Distribution Function of Hypergeometric Distribution	76
11.1	How STARS Works	84
12.1	Simulation Domains for CCLM versus STARS Evaluation	86
12.2	Study Design of CCLM versus STARS Evaluation	88
12.3	Global Climate Network Dissimilarities for 2 m Temperature in DJF	90
12.4	Global Climate Network Dissimilarities for All Variables and Seasons	90
12.5	Bivariate versus Univariate Model Error Measures	92
13.1	Study Design of CCLM versus STARS Reevaluation	94

Figures and Tables

13.2	Precipitation Climatology of the South American Monsoon System	95
13.3	Extreme Event and Anomaly Time Series Preprocessing	96
13.4	Degrees	98
13.5	Link Length Statistics	99
13.6	RGB Color Coded Main Connectivity Patterns	101
13.7	Global Network Dissimilarities	102
13.8	Dependence of Link Misplacement Likelihood on Link Length	103
13.9	Local Network Dissimilarities	105

Acronyms

BAN	LBA flux tower at Bananal Island	50
CAPE	Convective Available Potential Energy	40
CAX	LBA flux tower at Caxiuanã	50
CCLM	COSMO model in CLimate Mode	21
CCLMb	CCLM bootstraps	89
CDF	Cumulative Distribution Function	75
CORDEX	COordinated Regional climate Downscaling EXperiment	22
COSMO	COnsortium for Small scale MOdeling	21
CRU	Climatic Research Unit	49
DJF	December-January-February	51
DND	Degree-conditional Neighborhood Dissimilarity	77
ECMWF	European Centre for Medium-range Weather Forecasts	21
EL	Equilibrium Level	40
ENIAC	Electronic Numerical Integrator And Computer	25
ER	Erdős-Rényi	81
ERA-I	ERA-Interim	85
ERA-Ib	ERA-Interim bootstraps	89
ES	Event Synchronization	96
ESp	simple graph with links representing most positive ES values	96
GCD	Global Correlation Distance	78
GCM	General Circulation Model	25
GHD	Global Hamming Distance	74
GS	grid-scale	29
IFS	Integrated Forecasting System	21
IPCC	Intergovernmental Panel on Climate Change	25
IR	IFS convection scheme + RH SGS cloud scheme in radiation scheme	47
IS	IFS convection scheme + Statistical SGS cloud scheme in radiation scheme	47
ISCCP	International Satellite Cloud Climatology Project	49
ITCZ	Inter Tropical Convergence Zone	48
JJA	June-July-August	51
K34	LBA flux tower at Manaus Km34	50
K67	LBA flux tower at Santarém Km67	50

Acronyms

LBA	Large-scale Biosphere-atmosphere experiment in Amazonia	50
LCD	Local Correlation Distance	77
LCL	Lifting Condensation Level	40
LFC	Level of Free Convection	40
LHD	Local Hamming Distance	74
NWP	Numerical Weather Prediction	25
PIK	Potsdam Institute for Climate Impact Research	17
PREC	precipitation	86
RCM	Regional Climate Model	21
RH	Relative Humidity	31
RJA	LBA flux tower at Reserva Jaru	50
RMSE	Root-Mean-Square Error	87
RMSLE	Root-Mean-Square Log Error	87
SACZ	South Atlantic Convergence Zone	48
SALLJ	South American Low-Level Jet	49
SAMS	South American Monsoon System	48
SERN	Spatially Embedded Random Network	81
SGS	subgrid-scale	29
SLP	sea level pressure	86
SR	Spearman Rank correlation coefficient	96
SRB	Surface Radiation Budget	49
SRn	simple graph with links representing most negative SR values	97
SRp	simple graph with links representing most positive SR values	97
STARS	STatistical Analogue Resampling Scheme	83
T2M	2 m temperature	86
TR	Tiedtke convection scheme + RH SGS cloud scheme in radiation scheme	47
TRMM	Tropical Rainfall Measuring Mission	49
TRMMb	TRMM bootstraps	94
TS	Tiedtke convection scheme + Statistical SGS cloud scheme in radiation scheme	47
VL	Viger-Latapy	81
Z500	500 hPa geopotential height	86

Preface

This dissertation integrates research results that were obtained in the framework of a graduate school project which had the initial objective to analyze sensitivities of the South American climate to changes of the regional vegetation as they have occurred, are occurring or may yet occur in response to regional climate and land-use changes. It was planned to quantify those sensitivities by running the regional climate model COSMO-CLM under various greenhouse gas and vegetation change scenarios.

Since it was initially unknown whether COSMO-CLM was actually able to simulate the South American climate with state-of-the-art fidelity, my first task was to provide a thorough evaluation of the model performance over this region. I found that, with a setup that worked well over Africa, the model produced severe precipitation biases over tropical South America, and it took me almost one year to find a model configuration that considerably alleviated the problem. Everything I learned during those months is presented in Pt. I.

Dealing with these difficulties I developed a strong interest in the general problem of climate model evaluation. Hence, in the following, I shifted my research focus to this topic. I began to cooperate with Jan H. Feldhoff on the development of new evaluation methods using complex network theory. The principle idea here was to employ networks as a tool to evaluate climate models with respect to the spatial covariabilities in the climate system. This work, which I sadly had to finish without Jan, is presented in Pt. II.

The initially planned climate sensitivity analysis will be realized in future research projects carried out at the Potsdam Institute for Climate Impact Research (PIK). For them, the results of this dissertation constitute a sound basis.

Since many people have inspired, guided and supported my research efforts over the past three years, results are presented by *us* in the following. Essential contributions by Jan H. Feldhoff are pointed out at the appropriate location.

I.

**Regional Climate Model Sensitivities to
Parameterizations of Cumulus Convection
and Stratiform Subgrid-Scale Clouds over
South America**

1. Introduction I

Since the beginning of numerical atmospheric modeling and despite many efforts, deficiencies in the representation of cloud processes in climate models have remained a source of much uncertainty in climate projections (Randall et al., 2003, 2007; Stocker et al., 2013). This is because clouds significantly influence thermodynamic and hydrological budgets, but need to be parameterized in mesoscale models (cf. Ch. 3; Tompkins, 2002).

A variable intimately related to clouds and of paramount importance for climate impact research is precipitation. In light of climate change, questions related to the hydrological cycle are: Where do humans have to adapt to changes in water availability (Parry et al., 2007; Liersch et al., 2012; Schewe et al., 2014)? Are extreme rain events going to be more frequent or intense (Marengo et al., 2009; Toreti et al., 2013; Fischer et al., 2013a)? How will ecosystems such as the Amazon rainforest respond to changes in precipitation patterns (Salazar et al., 2007; Cook et al., 2011; Warszawski et al., 2013)?

Deficiencies in parameterizations of cloud processes are reflected in precipitation biases, among other things. Particularly in the tropics, cumulus convection is an important process in this respect and its parameterization has received much attention (e.g. Betts and Jakob, 2002; Bechtold et al., 2004; Arakawa, 2004; Santos e Silva et al., 2012). However, since cumulus convection involves many coupled processes between the surface, the planetary boundary layer, and the free troposphere (Bechtold et al., 2004), the quality of its representation by climate models depends on several other model components as well.

One example of such a model component is the parameterization of radiative transfer as radiation influences energy budgets at the surface and throughout the atmosphere, and thus codetermines the amount of energy that is potentially available for cumulus convection. While radiative transfer impacts clouds, clouds also impact radiative transfer. This opens a feedback loop from clouds to clouds that shall be the main topic of the first part of this dissertation.

We are going to investigate how changes in the representation of stratiform nonprecipitating subgrid-scale clouds in the parameterization of radiative transfer influence cumulus convection and precipitation. Sensitivities of this kind have been found in earlier studies: In simulations with the Regional Climate Model (RCM) COSMO-CLM over Europe, Hohenegger et al. (2008) discovered a strong sensitivity of convective summertime rainfall to whether or not subgrid-scale clouds were considered in the radiative transfer calculations; in simulations with another RCM over North America, Xu and Small (2002) found a substantial sensitivity of monsoon season rainfall to the choice of the radiation scheme; and Morcrette et al. (2008) reported that a revision of the radiative transfer parameterization of the Integrated Forecasting System (IFS) of the European Centre for Medium-range Weather Forecasts (ECMWF) led to significant improvements of simulated cumulus convection over tropical continents.

We found similar sensitivities during our quest for a good COSMO-CLM setup for South America. The COSMO model in CLimate Mode (COSMO-CLM or CCLM; Rockel et al., 2008a) is the climate version of the CONSORTIUM for Small scale MODELing (COSMO) model (Baldauf et al., 2011), which is the operational numerical weather prediction model of the German Weather Service and other members of the COSMO consortium. The development of CCLM is steered by the CLM-Community, which has more than 50 member institutions from Europe, Asia, Africa, and

the Americas. CCLM has been extensively applied over European domains (e.g. Jaeger et al., 2008; Zahn and von Storch, 2008; Hohenegger et al., 2009; Davin and Seneviratne, 2012) but also over the Indian subcontinent (Dobler and Ahrens, 2010), over East Asia (Fischer et al., 2013b), and over Africa (Nikulin et al., 2012). The latter two applications were spurred by the COordinated Regional climate Downscaling EXperiment (CORDEX) initiative (Giorgi et al., 2009).

Previously, there had been three documented CCLM applications over South America: Böhm et al. (2003) had tested an early model version in combination with different soil hydrology parameterizations over the semi-arid Northeast region of Brazil; Rockel and Geyer (2008) had evaluated precipitation over the whole continent as simulated with the standard European model setup; and Wagner et al. (2012) had compared simulated sea level pressures, precipitation, and 2 m temperatures to observations over the southern part of the continent.

With our first CCLM simulation over South America, for which we used a model setup that worked well over Africa (Panitz et al., 2013), we essentially reproduced the bias pattern of strong underestimation/overestimation of rainfall over tropical continents/oceans that Rockel and Geyer (2008) had found in their study across tropical domains. We had hoped for a better result since in comparison to them, we did not just use a different model setup but also a later model version.

In order to improve simulation results, we first examined model sensitivities to the representation of land surface-atmosphere and ocean surface-atmosphere interactions. For example, we tried different values for the root depth of rainforest trees since that should impact the moisture available for evapotranspiration and in turn atmospheric humidity and precipitation; we experimented with different options for the calculation of the shortwave land surface albedo to check whether the induced changes in the surface energy balance would enhance precipitation over land; and we tuned the oceanic evaporation rate up and down, assuming that this would lead to precipitation changes over ocean and land. Yet all of those experiments led either to tiny overall improvements only or to reduced biases for one variable/area/time of the year at the expense of an increased bias for another variable/area/time of the year.

After we had ruled out the representation of atmosphere-surface interactions over land and ocean as very important for an accurate simulation of precipitation, we turned our attention to the atmosphere. Given that precipitation originates from clouds, it appeared natural to examine the representation of clouds in the model. It turned out that CCLM offers two options for the parameterizations of both subgrid-scale cumuliform and subgrid-scale stratiform clouds. Choosing the nondefault options in both cases led to the substantial improvements we had hoped for.

The details of this model sensitivity study are presented in the following. We include results for more variables than just precipitation to provide a first comprehensive evaluation of CCLM over South America. At the same time, to our knowledge, this is the first RCM sensitivity study comparing simulations with a relative humidity and a statistical scheme for the representation of subgrid-scale stratiform clouds in the parameterization of radiation in combination with different parameterizations of cumulus convection.

There has been a range of attempts to simulate the South American climate with other RCMs. While some studies focus on model evaluation (Nicolini et al., 2002; Seth and Rojas, 2003; Solman et al., 2013), others provide regional climate projections based on greenhouse gas emission or land-surface change scenario runs of general circulation models (Correia et al., 2008; Marengo et al., 2010, 2012a). We are going to relate our evaluation results to those obtained in these studies.

Part I is structured as follows. The paradigm of numerical climate modeling that CCLM adheres to is introduced in Ch. 2. In Ch. 3 we outline the idea of physical parameterization in the context of atmospheric modeling, and describe the subgrid-scale cloud parameterization schemes available in CCLM. In Ch. 4 we explain the concept of regional climate modeling and give a general description

of CCLM. Our understanding of the term climate model evaluation is stated in Ch. 5. In Ch. 6 we then delineate the design of our CCLM sensitivity-evaluation study over South America. Its results are presented in Ch. 7. We conclude with a summary and discussion in Ch. 8.

2. Numerical Atmospheric Modeling and Meteorological Reanalysis

The Intergovernmental Panel on Climate Change (IPCC) defines *climate* in a narrow sense as the statistical description of weather over long periods of time (Baede, 2001). In line with this definition, the numerical climate modeling paradigm we are concerned with in this part is the statistical analysis of long-term weather simulations with suitably extended *Numerical Weather Prediction* (NWP) models.

The basic ideas of numerical atmospheric modeling were developed about a century ago, yet they could only be put in practice with the advent of electronic digital computers in the 1940s, most notably with the completion of the Electronic Numerical Integrator And Computer (ENIAC) in 1945 (McCartney, 1999; Donner et al., 2011). The first long-range numerical simulation of the atmospheric general circulation was carried out by Phillips (1956) with a model that only had two vertical levels and 16×17 horizontal grid cells. It was a great success as a definite three-celled meridional circulation corresponding to the Hadley, Ferrel, and Polar cells appeared after one month's simulation. This seminal work thrilled the meteorological community and led to the development of several *Atmospheric General Circulation Models* (AGCMs or just GCMs as we are only concerned with the atmosphere and not with the ocean here) by research groups based in the US and the UK (Donner et al., 2011).

Due to limited computer resources and different objectives of the respective research communities, NWP and numerical climate modeling evolved separately in their early stages. Back then, weather forecasting was limited to short-term prediction over small areas with modelers focusing on the efficiency of their numerical methods, while climate models have been global from the outset with modelers concentrating on conservative numerical formulations and advanced atmospheric physics. Global weather forecasting began in the 1970s with the establishment of the ECMWF. Synergies between the disciplines became evident in the 1980s when numerical model formulations had converged and NWP groups recognized the need to adopt the more sophisticated representation of physical processes from GCMs. This development in connection with the ever increasing model complexity made it worthwhile to create unified atmospheric modeling systems, the first of which came into production use in the 1990s. The unified approach to NWP and numerical climate modeling is the standard nowadays; for a comprehensive review of the scientific and technical benefits of exploiting these synergies see Donner et al. (2011).

In the following we want to shed some light on the physical principles that are fundamental to state-of-the-art numerical atmospheric models. Shortly after Abbe (1901) recognized that meteorology is essentially the application of hydrodynamics and thermodynamics to the atmosphere, Bjerknes (1904) proposed a set of equations that to this day is considered the basis of an exact scientific description of atmospheric dynamics. Besides the thermodynamic equation of state for air, this set comprises the hydrodynamic equations of motion, the mass continuity equation, and the equation of energy conservation. Adding the budget equations for atmospheric humidity yields the following

basic dynamic equations,

$$\rho \frac{d\mathbf{v}}{dt} = -\nabla p + \rho \mathbf{g} - 2\rho \boldsymbol{\Omega} \times \mathbf{v}, \quad (2.1)$$

$$\frac{d\rho}{dt} = -\rho \nabla \cdot \mathbf{v}, \quad (2.2)$$

$$\rho \frac{dq_x}{dt} = -\nabla \cdot \mathbf{P}_x + S_x, \quad (2.3)$$

$$\rho \frac{de}{dt} = -p \nabla \cdot \mathbf{v} - \nabla \cdot \mathbf{F}, \quad (2.4)$$

with the material derivative $d/dt = \partial/\partial t + \mathbf{v} \cdot \nabla$, the total pressure p , the wind velocity vector \mathbf{v} , the total mass density of moist air ρ , the gravitational acceleration vector \mathbf{g} , and the angular velocity vector of the earth rotation $\boldsymbol{\Omega}$, that brings about the Coriolis force. The total mass density ρ has contributions from dry air and humidity in three phases. We use

$$x = \begin{cases} d & \text{for dry air,} \\ v & \text{for water vapor,} \\ l & \text{for liquid water,} \\ i & \text{for ice} \end{cases} \quad (2.5)$$

to indicate the different constituents. If ρ_x is the partial mass density of constituent x , then $q_x = \rho_x/\rho$ gives its mass concentration in the mixture, i.e. q_x is the specific humidity of water vapor, liquid water, ice for $x = v, l, i$, respectively, and $q_d + q_v + q_l + q_i = 1$. The total pressure $p = p_d + p_v$ is the sum of the partial pressures of dry air and water vapor. For later reference we note that based on the ideal gas law,

$$q_v = \frac{p_v R_d/R_v}{p - p_v(1 - R_d/R_v)} \quad (2.6)$$

relates q_v , p , and p_v , where the factor $R_d/R_v = 0.622$, the ratio of the specific gas constants of dry air and water vapor, accounts for the different molar masses of the two gases. In the moisture budgets (2.3), \mathbf{P}_x represents the sedimentation, i.e. precipitation flux of liquid water and ice associated with precipitation, and S_x denotes the mutual sources and sinks of humidity associated with phase transitions. The energy budget (2.4) reflects that changes of state due to atmospheric motion are approximately adiabatic, which implies that changes of the specific internal energy e of an air parcel are either due to work done by adiabatic compression/expansion or due to energy fluxes \mathbf{F} that are of neither hydrodynamic nor thermodynamic nature, namely those associated with radiation and precipitation. Note that the influence of viscosity is neglected in (2.1) and (2.4) by virtue of the high Reynolds number of atmospheric flows (Cushman-Roisin and Beckers, 2011).

Besides the basic dynamic equations (2.1) to (2.4), further physical laws and empirical relationships are needed to describe atmospheric processes such as radiative transfer, cloud microphysics or land surface-atmosphere interactions, and to finally obtain a closed system of equations that describes the dynamics of the atmosphere in some approximation. To facilitate a numerical integration of this system from some initial atmospheric state, the space-time continuum needs to be discretized. The natural spatial coordinates are those of the spherical or geographical coordinate system. Some models use pressure as their vertical coordinate. The kind of discretization of the hor-

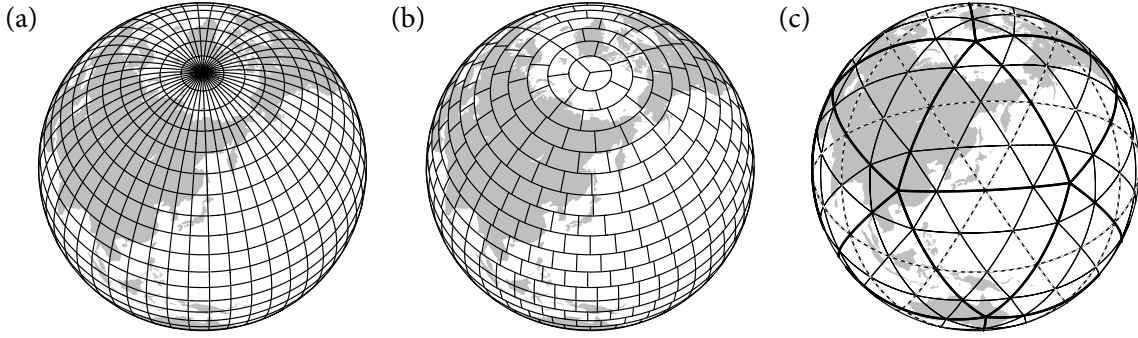


Figure 2.1.: Three grid types used for numerical atmospheric modeling. The pole singularities of the classical spherical grid (a) can be avoided using a reduced grid (b) or an icosahedral grid (c), for example (from Washington et al., 2009).

horizontal coordinates defines the grid type of the model; the classical equidistant sampling of latitude ϕ and longitude λ is just one possibility (cf. Fig. 2.1).

Since finer discretization implies greater computational cost, spatial and temporal model resolutions enhanced as computer resources grew. Classical GCMs operate at horizontal resolutions of the order of 100 km and thus resolve large-scale circulation patterns with horizontal sizes of the order of 1000 km. Since at this scale, vertical accelerations are small, it is common to neglect them in the vertical component of the Navier-Stokes equation (2.1). Further omission of the vertical component of the Coriolis force in view of the much stronger gravitation yields

$$\frac{\partial p}{\partial z} = -\rho g, \quad (2.7)$$

which signifies an atmosphere in hydrostatic balance; hence this is called the *hydrostatic approximation*. The atmospheric model applied in this study was designed for horizontal resolutions down to the order of 1 km. As vertical accelerations become important at those scales, the model does not rely on this approximation and hence is labeled *nonhydrostatic*.

Numerical atmospheric models are not just used to produce weather forecasts and climate simulations but also to improve the observational evidence of historical climate change. The approach known as *reanalysis* was pioneered by ECMWF and consists of a consistent meteorological data assimilation over an extended period, i.e. of running a NWP model while continuously nudging (von Storch et al., 2000), i.e. correcting it towards historical meteorological observations using a single data assimilation system throughout the reanalysis period. The result is a comprehensive four-dimensional picture of our atmosphere and as such it is the most accurate and consistent meteorological record we have. Care has to be taken inasmuch as reanalysis data quality varies from variable to variable and depends on the relative influences of model and observations (Kalnay et al., 1996; Trenberth et al., 2001; Marshall, 2002). In this thesis we use data from the latest reanalysis product of the ECMWF (Dee et al., 2011) as boundary conditions for dynamical downscaling (cf. Ch. 4), as input data for statistical resampling (cf. Ch. 11), and for several model evaluation purposes.

3. Parameterization of Clouds

The nonlinearity of the Navier-Stokes equation has fundamental implications for its discretization. As an example, let us consider the continuity equation of atmospheric water vapor [cf. Eq. (2.3)],

$$\frac{\partial(\rho q_v)}{\partial t} + \nabla \cdot (\rho q_v \mathbf{v}) = \rho e - \rho c, \quad (3.1)$$

where e from now on denotes the rate of evaporation and c is the rate of condensation, i.e. the right-hand side of (3.1) expresses water vapor sources and sinks. The left-hand side describes the passive advection of water vapor by the atmospheric flow.

Discretizing equations like (3.1) means tessellating the space-time continuum into polytopes, averaging every field over these polytopes and specifying the evolution equations of these discretized fields. Let us focus on the discretization of space to see what it does to (3.1). Since differentiation is a linear operation, grid-volume averaging of (3.1) yields

$$\frac{\partial \langle \rho q_v \rangle}{\partial t} + \nabla \cdot \langle \rho q_v \mathbf{v} \rangle = \langle \rho e \rangle - \langle \rho c \rangle, \quad (3.2)$$

with $\langle \cdot \rangle$ denoting the average over some fixed but arbitrary grid volume. The most interesting part of (3.2) is the nonlinear term $\nabla \cdot \langle \rho q_v \mathbf{v} \rangle$. Following Reynolds (1894), we decompose any field f into its grid-scale (GS) average and subgrid-scale (SGS) fluctuations around this average, i.e. $f = \langle f \rangle + f'$. Then $\langle f' \rangle = 0$ and it is easy to see that for a product of two quantities, $\langle fg \rangle = \langle f \rangle \langle g \rangle + \langle f' g' \rangle$ holds. Under the usual assumption that SGS fluctuations of ρ are negligible, the grid-volume average of q_v evolves according to

$$\frac{\partial(\langle \rho \rangle \langle q_v \rangle)}{\partial t} + \nabla \cdot (\langle \rho \rangle \langle q_v \rangle \langle \mathbf{v} \rangle) = \langle \rho \rangle \langle e \rangle - \langle \rho \rangle \langle c \rangle - \nabla \cdot (\langle \rho \rangle \langle q'_v \mathbf{v}' \rangle). \quad (3.3)$$

The equations of motion of $\langle q_v \rangle$ and q_v differ by the last term on the right-hand side of (3.3), which describes the transport of moisture by SGS eddies. While the horizontal components of this transport only become relevant at the kilometer scale (Schättler et al., 2013), divergences of the vertical eddy covariances of wind and advected quantities like specific humidity are too fundamental to be neglected at typical horizontal resolutions of regional and global climate models (Donner et al., 2011), which range from a few to hundreds of kilometers. They are essential for the vertical stabilization of the atmosphere and closely related to the formation of clouds.

Unfortunately, statistics of unresolved dynamics like $\langle q'_v \mathbf{v}' \rangle$ cannot be directly derived from first principles (Donner et al., 2011). In lieu thereof, one tries to devise conceptual models of the relevant SGS processes with the objective to express the desired statistics in terms of GS quantities like $\langle q_v \rangle$ and $\langle \mathbf{v} \rangle$ and thereby to close the system of evolution equations at the grid scale.¹ The most prominent examples of such models are *turbulence* and *convection* schemes, which are supposed to represent the quasi-random small-scale motions and the quasi-organized motions at the larger unresolved scales, respectively (Mironov, 2009).

¹This part of a parameterization scheme is called *closure*.

3. Parameterization of Clouds

The numerical solution of the hydrodynamic and thermodynamic equations at the grid scale, such as (3.3) without the SGS eddy covariance term, is the job of the *dynamical core* of an atmospheric model (Donner et al., 2011). All other model parts are grouped under the umbrella term *model physics* or *physical parameterizations* or just *parameterizations*. This includes schemes of land-atmosphere interaction, cloud microphysics, and radiative transfer. Parameterizations of unresolved hydrodynamics and thermodynamics are special in the sense that they become less important as model grid resolution increases. For example, the parameterization of deep convection becomes superfluous at the kilometer scale (Hohenegger et al., 2008).

Very important is the parameterization of processes related to the occurrence of clouds, whose horizontal size ranges from meters for fragmentary small cumuli (Koren et al., 2008) to thousands of kilometers for cloud sheets covering the mid-latitude oceans (Wood and Field, 2011). Clouds are an integral part of the climate system. They strongly interact with both shortwave and longwave radiation, they produce precipitation, and they are key players in the vertical transport of energy, moisture, and momentum (de Rooy et al., 2013). At the same time, they are overwhelmingly complicated (Randall et al., 2003): Virtually all clouds are turbulent; the hydrometeors that make up clouds range from microns to millimeters in size and intricate microphysical processes control their formation, interaction, and sedimentation; complicated hydrodynamics and thermodynamics are associated with the occurrence of vertically extended clouds; different kinds of clouds may coexist in an atmospheric column, with frequent interactions occurring between them; the interplay of clouds with radiation depends on the geometry of a cloud field and its hydrometeorological composition; and frequently clouds form mesoscale or even large-scale dynamical systems that interact with the general circulation.

In consideration of these various cloud-related interactions between microphysics, multiscale dynamics, and radiative transfer, Arakawa (2004) expressed the need to conceptually integrate the respective processes and scales into one unified modeling framework. He did so in light of about 40 years of unintegrated cloud parameterization research which, despite great efforts and advances, was not able to significantly reduce the uncertainty around climate projections that stems from the representation of cloud processes in GCMs (Randall et al., 2003). Yet to date, unified cloud parameterizations, let alone unified model physics, have remained elusive. Like most atmospheric models, CCLM features independent parameterizations of SGS *cumuliform* (vertically developed) and SGS *stratiform* (horizontally developed) clouds (Fig. 3.1). In the remainder of this chapter, we describe the two schemes available in CCLM per SGS cloud type. This shall not only prepare the reader for the reception of the results of our model evaluation/sensitivity study but it shall also convey the conceptual complexity of the cloud parameterization problem.

3.1. Parameterization of Stratiform Clouds

Randall et al. (2003) define stratiform clouds as those clouds that are neutrally buoyant in an area-averaged sense. In CCLM, it is assumed that precipitating stratiform clouds are covered by the GS dynamics and microphysics; SGS stratiform clouds are thus treated as nonprecipitating, which significantly simplifies their parameterization. In our model evaluation study we analyze the sensitivity of simulation results to the representation of SGS clouds in the radiative transfer scheme by Ritter and Geleyn (1992). For every grid volume, this scheme requires values of the cloud cover fraction C and of the specific cloud liquid water and ice contents, q_1^{rad} and q_i^{rad} , respectively (cf. Sec. 3.2). The job of the parameterization of SGS stratiform clouds is to provide their contributions to C , q_1^{rad} , and q_i^{rad} .

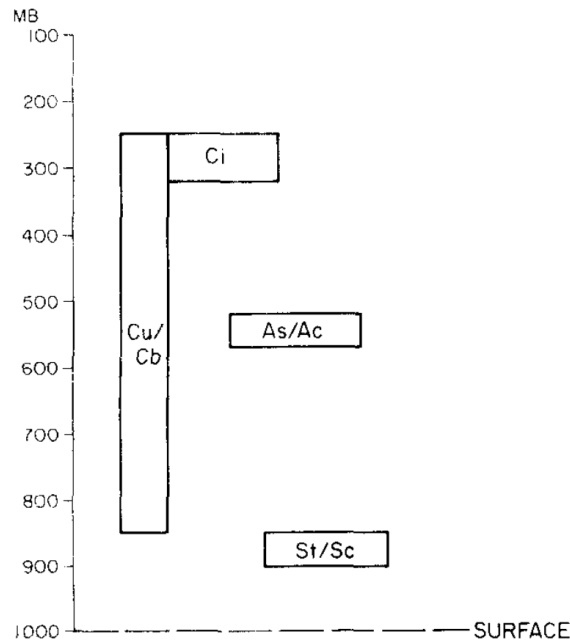


Figure 3.1.: Schematic representation of the horizontal and vertical cloud distribution in an atmospheric model with distinction between cumuliform (Cu/Cb) and stratiform (Ci, As/Ac, St/Sc) clouds (from Slingo, 1987). While cumuliform clouds extend across several model layers, stratiform clouds occupy individual layers only.

SGS clouds exist due to fluctuations of the water vapor saturation deficit $q_{\text{def}} = q_v + q_l + q_i - q_v^*$ within a given grid volume, where q_v^* is the saturation specific humidity of water vapor. For the sake of simplicity, it is commonly assumed that q_{def} only varies horizontally inside a grid volume, which requires a sufficiently high vertical resolution. Provided there are enough cloud condensation nuclei, the cloud cover fraction of a grid volume is equal to the fraction of the grid volume with positive values of q_{def} . Accordingly, any parameterization of stratiform SGS clouds is based on assumptions about the distribution of q_{def} within a given grid volume. Traditionally, there have been two approaches to the problem, that differ in making these assumptions either implicitly or explicitly (Tompkins, 2002). The older class of schemes simply expresses the stratiform cloud cover fraction in terms of the GS relative humidity (Smagorinsky, 1960; Slingo, 1987). The more sophisticated approach is explicit about the assumed q_{def} distribution and is closed by determining the moments of this distribution (Sommeria and Deardorff, 1977). One parameterization of each type is implemented in CCLM and described in the following.

3.1.1. A Relative Humidity Scheme

Relative Humidity (RH) schemes are based on the idea that SGS condensation starts before the GS relative humidity has reached 100% and that the cloud cover fraction can be expressed in terms of this GS relative humidity (Sundqvist, 1978). Let C^{str} be the cloud cover fraction due to stratiform clouds. RH schemes postulate that C^{str} increases monotonically from zero at some critical GS relative humidity $U_c < 1$ to one at GS saturation. Tompkins (2002) points out that this is equivalent to the assumption of a certain fixed variability of q_{def} in all grid volumes across the globe. As he goes

3. Parameterization of Clouds

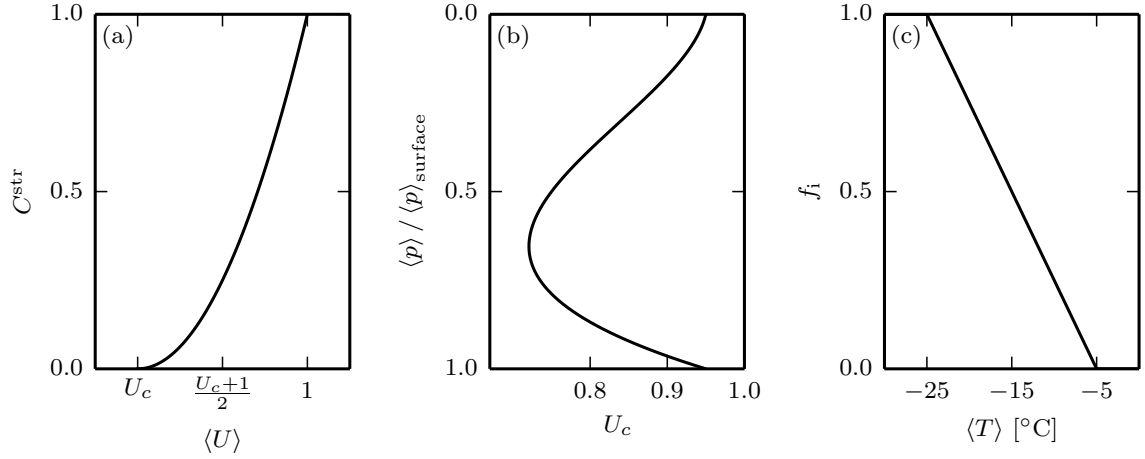


Figure 3.2.: Some functions used in the RH scheme of CCLM. (a) Functional relationship between SGS stratiform cloud cover $C^{\text{str}} < 1$ and GS relative humidity $\langle U \rangle < 1$. (b) Vertical profile of the critical relative humidity U_c with the height given by the sigma vertical coordinate defined as the pressure p normalized by its surface value p_{surface} . (c) Temperature dependence of the cloud ice fraction f_i .

on to state that grid volumes with 80% relative humidity undergoing deep convection are likely to have different cloud characteristics than grid volumes with 80% relative humidity in a frontal stratus cloud, this clearly is an oversimplification of reality. In the following we outline how CCLM diagnoses the stratiform cloud cover fraction C^{str} and the specific stratiform cloud water and ice contents q_l^{str} and q_i^{str} , which represent contributions from both GS and SGS stratiform clouds.

If there are GS clouds, i.e. if $\langle q_l \rangle > 0$ or $\langle q_i \rangle > 0$, then C^{str} is set to one. Otherwise, a fractional stratiform cloud cover is diagnosed according to

$$C^{\text{str}} = \min^2 \left\{ 1, \max \left\{ 0, \frac{\langle U \rangle - U_c}{1 - U_c} \right\} \right\}, \quad (3.4)$$

where $\langle U \rangle = \langle q_v \rangle / \langle q_v^* \rangle$ is the GS relative humidity [cf. Fig. 3.2(a)]. SGS condensation begins at the critical value U_c , which depends on height as depicted in Fig. 3.2(b). The saturation specific humidity $\langle q_v^* \rangle$ is calculated under the assumption that mixed-phase clouds exist for temperatures between -25°C and -5°C . Therefore, in this temperature range, $\langle q_v^* \rangle$ is a weighted sum of the saturation specific humidities $\langle q_{vl}^* \rangle$ of *warm clouds* (pure liquid water clouds) and $\langle q_{vi}^* \rangle$ of *cold clouds* (pure ice clouds),

$$\langle q_v^* \rangle = (1 - f_i) \langle q_{vl}^* \rangle + f_i \langle q_{vi}^* \rangle. \quad (3.5)$$

The temperature dependence of the ice fraction f_i is depicted in Fig. 3.2(c). On the basis of (2.6), the saturation specific humidities of warm and cold clouds are calculated according to

$$\langle q_{vx}^* \rangle = \frac{\langle p_{vx}^* \rangle R_d / R_v}{\langle p \rangle - \langle p_{vx}^* \rangle (1 - R_d / R_v)}, \quad (3.6)$$

where p_{vx}^* denotes the saturation vapor pressure over a plane surface of water ($x = l$) and ice ($x = i$), which is calculated using the Magnus approximation (Tetens, 1930; Murray, 1967).

The specific liquid water and ice contents of stratiform clouds are estimated according to

$$q_x^{\text{str}} = \max \left\{ \frac{\langle q_x \rangle}{2}, 0.005 f_x \langle q_v^* \rangle \right\}, \quad (3.7)$$

where we defined $f_1 = 1 - f_i$. Note that q_x^{str} are the in-cloud liquid water and ice contents; to obtain the respective grid volume average specific humidities, q_x^{str} needs to be multiplied by C^{str} .

In order to understand why $q_x^{\text{str}} < \langle q_x \rangle$ in the case of GS condensation, it is essential to know how q_x^{str} is used in the radiative transfer scheme. The latter is based on the Beer-Lambert law, according to which the intensity of light is exponentially attenuated as it travels through homogeneous materials. Given a vertically homogeneous grid volume of height Δz , the presence of cloud liquid water or ice reduces the intensity of vertically incident radiation by a factor of $\exp(-\epsilon_x(\lambda) q_x \Delta z)$ at wavelength λ and for each type x of hydrometeors. Horizontal averaging of this factor yields

$$\exp(-\epsilon_x \langle q_x \rangle \Delta z) \langle \exp(-\epsilon_x q'_x \Delta z) \rangle \text{ or, equivalently,} \quad (3.8)$$

$$\exp(-\epsilon_x \alpha \langle q_x \rangle \Delta z). \quad (3.9)$$

If $q'_x \neq 0$, then the second factor in (3.8) is greater than one because $\langle q'_x \rangle = 0$. This implies that α in (3.9) is less than one because ϵ_x , $\langle q_x \rangle$, and Δz are all nonnegative. The factor $\frac{1}{2}$ in (3.7) is one possible choice for the value of α . We see that it represents a nonlinear effect of the SGS variability of q_x on the optical properties of GS stratiform clouds.

In the absence of GS condensation, the RH scheme diagnoses q_x^{str} as proportional to (5‰ of) the GS saturation specific humidity, which is a clear idealization of reality, but experience shows that with the right tuning of the factor of proportionality, realistic values of planetary albedo and outgoing longwave radiation can be obtained (Ritter and Geleyn, 1992).

In a final step, the RH scheme accounts for the special case of thin high cirrus clouds (Görsdorf et al., 2011). If the stratiform cloud liquid water and ice content calculation yields values of $q_1^{\text{str}} = 0$ and $0 < q_i^{\text{str}} < 8 \times 10^{-6}$, then the value of the cloud cover fraction C^{str} from (3.4) is reduced by the factor

$$\min \left\{ 1, \max \left\{ 0, \frac{7 + \log_{10} q_i^{\text{str}}}{1 + \log_{10} 8} \right\} \right\}. \quad (3.10)$$

3.1.2. A Statistical Scheme

When CCLM is run with its statistical parameterization of SGS stratiform clouds, then this parameterization in fact pertains to warm SGS stratiform clouds only, i.e. cold stratiform clouds are considered to be present either at grid scale (if $\langle q_i \rangle > 0$, then $C^{\text{str}} = 1$) or not at all ($C^{\text{str}} = 0$ otherwise).

Warm SGS stratiform clouds are parameterized as proposed by Sommeria and Deardorff (1977). This scheme is based on the assumptions that in warm nonprecipitating clouds, (i) the air is saturated with water vapor, i.e. the relative humidity is at exactly 100% with respect to the saturation vapor pressure over a plane surface of water, (ii) water droplets are carried along with air parcels, which (iii) move adiabatically, and (iv) the entire system is always in thermodynamic equilibrium, which implies that air and liquid water have the same temperature. The corresponding thermodynamic reference process is the reversible water saturation adiabat (Saunders, 1957; Betts, 1973). The two fundamental quantities that are conserved during this process are the *total water specific humidity* $q_w = q_v + q_l$ and the *liquid water potential temperature* θ_l , which can be approximated by

3. Parameterization of Clouds

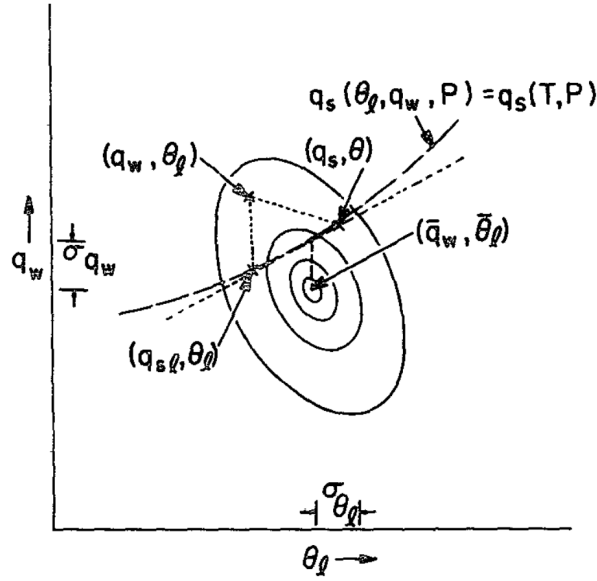


Figure 3.3.: Schematic diagram of the distribution of the variables q_w and θ_1 inside a given grid volume (from Sommeria and Deardorff, 1977). The saturation specific humidity q_w^* is represented by the symbol q_s in this diagram.

$$\theta_1 \approx \theta - \frac{\theta}{T} \frac{L}{c_p} q_1 \quad (3.11)$$

to an accuracy of a few percent (Betts, 1973). Here, L is the latent heat of vaporization, c_p is the specific heat capacity of dry air at constant pressure, and $\theta = T(p_0/p)^\kappa$ is the *potential temperature*, which, with some fixed reference pressure p_0 and the Poisson constant $\kappa = R_d/c_p = 0.285$, is approximately conserved during dry adiabatic motion of moist air.

In their model of warm SGS condensation, Sommeria and Deardorff (1977) assume that inside a given grid volume, q_w and θ_1 are joint-normally distributed around the GS values $\langle q_w \rangle$, $\langle \theta_1 \rangle$ with variances $\sigma_{q_w}^2 = \langle q_w' q_w' \rangle$, $\sigma_{\theta_1}^2 = \langle \theta_1' \theta_1' \rangle$ and covariance $\langle q_w' \theta_1' \rangle$ (cf. Fig. 3.3). They state that this assumption implies that those air parcels existing within any given grid volume have had complicated past trajectories and have not selectively been subjected to rapid changes in q_w and θ_1 . The Gaussian assumption is applied to the conservative variables instead of to q_1 and T since large changes in these latter variables occur following a parcel within clouds and near cloud edges.

Based on the SGS distribution of q_w and θ_1 and using various thermodynamic identities, Sommeria and Deardorff (1977) derive approximate expressions for the stratiform cloud cover fraction and the stratiform cloud liquid water content,

$$C^{\text{str}} = \frac{1}{2} \left(1 + \frac{Q_d}{Q_c} \right), \quad (3.12)$$

$$C^{\text{str}} q_1^{\text{str}} = \frac{\sigma_d}{\beta_1} \begin{cases} 0 & \text{for } Q_d \leq -Q_c, \\ (Q_d/Q_c + 1)^2/4 & \text{for } -Q_c < Q_d < Q_c, \\ Q_d & \text{for } Q_c \leq Q_d, \end{cases} \quad (3.13)$$

where $Q_c = 1.6$ is the critical value of Q_d . Along their way to these results, the authors define

$$T_1 = T - \frac{L}{c_p} q_1 \approx \frac{T}{\theta} \theta_1, \quad (3.14)$$

$$q_1^* = q_{v1}^*(T_1, p), \quad (3.15)$$

$$\beta_1 = 1 + \frac{L^2 \langle q_1^* \rangle}{R_v c_p \langle T_1 \rangle^2}, \quad (3.16)$$

$$\sigma_d^2 = \langle q'_w q'_w \rangle + \langle q_1^{*'} q_1^{*'} \rangle - 2 \langle q'_w q_1^{*'} \rangle = \langle (q'_w - q_1^{*'})^2 \rangle, \quad (3.17)$$

$$Q_d = \frac{\langle q_w \rangle - \langle q_1^* \rangle}{\sigma_d}. \quad (3.18)$$

For typical values of q_1 in clouds, the *liquid water temperature* T_1 is a few Kelvin lower than T . Note that T_1 is not the temperature of the cloud droplets since these are assumed to be in equilibrium with their environment; Sommeria and Deardorff (1977) only chose the name in analogy to that of θ_1 . The quantity $\langle q_1^* \rangle$ is calculated using (3.6) with $\langle T_1 \rangle$ in place of $\langle T \rangle$ in the Magnus formula for $\langle p_{v1}^* \rangle$. The core variable of the scheme is Q_d , the normalized deviation from mean saturation. To close the system of equations, the standard deviation σ_d of $q_w - q_1^*$ in the grid volume needs to be estimated, which is done in the turbulence parameterization. This linkage of optical SGS cloud properties to the turbulent SGS dynamics promises a representation of clouds that is more physically consistent than with the RH scheme.

It is interesting to note that at GS saturation, when $\langle q_w \rangle = \langle q_{v1}^* \rangle$ and the RH scheme diagnoses $C^{\text{str}} = 1$, the statistical scheme produces a typical value of $C^{\text{str}} = 0.65$ since SGS fluctuations of humidity and temperature leave a fraction of the grid volume unsaturated (Sommeria and Deardorff, 1977). The typical value is greater than 0.5 [cf. Eq. (3.12)] because when $\langle q_w \rangle = \langle q_{v1}^* \rangle$, then typically $\langle q_1 \rangle > 0$ due to SGS variability, which implies $\langle T_1 \rangle < \langle T \rangle$ and $\langle q_1^* \rangle < \langle q_{v1}^* \rangle$, i.e. $Q_d > 0$.

3.2. Cloud Cover Fraction and Cloud Liquid Water and Ice Content

The radiative effect of a cloud depends on the cloud extent as well as on the concentration and on the size distribution of its hydrometeors (Stephens, 1979). The radiative transfer scheme by Ritter and Geleyn (1992) simplifies the latter aspect by introducing effective cloud droplet and ice crystal sizes, which are inferred from the specific cloud liquid water content q_1^{rad} and the specific cloud ice content q_i^{rad} , respectively. Accordingly, the scheme requires the input of q_1^{rad} , q_i^{rad} and of the cloud cover fraction C of every grid volume. The three quantities are to represent contributions from both cumuliform and stratiform clouds as the two types may coexist in a grid volume.

Symmetric contributions by cumuliform and stratiform clouds yield

$$C = C^{\text{cum}} + (1 - C^{\text{cum}}) C^{\text{str}} \quad (3.19)$$

$$= C^{\text{cum}} + C^{\text{str}} - C^{\text{cum}} C^{\text{str}} = C^{\text{str}} + (1 - C^{\text{str}}) C^{\text{cum}}. \quad (3.20)$$

The form of (3.19) and (3.20) reflects that stratiform clouds can only overcast that fraction of a grid volume which is not occupied by cumuliform clouds and vice versa. The contribution of cumuliform clouds to the cloud cover fraction is assumed to be proportional to an effective cumulus cloud height,

3. Parameterization of Clouds

$$C^{\text{cum}} = \min \left\{ 1, \max \left\{ 0.05, 0.35 \frac{z_{\text{top}} - z_{\text{bas}}}{5000 \text{ m}} \right\} \right\}, \quad (3.21)$$

where z_{bas} and z_{top} are the cloud base and top heights, respectively. A relationship between the horizontal and the vertical extent of cumulus clouds is suggested by observations (Plank, 1969). The cumulus cloud cover fraction (3.21) is assigned to all layers between z_{bas} and z_{top} . Cumulus anvils are diagnosed if the temperature increases at the cloud top; in this case, C^{cum} is doubled in the top level layer. The values of z_{bas} and z_{top} are estimated in the cumulus convection scheme (cf. Sec. 3.3).

While C^{cum} is diagnosed according to (3.21) irrespective of the chosen SGS stratiform cloud scheme, the diagnosis of the liquid water and ice contents of cumulus clouds depends on this choice in CCLM, given that

$$q_1^{\text{rad}} = C^{\text{cum}} q_1^{\text{cum}} + (1 - C^{\text{cum}}) C^{\text{str}} q_1^{\text{str}}, \quad (3.22)$$

is the cloud liquid water content seen by the radiation scheme, where

$$q_1^{\text{cum}} = 0.01 \begin{cases} (1 - f_i) \langle q_v^* \rangle & \text{with the RH scheme,} \\ \begin{cases} \langle q_{\text{vl}}^* \rangle & \text{for } \langle T \rangle \geq 0 \\ \langle q_{\text{vi}}^* \rangle & \text{for } \langle T \rangle < 0 \end{cases} & \text{with the statistical scheme.} \end{cases} \quad (3.23)$$

We note that the possibility of mixed-phase clouds and supercooled cloud droplets is not taken into account with the statistical scheme [cf. Fig. 3.2(c)]. Note also the formal analogy between (3.23) and the corresponding formula (3.7) for stratiform clouds in the RH scheme. The cloud ice content seen by the radiation scheme is

$$q_i^{\text{rad}} = \begin{cases} C^{\text{cum}} q_i^{\text{cum}} + (1 - C^{\text{cum}}) C^{\text{str}} q_i^{\text{str}} & \text{with the RH scheme,} \\ \langle q_i \rangle & \text{with the statistical scheme,} \end{cases} \quad (3.24)$$

where

$$q_i^{\text{cum}} = 0.01 f_i \langle q_v^* \rangle. \quad (3.25)$$

A variable that is relatively easy to measure and therefore frequently validated is C^{tot} , the *total cloud cover* of a grid column, i.e. the area fraction of the column that appears overcast when it is viewed from above or below. Clouds from all layers contribute to C^{tot} ; if k is the layer index, then

$$C^{\text{tot}} = 1 - (1 - C_1) \prod_{k \geq 2} \frac{1 - \max \{ C_k, C_{k-1} \}}{1 - C_{k-1}} \quad (3.26)$$

is used to diagnose C^{tot} in CCLM. This formula yields $C^{\text{tot}} = \max_k C_k$ if C_k is constant or has one local maximum only. In the case of multiple local maxima the result is somewhat more complex. The assumptions behind (3.26) are that (i) a positive cloud cover fraction in adjacent layers k , $k - 1$ indicates clouds that vertically extend across those layers, hence a maximum overlap is assumed for C_k , C_{k-1} , while (ii) a vanishing cloud cover fraction in some layer k^* indicates independent clouds above and below that layer, hence a random overlap is assumed for $C_{k < k^*}$, $C_{k > k^*}$, i.e. the clear-sky

fraction below cloudy layers $\hat{k} < k^* < \check{k}$ is set equal to $(1 - C_{\hat{k}})(1 - C_{\check{k}})$. This cloud geometry concept is used in the Ritter and Geleyn (1992) scheme as well, so (3.26) is consistent with the radiative transfer calculations in CCLM.

3.3. Parameterization of Cumuliform Clouds

Cumuliform clouds differ from stratiform clouds by their pronounced vertical development. Their presence is associated with strong vertical eddy transports of moisture, energy, and momentum. They often generate precipitation. The parameterization of cumuliform clouds is therefore a greater challenge than that of stratiform clouds. It has been regarded as perhaps the most difficult parameterization problem in numerical atmospheric modeling (Donner et al., 2011). Arakawa (2004) defines cumulus parameterization as the problem of formulating the statistical effects of moist convection to obtain a closed system for predicting weather and climate. This definition reflects that cumuliform clouds form as a result of moist convection, i.e. of atmospheric convection in which the phase changes of water play a considerable role. Consequently, *cumulus parameterization schemes* are also referred to as *convection parameterization schemes*.

The classical objectives of such schemes are to provide the vertical profiles of heating/cooling and drying/moistening tendencies as well as the surface precipitation generated by SGS cumulus convection. These objectives can most easily be met, albeit with arguable precision, by so-called moist-convective adjustment schemes, such as that proposed by Manabe et al. (1965). Based on the GS relative humidity $\langle U \rangle$ and the GS temperature lapse rate $\langle \Gamma \rangle$, this scheme diagnoses moist convection to occur where the air is supersaturated ($\langle U \rangle > 100\%$) and conditionally unstable ($\langle \Gamma \rangle > \langle \Gamma_m \rangle$, where Γ_m is the moist-adiabatic temperature lapse rate). If these conditions are met, then the scheme adjusts $\langle T \rangle$ and $\langle q_v \rangle$ such that $\langle U \rangle = 100\%$ and $\langle \Gamma \rangle = \langle \Gamma_m \rangle$, and all the water condensed by this process precipitates instantaneously (Manabe et al., 1965; Arakawa, 2004).

The so-called mass-flux schemes are of greater sophistication. These schemes include a cloud model, which is closed by linking the grid-column average cloud-base mass flux to the GS environment in one way or another. The two convection schemes implemented in CCLM are of this kind. Conceptually, they are both based on the cloud model developed by Yanai et al. (1973) in a diagnostic study of tropical cumulus convection. This cloud model is made for horizontal grid resolutions of some tens of kilometers, at which grid volumes with occurring cumulus convection are populated by an ensemble of cumulus clouds, which have a common base height but different depths [cf. Fig. 3.4(a)].

The traditional simplified picture of cumulus convection is that it organizes itself into narrow, intense saturated updrafts that are embedded in a slowly subsiding environment, and that air is exchanged turbulently at the cloud edges (Bjerknes, 1938; Randall et al., 2003). With this picture in mind, Yanai et al. (1973) sketched a cumulus convection scheme, in which every cloud of the ensemble has its individual vertical profile of humidity, dry and moist static energy, vertical velocity, and of the rates of condensation, precipitation, and turbulent exchange with environmental air through entrainment and detrainment, while the ambient air is characterized by a single vertical profile of humidity, dry and moist static energy, and vertical velocity. With their scheme, Yanai et al. (1973) wanted to retrieve bulk properties of tropical cumulus cloud clusters from observed large-scale budgets of heat and moisture but it turned out that the scheme led to a system of equations with too many unknowns. To make the problem tractable, Yanai et al. (1973) introduced some simplifications, such as a restriction of detrainment to the cloud tops, and they replaced the cloud ensemble by representative bulk quantities [cf. Fig. 3.4(b)]. The bulk cloud properties they retrieved with this

3. Parameterization of Clouds

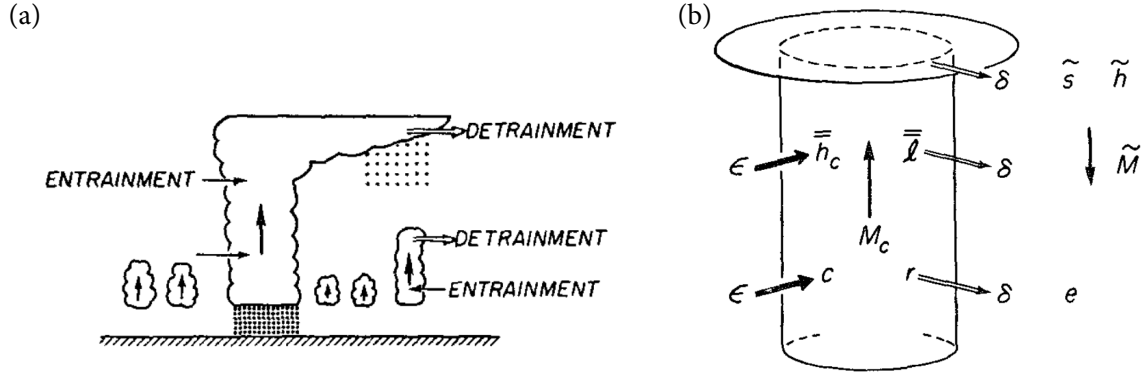


Figure 3.4.: Schematic view of (a) an ensemble of cumulus clouds and of (b) the bulk model of such an ensemble (from Yanai et al., 1973). The bulk quantities are the rates of entrainment ϵ and detrainment δ , the in-cloud and environmental vertical mass fluxes M_c and \tilde{M} , respectively, the specific cloud liquid water content \bar{l} , the rates of environmental evaporation e , in-cloud condensation c , and rain r , the in-cloud moist static energy \bar{h}_c , and the environmental dry and moist static energies \tilde{s} and \tilde{h} , respectively. All of these quantities are defined for every bulk cloud layer and they are linked by a set of hydrodynamic and thermodynamic equations. The conditions at the bulk cloud bottom and top as well as in its environment are determined from the large-scale atmospheric state, under the assumption that the cloud ensemble as a whole is in equilibrium with the large-scale dynamics.

simplified scheme were realistic.

Now, the parameterization problem in numerical atmospheric modeling is reverse in the sense that the large-scale tendencies due to SGS cumulus convection are its sought quantities (Arakawa and Schubert, 1974). Nevertheless, the bulk representation of an ensemble of cumulus clouds turned out to be a fruitful idea. It was adopted by the designers of cumulus parameterization schemes such as Tiedtke (1989). An adapted version of his scheme is implemented in CCLM and described in the following.

3.3.1. The Tiedtke Scheme

Let us first recall the purpose of cumulus parameterization schemes from the equation point of view. As already alluded to at the beginning of this chapter, their purpose is to specify those tendencies in GS budget equations of moisture and energy, best expressed in terms the water vapor specific humidity q_v and the specific dry static energy $s = c_p T + gz$, that are due to SGS cumulus convection. The left-hand side of (3.3) can be written as

$$\langle \rho \rangle \left[\frac{\partial \langle q_v \rangle}{\partial t} + \langle \mathbf{v} \rangle \cdot \nabla \langle q_v \rangle \right] + \langle q_v \rangle \left[\frac{\partial \langle \rho \rangle}{\partial t} + \nabla \cdot (\langle \rho \rangle \langle \mathbf{v} \rangle) \right], \quad (3.27)$$

where the second term vanishes due to mass continuity [cf. Eq. (2.2)]. As Tiedtke (1989) states, the horizontal eddy flux divergences of s and q_v can be neglected if the net lateral transports across the boundary of a grid volume by cumulus convection are small in comparison to the transport by the GS flow. This usually is the case at horizontal resolutions of some tens of kilometers or coarser

(Schättler et al., 2013) and (3.3) becomes

$$\frac{\partial \langle q_v \rangle}{\partial t} + \langle \mathbf{v} \rangle \cdot \nabla \langle q_v \rangle = -\frac{1}{\langle \rho \rangle} \frac{\partial (\langle \rho \rangle \langle q'_v w' \rangle)}{\partial z} + \langle e \rangle - \langle c \rangle, \quad (3.28)$$

where w is the vertical velocity component. While dry static energy is conserved during unsaturated motion, it is changed by phase transitions of water and by radiation. Similarly, the budget equation for q_v , one obtains

$$\frac{\partial \langle s \rangle}{\partial t} + \langle \mathbf{v} \rangle \cdot \nabla \langle s \rangle = -\frac{1}{\langle \rho \rangle} \frac{\partial (\langle \rho \rangle \langle s' w' \rangle)}{\partial z} - L(\langle e \rangle - \langle c \rangle) + \langle Q_{\text{rad}} \rangle, \quad (3.29)$$

where Q_{rad} is the rate of heating/cooling due to radiation. Then it is common to decompose the vertical SGS eddy covariances into contributions from turbulence and cumulus convection, amongst others, i.e. $\langle s' w' \rangle = \langle s' w' \rangle^{\text{tur}} + \langle s' w' \rangle^{\text{cum}} + \langle s' w' \rangle^{\text{...}}$ and similarly for q_v , so that the different SGS processes contribute linearly to the overall GS tendencies (Mironov, 2009).

The Tiedtke (1989) scheme is based on an extension of the Yanai et al. (1973) bulk cloud model by cumulus downdrafts, which in reality occur in association with convective precipitation. Accordingly, the eddy covariances due to cumulus convection have contributions from updrafts (\uparrow) and downdrafts (\downarrow),

$$\langle \rho \rangle \langle s' w' \rangle^{\text{cum}} = M^\uparrow (s^\uparrow - \langle s \rangle) + M^\downarrow (s^\downarrow - \langle s \rangle) \quad (3.30)$$

and similarly for q_v . Because of the approximation $\tilde{s} = \langle s \rangle$ and $\tilde{q}_v = \langle q_v \rangle$ [cf. Fig. 3.4(b)], (3.30) does not include contributions from environmental subsidence.

Cumulus convection also adds tendencies in condensation and evaporation to the right-hand sides of (3.28) and (3.29). In the Tiedtke (1989) scheme, these are $\langle c \rangle^{\text{cum}} = c^\uparrow$ for condensation occurring in updrafts and $\langle e \rangle^{\text{cum}} = e^\downarrow + e^\delta + e^p$ for evaporation in downdrafts that keep these saturated, evaporation of detrained cloud water and evaporation of precipitation in the unsaturated subcloud layer, respectively.

Due to the higher number of unknowns in his scheme, Tiedtke (1989) needs to impose more closure assumptions than Yanai et al. (1973). The conversion from cloud water into precipitation is assumed to happen at a constant relative rate for all cloud layers higher than 1500 m above cloud base, which ensures nonprecipitating shallow cumuli. Entrainment and detrainment into and from the bulk cloud can be turbulent and organized. We are going to elaborate on the organized part below. The rates of turbulent entrainment and detrainment of updrafts are set proportional to the updraft mass flux M^\uparrow and similarly for the downdrafts. The latter are assumed to begin at the GS level of free sinking following Fritsch and Chappell (1980), where M^\downarrow is set proportional to M^\uparrow at cloud base.

The *principle closure* of the scheme, defined by Arakawa (2004) as the hypothesis that links the existence and overall intensity of cumulus activity to large-scale processes, diagnoses the type of cumulus convection and specifies M^\uparrow at cloud base. Tiedtke (1989) distinguishes shallow, deep and mid-level convection, imposing different closures for the different convection types. Only one type of convection can be present in a grid column at a time. While shallow and deep convection are thought to have their roots in the planetary boundary layer, mid-level convection is thought to result from an elevated instability in frontal systems.

The discrimination of deep from shallow convection is based on the ratio of the total, i.e. vertically integrated, GS moisture convergence to the vertical moisture flux at the surface. Moist convection

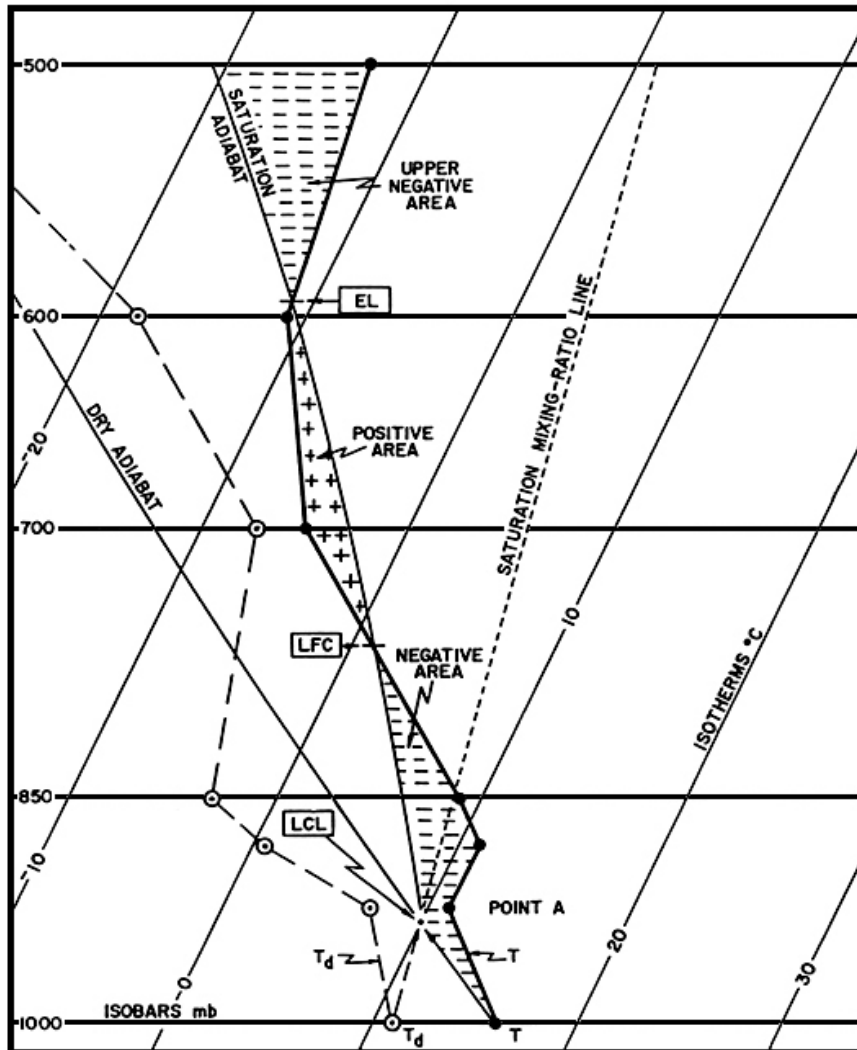


Figure 3.5.: Schematic skew-T diagram illustrating the definitions of the Lifting Condensation Level (LCL), the Level of Free Convection (LFC), and the Equilibrium Level (EL) (from Szoke, 2002). The thick solid line is the actual atmospheric temperature profile; the thin solid line is the temperature of a surface air parcel that is lifted through this atmosphere in a gedankenexperiment, first dry-adiabatically until saturation at the LCL, then moist-adiabatically. The level where the parcel would first become positively buoyant with respect to its environment is the LFC; the level where it would then first become neutrally buoyant again is the EL. The Convective Available Potential Energy (CAPE) is defined as the vertical integral of the positive buoyancy between the LFC and the EL.

is deemed deep/shallow when this ratio is above/below a fixed threshold. This way of distinction is suggested by the observation that deep cumulus convection is frequently associated with large-scale convergence in the lower troposphere while shallow tradewind cumuli can even form under a subsidence inversion.

Whether free convection (shallow or deep) can occur in a grid column is determined by a *trigger*. The trigger of the Tiedtke (1989) scheme consists of a test air parcel that is dry-adiabatically lifted from the lowest model layer through the GS atmosphere to the level of saturation (cf. LCL in Fig. 3.5). Departure humidity and temperature of the parcel are set to $\langle q_v \rangle$ and $\langle T \rangle + 0.5$ K, with $\langle q_v \rangle$ and $\langle T \rangle$ from the lowest model layer. The temperature perturbation is to account for SGS variability. Free convection is diagnosed if the parcel is positively buoyant at the level of saturation. In this case, this level defines the cloud base height z_{bas} and the values of s and q_v of the parcel at this level are used as lower boundary conditions for the bulk cloud model. The cloud top height z_{top} is determined by the level where the parcel becomes neutrally buoyant again (cf. EL in Fig. 3.5).

Otherwise, the grid column is checked for the possibility of mid-level convection, which in contrast to free convection does not have its roots in the planetary boundary layer. To that end, adiabatic test parcels with environmental properties are lifted by one layer from the second lowest and subsequently higher model levels. If the parcel becomes buoyant and if the respective layer has positive vertical velocity $\langle w \rangle$ and relative humidity $\langle U \rangle > 90\%$, then this layer is considered the cloud base of mid-level convection. Cloud top height and bulk model boundary conditions for s and q_v are then derived the same way as in the case of free convection.

The type of convection determines the cloud base mass flux. In the case of free convection, M^\uparrow and M^\downarrow at cloud base are determined under the assumption that the integrated moisture content of the subcloud layer remains constant, i.e.

$$\begin{aligned} & \left[M^\uparrow (q_v^\uparrow - \langle q_v \rangle) + M^\downarrow (q_v^\downarrow - \langle q_v \rangle) \right]_{\text{bas}} \\ &= - \int_{z_{\text{surface}}}^{z_{\text{bas}}} \left[\langle \rho \rangle \langle \mathbf{v} \rangle \cdot \nabla \langle q_v \rangle + \frac{\partial}{\partial z} (\langle \rho \rangle \langle q_v' w' \rangle^{\text{tur}}) \right] dz, \end{aligned} \quad (3.31)$$

which follows from (3.28) and (3.30). In the case of mid-level convection, the updraft mass flux at the cloud base is set equal to the vertical mass transport by the GS flow, i.e. $M_{\text{bas}}^\uparrow = \langle \rho \rangle_{\text{bas}} \langle w \rangle_{\text{bas}}$, which makes all the vertically advected moisture available to moist convection.

In addition, the type of convection determines the constants of proportionality in the updraft rates of turbulent entrainment and detrainment. In rough accordance with observations, the constants are set three times greater for shallow than for deep and mid-level convection. And also the rate of organized entrainment into the updraft depends on the type of convection as only for deep and mid-level convection, this type of entrainment is assumed to occur; its intensity is set proportional to the GS moisture convergence below the level of maximum vertical velocity, as suggested by Lindzen (1988). Irrespective of the type of convection, organized detrainment of the complete updraft mass flux is distributed to the zero-buoyancy level and the level above.

Besides GS tendencies in s and q_v , the CCLM implementation of the Tiedtke (1989) scheme also provides tendencies in horizontal momentum and chemical tracers that are due to the passive vertical transport of these quantities by cumulus convection. Let ψ be a horizontal wind component or the concentration of a chemical tracer, then

$$\langle \rho \rangle \frac{\partial \langle \psi \rangle^{\text{cum}}}{\partial t} = M^\uparrow (\psi^\uparrow - \langle \psi \rangle) + M^\downarrow (\psi^\downarrow - \langle \psi \rangle) \quad (3.32)$$

3. Parameterization of Clouds

parameterizes this transport, where the fluxes $M^\uparrow\psi^\uparrow$ and $M^\downarrow\psi^\downarrow$ change with height as a result of the passive lateral inflow and outflow of ψ into and out of updraft and downdraft by entrainment and detrainment. At cloud base, ψ^\uparrow and ψ^\downarrow are determined the same way as s , q_v , and q_c . Further revisions that led from the original Tiedtke (1989) scheme to its current CCLM implementation include a smoother phase transition to mixed-phase clouds, organized detrainment of cloud ice, and a lowered relative humidity threshold for the reevaporation of rain below cloud base (Brockhaus et al., 2009). A comprehensive description of the CCLM implementation of the Tiedtke (1989) scheme can be found in Doms et al. (2011a).

3.3.2. The IFS Scheme

The second cumulus convection scheme implemented in CCLM is a copy of the scheme implemented in the ECMWF IFS Cy33r1 (Bechtold et al., 2008). This scheme was originally based on the Tiedtke (1989) scheme but underwent numerous revisions in the meantime.

The first of these revisions was described by Gregory et al. (2000) and comprises three changes. The first change applies to the diagnosis of deep versus shallow convection which was replaced by a cloud depth criterion, with deep/shallow convection being diagnosed for a convective cloud depth of more/less than 200 hPa. The second change pertains to the shallow convective closure where the subcloud moisture balance (3.31) was replaced by an analogous subcloud dry static energy balance.

The third change concerns the deep convective closure. Based on the finding by Ceselski (1974) that low-level convergence is neither necessary nor sufficient for deep moist convection to occur, Fritsch and Chappell (1980) advocated to link the intensity of deep convection to the Convective Available Potential Energy (CAPE) and Nordeng (1994) showed that this improves the simulated tropical transient convective activity. CAPE is defined as the vertical integral of the positive buoyancy that is available to an ascending surface air parcel between its LFC and EL (cf. Fig. 3.5). CAPE is measured in joules per kilogram of air. Based on the virtual temperature $T_v \cong T(1 + (R_v/R_d - 1)q_v)$ it can be expressed as

$$\text{CAPE} = \int_{z_{\text{LFC}}}^{z_{\text{EL}}} g \frac{T_v^{\text{parcel}} - \langle T_v \rangle}{\langle T_v \rangle} dz. \quad (3.33)$$

It is assumed that cumulus convection leads to an exponential depletion of CAPE. Accordingly, the revised closure for the updraft mass flux at cloud base is $M_{\text{bas}}^\uparrow \propto \text{CAPE}/\tau$ with an adjustment time scale τ that in a second revision was set proportional to the convective turnover time scale.

This second revision of the scheme is described by Bechtold et al. (2008). Scaling factors are introduced that reduce the turbulent and organized entrainment into updrafts with height in order to mimic the effects of a cloud ensemble. Organized entrainment into the updraft is now limited to deep convection and linked to the GS relative humidity instead of the GS moisture convergence, which benefits the representation of tropical variability.

Further innovations with respect to the Tiedtke (1989) scheme include the introduction of organized entrainment (Nordeng, 1994) and detrainment for the downdraft, trigger parcel ascents for the diagnosis of free convection from multiple levels with temperature and humidity perturbation, a more sophisticated conversion of cloud liquid water and ice to precipitation following Sundqvist (1978), and partially revised values for the various parameters of the scheme. A comprehensive description of the IFS Cy33r1 convection scheme is given by the ECMWF (2009).

4. Dynamical Downscaling and CCLM

Climate impact models often require meteorological input data at horizontal resolutions that cannot be supplied by GCMs due to computational constraints. This particularly pertains to the surface climate in regions of complex topography. Different *downscaling* methods have been devised to bridge this gap (Wilby and Wigley, 1997). The most common approach is to run a climate model over a limited area at the desired resolution using interpolated GCM output as lateral boundary conditions (Dickinson et al., 1989; Giorgi, 1990). This method is termed *dynamical downscaling* and the corresponding atmospheric models are called *limited area models* or *regional climate models* (RCMs).

The idea of one-way nesting a high-resolution limited area model into a GCM was originally born in the weather forecasting community and then adopted by climate modelers (Dickinson et al., 1989). The method is pragmatic and much simpler to apply than a two-way nesting where RCM and GCM are run in parallel to feed aggregated RCM results back to the GCM at run time (Phillips and Shukla, 1973). This ease comes at the cost of unrepresented interactions between RCM-scale and GCM-scale dynamics and it aggravates inconsistencies at the RCM domain boundaries (Zhang et al., 1986; Warner, 1989), which occur in a two-way nesting framework as well, not just due to different spatial resolutions but also because, in most applications, the employed regional and global models differ in both their dynamical core and their parameterization schemes.

To handle these inconsistencies in the one-way nesting framework, Davies (1976) suggested to introduce a sponge zone extending across the n outermost grid points of the RCM grid, where the RCM variables are gradually blended with the GCM variables to facilitate a smooth transition between the two grids. Technically, this can be realized by adding an extra term to the tendencies of every prognostic variable ψ as per

$$\left(\frac{\partial \langle \psi \rangle}{\partial t} \right)^{\text{lateral boundary}} = \mu_i \left(\langle \psi \rangle^{\text{lateral boundary}} - \langle \psi \rangle \right), \quad (4.1)$$

where $\langle \psi \rangle^{\text{lateral boundary}}$ represents the boundary data and μ_i decays exponentially with grid-cell distance $i = 1, \dots, n$ to the domain edge. This approach is also adopted in the RCM CCLM that we employ in this study.

Our simulations are performed with CCLM version 4.25.3, which has about 300 000 lines of code and around 300 namelist parameters. A typical model run using 256 processors of the PIK high-performance cluster roughly takes one day per simulation year. This means that any brute force scanning of the parameter space to the end of finding an optimum model setup is doomed to failure. The only feasible way to improvement is via insights into the simulated physical system and into the conceptualization of this system in the model.

Since CCLM was designed for climate simulations on highly resolved horizontal grids down to mesh sizes on the order of 1 km, it is based on the nonhydrostatic Navier-Stokes equations (cf. Ch. 2). These are discretized on a rotated spherical coordinate system to have as regular a grid as possible within the simulation domain; in a typical application, the pole is tilted such that the equator runs through the center of the domain [cf. Fig. 4.1(a)]. Also for numerical reasons, CCLM uses terrain-

4. Dynamical Downscaling and CCLM

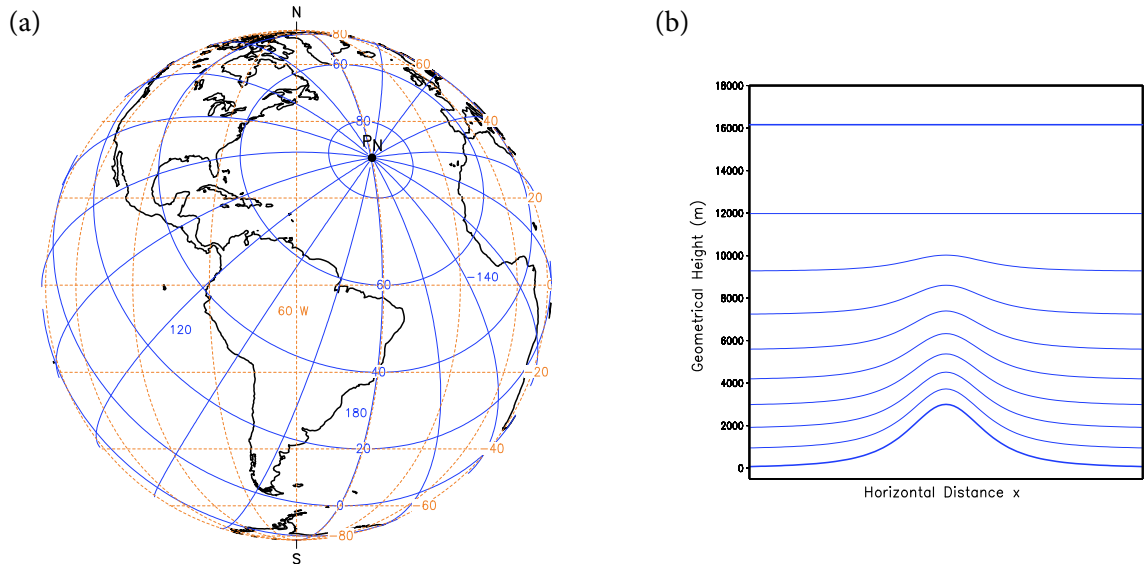


Figure 4.1.: (a) Rotated spherical coordinate system (solid blue) with its North Pole tilted to 30°N , 40°W with respect to the geographical coordinate system (broken orange) and (b) schematic diagram of a terrain-following vertical coordinate over a bell-shaped mountain (from Doms et al., 2011b).

following vertical coordinates, which means that the bottom model level represents the atmospheric layer directly atop the earth's surface, the top model level represents a flat atmospheric layer at some prescribed height, and the intermediate levels represent atmospheric layers of gradually increasing flatness with height [cf. Fig. 4.1(b)].

The dynamical core of CCLM is based on a finite difference numerical scheme. The discretized model variables are staggered on an Arakawa-C/Lorenz grid (Cushman-Roisin and Beckers, 2011; Lorenz, 1960), which means that scalars such as $\langle \rho \rangle$, $\langle q_x \rangle$, $\langle p \rangle$, and $\langle T \rangle$ are defined at grid volume centers while the three velocity components $\langle u \rangle$, $\langle v \rangle$, and $\langle w \rangle$ are defined at grid volume faces, i.e. halfway between the centers. Several time integration schemes are implemented. In our application we use a total variation diminishing version of a 3rd order Runge-Kutta split-explicit scheme (Liu et al., 1994; Doms et al., 2011b).

The cloud parameterizations of CCLM distinguish between GS and SGS clouds. A bulk water-continuity model describes the GS clouds (Doms et al., 2011a). It includes prognostic equations for water vapor, rain, snow, cloud liquid water, and cloud ice. SGS clouds are considered as either cumuliform or stratiform and are parameterized as described in Ch. 3. Radiative transfer is parameterized with the Ritter and Geleyn (1992) scheme that is based on a delta-two-stream approximation of the radiative transfer equations with three spectral intervals in the solar and six in the thermal part of the radiation spectrum. In addition to the standard atmospheric gases the radiative properties of aerosols and of liquid water and ice clouds are taken into account. SGS turbulence is parameterized with a prognostic turbulent kinetic energy closure at level 2.5 according to Mellor and Yamada (1982) that includes effects from SGS condensation and evaporation (Raschendorfer, 2001). Per default, soil processes are parameterized by the multi-layer soil model TERRA-ML (Schrodin and Heise, 2001), plants are modeled following the biosphere-atmosphere transfer scheme by Dickinson et al. (1986), and the bare surface is parameterized according to Dickinson (1984).

5. What We Talk about When We Talk about Climate Model Evaluation

The overarching topic of this thesis is the evaluation of numerical atmospheric models. When we write *model evaluation* we mean a model quality assessment based on the comparison of simulated with observed values of some observables of the simulated system. While this task is frequently referred to as *model validation* in the scientific literature, we prefer the former over the latter term for reasons well compiled by Oreskes (1998) and summarized in the following.

To begin with, a *model validation* does not make any sense if taken literally. We adhere to the argument by Popper (1937, 1963) that scientific models or theories can only be proven wrong, never right. If valid is understood in the strict sense of objectively true this implies that any attempt of a *model validation* must fail, which reduces the term ad absurdum.

Nevertheless, many scientists have used and are using the term, thinking of a valid model as one without obvious flaws or defects. As Oreskes (1998) argues, using the term with this less strict definition in mind is fine for communication within the scientific community, yet it turns problematic when model validation studies are read by nonexperts. This is because, commonly, the language of such studies is excessively affirmative, which in combination with the term *model validation* communicates an overly positive level of confidence in model quality.

In conclusion, Oreskes (1998) advocates the use of the more logically sound and less suggestive term *model evaluation*. It also is the more general of the two terms (Hodges and Dewar, 1992). Next to simulation-observation comparisons one may evaluate a model's conceptualization of reality, the number and measurability of its input parameters, or its numerical formulation. Yet within this thesis we are solely going to use the term in the narrow sense stated at the outset of this section.

Modelers and observers of the climate system have cross-fertilized each other for decades. Comparisons of simulations with observations of atmospheric dynamics have been done since the very first attempts of their numerical modeling (Donner et al., 2011). Early model evaluations focused on the atmospheric energy cycle, the zonal-mean circulation, and regional surface climatologies. Subsequent ones examined the three-dimensional structure of the general circulation and atmospheric variability at various time scales, paying particular attention to mid-latitude synoptic disturbances and to the El Niño Southern Oscillation. With the rising concern over anthropogenic climate change and a concurrent increase of model utilization for future climate projections, recent evaluations have investigated the ability of climate models to replicate historical climate variations.

Many methods and metrics have been devised to quantify the degree of agreement between simulation and observation. Very simple ones are employed in the first part of this thesis. In the second part we then introduce and apply more sophisticated metrics based on climate networks.

6. The Sensitivity Study: Preliminaries

In the next chapter we present the results of the first comprehensive CCLM evaluation over South America. In particular, we examine the importance of the representation of SGS clouds for a faithful simulation of precipitation over the tropical part of the continent. While it is well documented that cumulus parameterization is crucial in this regard (Betts and Jakob, 2002; Bechtold et al., 2004; Santos e Silva et al., 2012), less is known about the sensitivity of simulated precipitation characteristics to the parameterization of nonprecipitating SGS clouds.

6.1. Study Design

We comparatively evaluate four CCLM hindcast simulations with model setups that differ in the chosen parameterizations of moist convection and of SGS clouds in the radiative transfer scheme but that are identical in other respects. These parameterizations are the ones described in Ch. 3; the labels we use to refer to the corresponding 2×2 model setups are displayed in Tab. 6.1.

We run the model on the CORDEX South America domain, which implies a horizontal resolution of 0.44° , i.e. of about 50 km. The computational grid includes an additional ten grid point wide sponge zone for boundary data relaxation (cf. Ch. 4) and consists of a total of 166×187 points (Fig. 6.2). The vertical coordinate is set to have 40 levels reaching up to 30 km above sea level, and as suggested by Panitz et al. (2013) for tropical domains, we adjust the Rayleigh damping height to 18 km.

In order to account for the deep roots in tropical rainforests, we lower the bottom of the deepest hydrologically active soil layer of TERRA-ML to 8 m (Nepstad et al., 1994; Baker et al., 2008). In accordance with Galbraith et al. (2010), we also increase the optimum temperature for stomatal conductance from 20°C to 25°C . Values for external model parameters such as land surface elevation, surface roughness length, and leaf area index are adapted from the ECOCLIMAP data set (Smiatek et al., 2008).

Our evaluation period covers 14 years from 1998 to 2011. Model runs are started in 1990 to allow for a spin-up of 8 years. Interpolated ERA-Interim reanalysis data (Dee et al., 2011) are used as initial and lateral boundary conditions.

setup label	cumulus convection scheme	nonprecipitating SGS cloud scheme
TR	Tiedtke (Sec. 3.3.1)	relative humidity (Sec. 3.1.1)
TS	Tiedtke	statistical (Sec. 3.1.2)
IR	IFS (Sec. 3.3.2)	relative humidity
IS	IFS	statistical

Table 6.1.: Labels and parameterization schemes of CCLM setups.

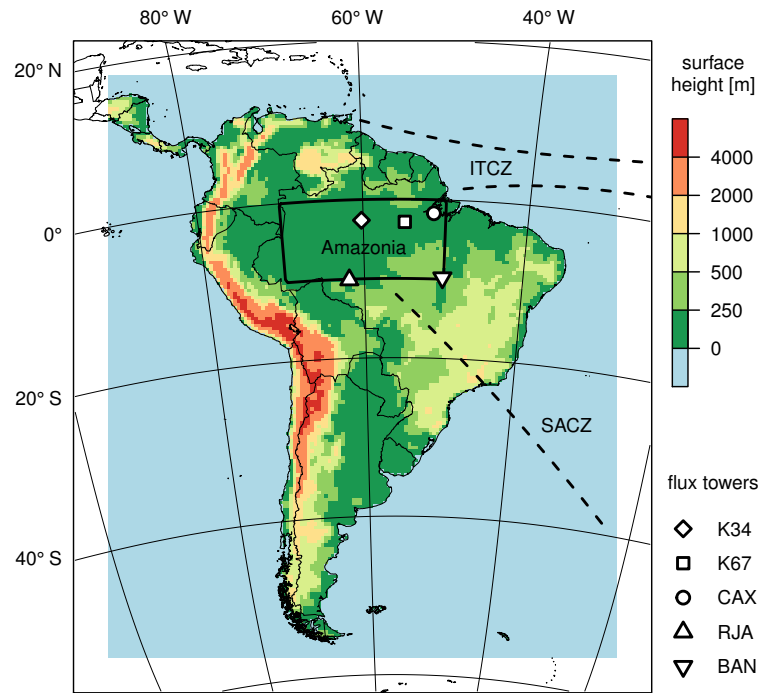


Figure 6.2.: Computational domain for CCLM simulations. The model evaluation is restricted to the CORDEX South America domain (colored). Marked are further the region we refer to as Amazonia in Sec. 7.2 (solid box), the locations of the five flux towers (Tab. 6.3), data recorded at which we employ below, and the climatological locations of the SACZ (southernmost dashed line) and of the Atlantic ITCZ in austral summer (middle dashed line) and winter (northernmost dashed line). Colors indicate surface elevation as it is represented in the model.

6.2. The South American Climate

The South American continent extends across several climate zones from 10°N to 55°S. Along its western shore, the Andes form a narrow but high orographic barrier (Bookhagen and Strecker, 2008). In line with climatological conditions, vegetation types vary considerably. While tropical South America is dominated by the vast Amazonian rainforest, various kinds of wood- and shrublands, savannas, and deciduous forests are found in the subtropics, and grasslands and semideserts prevail in southern South America. Climatically, throughout the year, the continent is framed by the Inter Tropical Convergence Zone (ITCZ) in the north, westerly winds in the south, and subtropical high pressure systems over the Pacific and Atlantic oceans in the west and east, respectively (Garreaud et al., 2009).

In austral winter, the ITCZ rain band retreats to northwestern South America, leaving the southern Amazon basin, the adjacent savanna, and northeastern Brazil in their dry season (Vera et al., 2006a; Liebmann et al., 2007). The westerlies carry extratropical cyclones to the south of the continent, supplying precipitation to the southwestern coast and to southeastern South America (Mendes et al., 2010).

In austral summer, the greatest part of the continent is subject to the South American Monsoon System (SAMS; Zhou and Lau, 1998; Vera et al., 2006b; Marengo et al., 2012b). Next to the ITCZ,

this comprises the South Atlantic Convergence Zone (SACZ), a band of moisture convergence and abundant precipitation extending southeastward from central Amazonia (Nogués-Paegle et al., 2002; Carvalho et al., 2004). Further low-level features of the SAMS include a thermal depression called the Chaco low over northwestern Argentina and the South American Low-Level Jet (SALLJ; Marengo et al., 2004), which transports large amounts of moisture from Amazonia to the subtropical plains through a narrow channel between the Andes and the Brazilian Plateau. The most prominent feature of the high-level circulation in austral summer is a large anticyclonic circulation called the Bolivian high, which can be considered together with the low-level Chaco low as a response to the strong convective heating in the Amazon region. The SAMS is characterized by enhanced convective activity and heavy precipitation in tropical South America. Moist convection has a pronounced diurnal cycle, is frequently organized in squall lines or other mesoscale convective systems, and is modulated by extratropical frontal systems (Molion, 1993; Silva Dias et al., 2002; Rickenbach et al., 2002; Salio et al., 2007).

6.3. Observational Data

We employ site measurements and various gridded data sets for the model evaluation. Prior to any comparison, the gridded data are interpolated from their native grid to the rotated spherical coordinate system of CCLM. In the case of radiative fluxes, cloud cover, and precipitation we apply a first-order conservative remapping scheme (Jones, 1999). Temperature, geopotential, and winds are interpolated bilinearly. Winds are additionally rotated in order to account for the relative rotation of grids.

We evaluate precipitation against the Tropical Rainfall Measuring Mission (TRMM) 3B42 V7 daily satellite product, which starts in 1998 and comes at a native resolution of 0.25° (Huffman et al., 2007). It arguably is the best precipitation data set available for tropical South America given its high resolution and the comparatively large uncertainties of gauge measurement data in the area (Carvalho et al., 2012). The product is based on measurements by radar, infrared and microwave sensors aboard numerous satellites, and calibrated by station data. While it is available up to 50° latitude, the TRMM precipitation radar data only extend to 36° latitude so that we constrain our analysis to latitudes north of 40°S , where the data are most reliable. We do not consider this a problem since our study focuses on the tropical climate of South America, and since inter-setup differences of modeled precipitation characteristics are small at more southern latitudes.

Total cloud cover is compared to the International Satellite Cloud Climatology Project (ISCCP) D2 monthly means from 1998 to 2007 which have a native resolution of 2.5° (Rossow and Schiffer, 1999). The cloud cover estimates are based on satellite observations of infrared and visible radiation and have an uncertainty of about 5%.

Surface shortwave and longwave net radiation are evaluated against the NASA/GEWEX Surface Radiation Budget (SRB) release-3.0 monthly estimates from 1998 to 2007 at a native resolution of 1° (Stackhouse Jr. et al., 2011), which are based on various input data including temperature and moisture profiles from the NASA Global Modeling and Assimilation Office GEOS-4 reanalysis product, and cloud parameters from ISCCP DX data. The estimates have uncertainties of about 20 W/m^2 for shortwave and 5 W/m^2 for longwave radiation.

2 m temperatures are compared to the Climatic Research Unit (CRU) TS3.21 monthly observations from 1998 to 2011 at the native resolution of 0.5° (Harris et al., 2013). This data set covers land points only, but since CCLM adopts the ERA-Interim sea surface temperatures we expect only minor differences of oceanic 2 m temperatures between different model runs.

6. The Sensitivity Study: Preliminaries

	K34	K67	CAX	RJA	BAN
longitude [°W]	60.21	54.96	51.46	61.93	50.16
latitude [°S]	2.61	2.86	1.72	10.08	9.82
height [m]	50.0	63.0	51.5	60.0	40.0
coverage [y]	7	4	3	3	3

Table 6.3.: Locations, measurement heights, and temporal data coverages of the Large-scale Biosphere-atmosphere Experiment in Amazonia (LBA) flux towers at Manaus Km34 (K34), Santarém Km67 (K67), Caxiuanã (CAX), Reserva Jaru (RJA), and Bananal Island (BAN).

850 hPa geopotential and wind are evaluated against ERA-Interim reanalysis data. As a benchmark reference, we also include ERA-Interim data in the evaluation of the other variables. Besides, this allows us to identify biases introduced by the lateral boundary conditions.

In order to compare simulation results to site measurements at high temporal resolution we include data recorded at the towers of the LBA-ECO CD-32 Brazil Flux Network (Saleska et al., 2009). This data set comprises hourly measurements from nine sites during the years 1999 to 2006. However, for most sites, this time frame is not entirely covered, and at some sites the vegetation is unnatural, which is a problem since the land cover data used by CCLM in the corresponding grid cells represent natural vegetation. Choosing sites with natural vegetation only that, in addition, provide at least 3 years of precipitation, temperature, and net radiation data, we end up with the towers at Manaus Km34 (K34), Santarém Km67 (K67), Caxiuanã (CAX), Reserva Jaru (RJA), and Bananal Island (BAN). Their locations, measurement heights, and temporal data coverages are displayed in Tab. 6.3 (cf. Fig. 6.2). All measurements were taken just above the canopy so that they may well be compared to the modeled surface fluxes and atmospheric variables at 2 m height. We compare tower measurements to data from the closest model grid cell, considering only times, when tower data are available.

7. The Sensitivity Study: Results

In the following, we first evaluate seasonal mean values of precipitation, total cloud cover, 2 m temperature, surface net shortwave and longwave radiation, as well as 850 hPa geopotential and wind over the whole evaluation domain. Then, we focus our analyses on Amazonia, where we start with an evaluation of the seasonal cycles and summertime diurnal cycles of precipitation, 2 m temperature, and surface net radiation at the flux tower sites (cf. Fig. 6.2), followed by an evaluation of the distribution of summertime daily precipitation intensities, and concluded with a comparison of summertime mean cloud profiles simulated with the different CCLM setups.

7.1. Seasonal Mean Values

To keep the climatological mean value evaluation compact, we limit it to the austral summer (December-January-February, DJF) and winter (June-July-August, JJA) seasons. This should suffice to obtain a general impression of the performance of CCLM over the region, since DJF and JJA comprise the months of the southernmost and northernmost locations of the ITCZ, which means that the two seasons characterize the South American climate extremes.

7.1.1. Precipitation

We commence with the central variable of this study. DJF and JJA mean precipitation are shown in Fig. 7.1. In DJF, the TRMM and ERA-Interim data exhibit the typical monsoon season rainfall pattern with precipitation maxima along the ITCZ, the SACZ, and the eastern Andes (cf. Bookhagen and Strecker 2008).

The CCLM simulations show quite different qualities in reproducing this pattern. With the TR setup, the model generates contrasting biases of more than 50% overestimation over the oceanic part of the ITCZ and more than 50% underestimation over land except along the Andes south of 20°S. As alluded to in the introduction, the rediscovery of this bias pattern was the starting point for this sensitivity study. Rockel and Geyer (2008) had shown this land-sea contrast of precipitation biases to occur over tropical domains around the globe when the CCLM is run with the TR SGS cloud schemes, and Panitz et al. (2013) partially confirmed this finding in recent CCLM simulations over Africa.

Substituting the IFS for the Tiedtke scheme smoothes rainfall patterns and reduces biases over land as well as over oceans. Especially the oceanic wet bias is almost completely removed and over the Andes the model produces less excessive precipitation. Gregory et al. (2000) found a similar smoothing of spatial rainfall patterns as well as rain rate reductions along the maritime ITCZ in global seasonal forecasts with the ECMWF IFS after changing trigger and closure of deep convection from those based on moisture convergence as proposed by Tiedtke (1989) to ones based on cloud depth and CAPE, respectively. Further modifications of the trigger and of entrainment rates led to qualitatively similar precipitation changes though (Bechtold et al., 2004). Since these are just some of the differences between the two cumulus convection schemes (cf. Sec. 3.3.2), it is difficult to tell which of the differences are most responsible for the improvements seen in Fig. 7.1.

7. The Sensitivity Study: Results

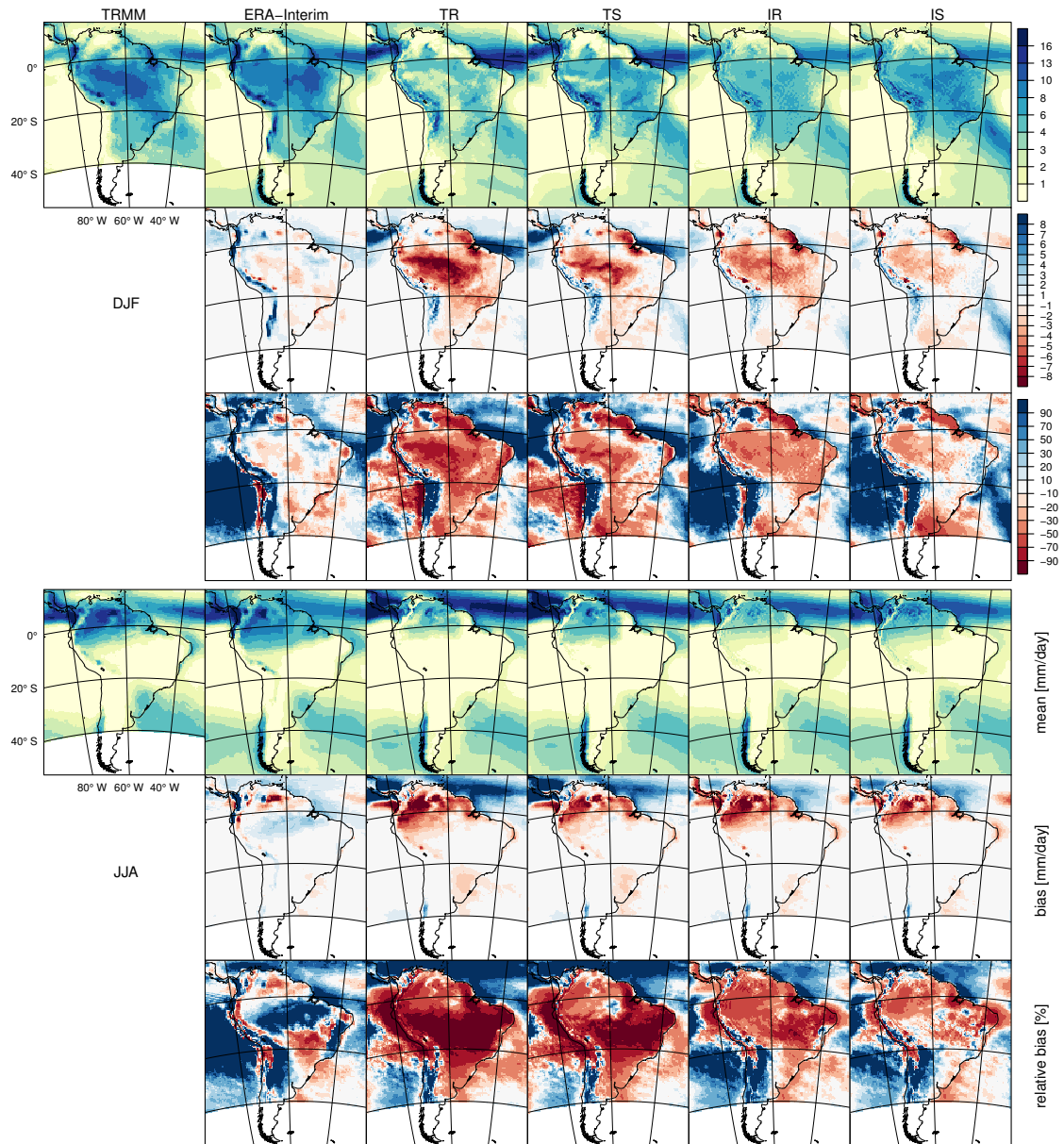


Figure 7.1.: Mean precipitation versus TRMM observations during austral summer (DJF, upper three rows) and austral winter (JJA, lower three rows) from 1998 to 2011. For each season, the top row shows the seasonal mean, the middle row shows the absolute (sim-obs), and the bottom row the relative $((\text{sim}-\text{obs})/\text{obs})$ difference to the observation, which is displayed in the leftmost column, followed by ERA-Interim, and the CCLM simulations with the TR, TS, IR, and IS setup (from left to right).

In comparison to simulations with the RH scheme, those with the statistical scheme show a further reduction of the dry bias over land. With the IS setup, the dry bias in western Amazonia is reduced to 30%—a magnitude also found with other RCMs (Marengo et al., 2009; Solman et al., 2013); in eastern Brazil we see a mix of over- and underestimations. While a strong sensitivity of simulated precipitation to the cumulus parameterization could be expected, the large sensitivity to the representation of SGS clouds in the radiation scheme is remarkable. We are going to elaborate on this latter sensitivity below.

Some biases, however, are common to all model setups and are also shared by other climate models. For instance, the overestimation of precipitation along the Andes (except at its eastern slopes between 0° and 20°S) is a feature of ERA-Interim, the reanalyses CFSR and MERRA (Carvalho et al., 2012), and many RCMs (Marengo et al., 2009; Solman et al., 2013).

Another example is the dry bias of up to 50% in northern Argentina, which is shared by all simulations while it is not seen in the ERA-Interim data, but observed in CFSR and MERRA (Carvalho et al., 2012). Observations have shown that monsoon-season rainfall is highly stochastic in this region and characterized by a heavy-tail distribution (Boers et al., 2013), which implies that heavy rain events (> 20 mm/day) contribute considerably to the total precipitation. Some of these events are caused by the world's largest mesoscale convective systems (Vera et al., 2006b), which suggests that such systems are not well reproduced by CCLM—in fact we show in Sec. 7.2.3 that CCLM strongly underestimates the frequency of heavy rain events over Amazonia. The particular importance of these events for the mean DJF precipitation over northern Argentina probably explains the respective dry bias.

Along the coast around the outlet of the Amazon river, the baseline land-sea bias contrast remains with all CCLM setups. It also is a feature of other climate models (Marengo et al., 2009; Solman et al., 2013; Joetzjer et al., 2013) and of ERA-Interim. In CCLM, it might therefore result from inaccurate boundary conditions. In fact, ERA-Interim wind uncertainties in the Atlantic ITCZ are considerable as direct observations are essentially limited to satellite scatterometer measurements (Žagar et al., 2011) and since there is comparably little wind information in tropical mass field observations (Žagar et al., 2005). Findings by Bechtold et al. (2014, Fig. 11) suggest that a better representation of the diurnal cycle of convection (cf. Sec. 7.2.2) could reduce the coastal bias contrast. Alternatively, one could attribute it to an interplay of an incorrect representation of the local land-sea circulation and a mischaracterization of the soil moisture-precipitation feedback: An erroneous land-sea breeze circulation with too little rainfall over land dries out the soil. In reality this would lead to stronger convection over land (Taylor et al., 2012), which would counterbalance the model deficit, but with the two cumulus convection schemes employed here, dryer soils inhibit convection (see Hohenegger et al. (2009) for CCLM with the Tiedtke scheme and Taylor et al. (2012) for ERA-Interim with the IFS scheme). Presumably, the deficient simulation of this feedback also aggravates the aforementioned dry bias over northern Argentina.

In JJA, we see the same land-sea bias contrast as in DJF, which is again most pronounced for the TR setup and least for IS. Again, a switch of the convection scheme from Tiedtke to IFS reduces biases over land and oceans while a swap from the RH to the statistical scheme mainly yields increased precipitation over land. With the TR setup, the rainfall maximum over southeastern South America is underestimated by up to 50%, as by the RCMs evaluated by Solman et al. (2013). Moving from TR to IS, this bias gradually declines. For the IS setup, the modeled mean rainfall pattern resembles the TRMM observation. Remaining deficiencies include dry biases in northeastern Brazil and northern Amazonia, as well as wet biases in the Gulf of Mexico, in northern Argentina, and in Chile, all of which are also shared by ERA-Interim.

7. The Sensitivity Study: Results

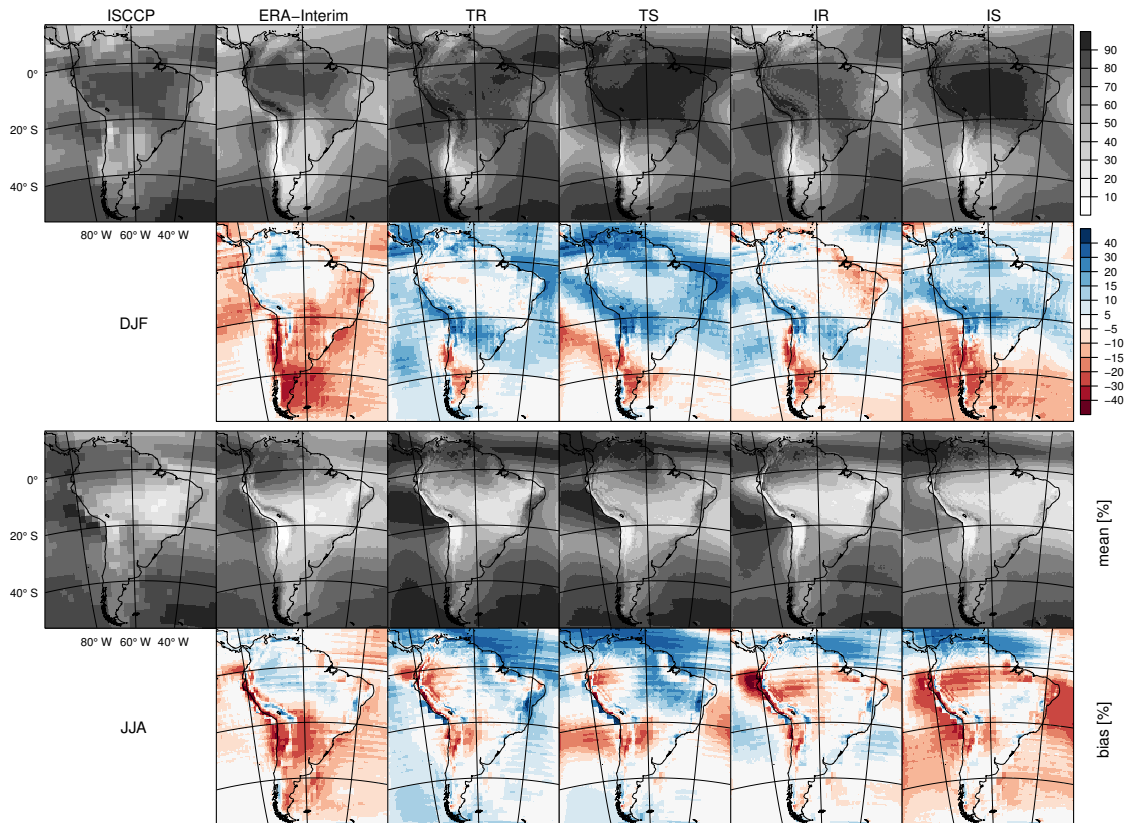


Figure 7.2.: Mean total cloud cover versus ISCCP observations from 1998 to 2007. Layout as described in Fig. 7.1, without relative biases.

7.1.2. Total Cloud Cover

Since we observed a major sensitivity of modeled mean precipitation to the parameterization of SGS clouds, we also expect major differences in the simulated cloud cover between model setups. The DJF and JJA mean values of total cloud cover are shown in Fig. 7.2 and they indeed vary considerably between simulations. Compared to the ISCCP data, the TR setup generally yields a too high mean cloud cover over the oceans in summer and winter. As could be expected, a change of the convection scheme results in smaller cloud cover changes than a change of the representation of SGS clouds in the radiation scheme. With the IFS scheme, it is generally less cloudy than with the Tiedtke scheme. The IR setup yields the smallest overall biases in both seasons.

Substituting the statistical for the RH scheme yields increased (reduced) cloud cover in regions with frequent (rare) incidences of deep convection. This pattern of change is most clearly visible in DJF when we find a sharp boundary between these regimes approximately along a great circle through 10°S , 90°W and 30°S , 30°W . It suggests that with the statistical scheme, CCLM generates less stratiform clouds, such that the total cloudiness is reduced in regions where stratiform clouds prevail, such as over the cool sea surface temperatures of the eastern Pacific (Mechoso et al., 2005). In regions with frequent deep convective activity we suppose that a more vigorous convective activity acts to counterbalance the by itself less frequent occurrence of stratiform clouds and leads to a greater overall cloudiness. This interpretation is consistent with the concurrently enhanced mean precipitation rates over Amazonia (cf. Fig. 7.1) and we are going to substantiate it below.

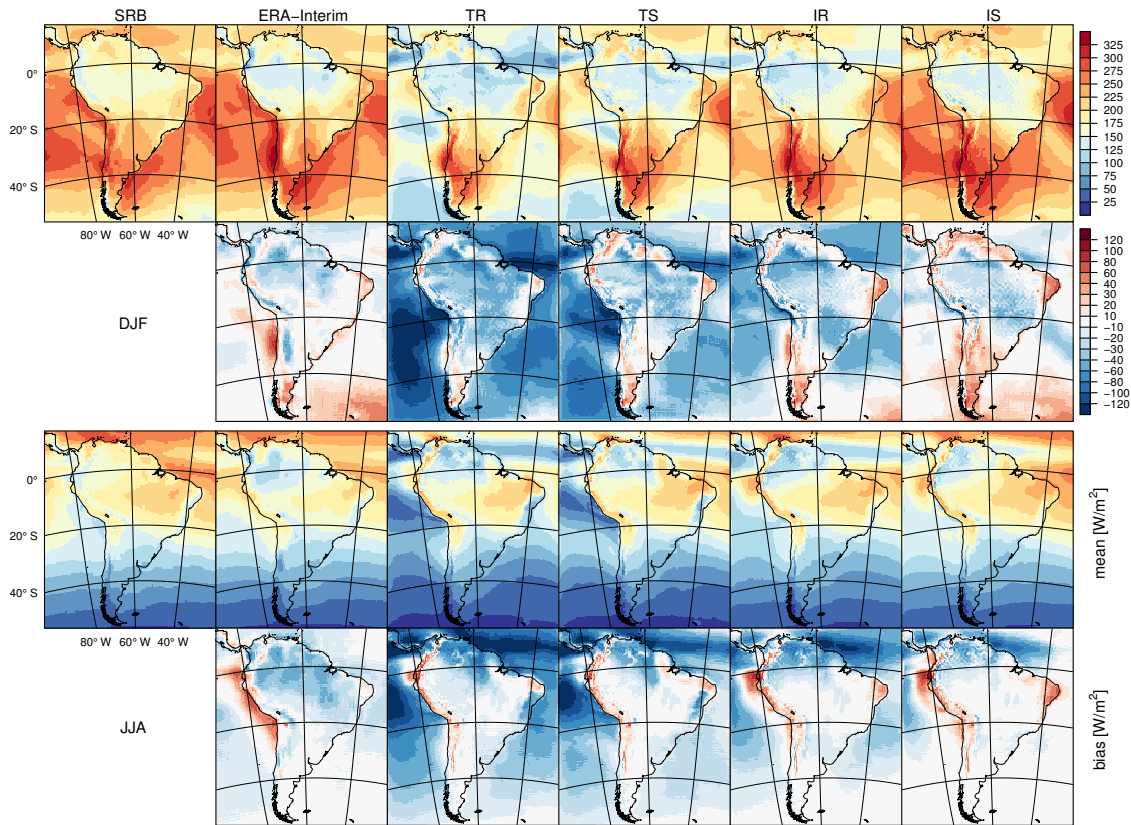


Figure 7.3.: Mean shortwave net radiation at the surface versus SRB observations from 1998 to 2007. Layout as described in Fig. 7.2.

7.1.3. Surface Shortwave Net Radiation

Since there is a direct relation between cloud cover and radiation budgets, we investigate the latter in the following. The DJF and JJA mean values of net surface shortwave radiation are displayed in Fig. 7.3. Compared to the SRB estimates, the TR setup severely underestimates shortwave net radiation, especially over the oceans. Similar to precipitation, biases of the same kind and magnitude were found over Africa (Panitz et al., 2013).

Employing the IFS instead of the Tiedtke scheme considerably mitigates the biases, as does substituting the statistical for the RH scheme. The differences between model setups are by far more pronounced over sea than over land. With the IS setup, the modeled shortwave net values resemble the SRB estimates in summer and winter. The remaining biases are underestimations (overestimations) inside (outside) the convergence zones ITCZ and SACZ.

The reduced surface shortwave net biases suggest a more correct representation of daytime clouds. As put forward by Morcrette et al. (2008), more solar radiation reaching the surface yields enhanced convection over tropical land masses. Thus the continuous increase of surface shortwave net radiation from TR to IS are in line with the respective increases of precipitation over the South American continent.

Related to the consistency between different variables, we observe an odd situation north of 20°S (the equator) in austral summer (winter). In this area, a comparison of simulations with different parameterizations of SGS clouds shows a positive correlation of total cloud cover and net surface

7. The Sensitivity Study: Results

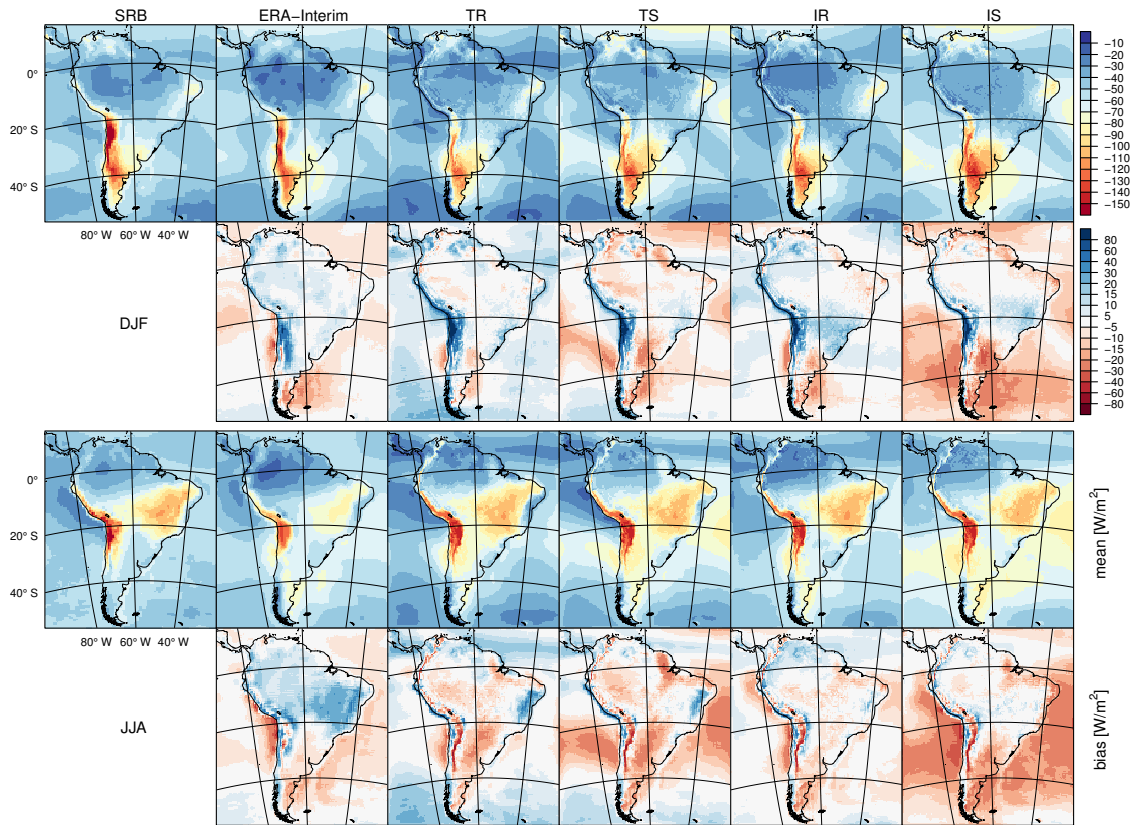


Figure 7.4.: Mean longwave net radiation at the surface versus SRB observations from 1998 to 2007. Layout as described in Fig. 7.2.

shortwave radiation. We discuss this apparent contradiction and provide a solution in Sec. 7.2.4.

7.1.4. Surface Longwave Net Radiation

In order to complete the radiation budget evaluation we now discuss DJF and JJA mean values of the modeled net surface longwave radiation (Fig. 7.4). Since the daytime radiation budget is shortwave dominated, longwave results primarily represent nighttime conditions. In comparison to the SRB data, the smallest biases are obtained with the IR setup.

Over land, using the IFS instead of the Tiedtke scheme mostly reduces biases while using the statistical instead of the RH scheme generally increases the outgoing longwave radiation, i.e. renders the net surface longwave radiation more negative, which leads to mixed bias changes.

Over sea, we observe increased outgoing longwave radiation for both, a swap of the cumulus parameterization to the IFS scheme, and a swap of representation of SGS clouds in the radiation parameterization to the statistical scheme—with a greater sensitivity to the latter change. With the IS setup, the outgoing longwave radiation is generally overestimated.

Considering the inter-setup differences of net surface shortwave and longwave radiation together, we conclude that with the statistical scheme, CCLM produces optically thinner clouds than with the RH scheme. For Amazonia in DJF, the validity of this conclusion is evidenced in Sec. 7.2.4.

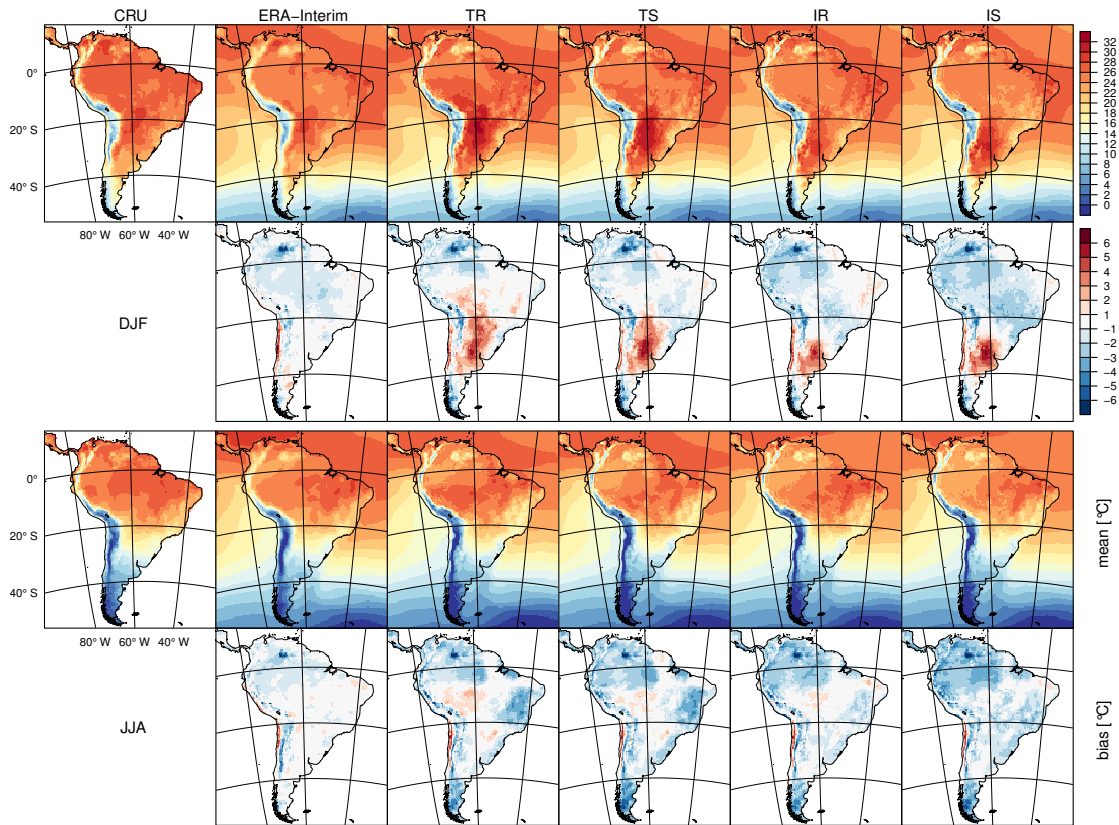


Figure 7.5.: Mean 2 m temperature versus CRU observations from 1998 to 2011. Layout as described in Fig. 7.2. Biases are height corrected with a constant lapse rate of 6.5 K/km.

7.1.5. 2 m Temperature

As an example of a variable which depends on the surface fluxes of radiation and precipitation, we evaluate the 2 m temperature, the DJF and JJA mean values of which are shown in Fig. 7.5. The bias patterns with respect to CRU observations are height corrected with a constant lapse rate of 6.5 K/km and do not differ much between model setups. Biases are greater in austral summer than in winter.

All year round we find a cold bias in Amazonia, which we reconsider in Sec. 7.2.1 because of the discrepancies between CRU temperatures and those measured on the flux towers. Cold biases along the Andes and over the Guiana Highlands are mostly shared by ERA-Interim, as is a warm bias in the Atacama desert.

While CCLM mostly produces too low temperatures, we find a pronounced DJF warm bias in northern Argentina, which is common to many RCMs (Solman et al., 2013). In part, we attribute it to the severe dry bias in this region and season that we discussed in Sec. 7.1.1, since the respective precipitation and temperature biases significantly anticorrelate (99% confidence level) across CCLM setups, and because the soil receives a lot of insolation in this area during summer (cf. Fig. 7.3), which makes it susceptible to dry stress.

However, a linear regression reveals that the dry bias does not fully explain the warm bias. The work by Wagner et al. (2012) suggests that its fundamental source is located outside the region of occurrence: The authors evaluated CCLM simulations over extratropical South America and

7. The Sensitivity Study: Results

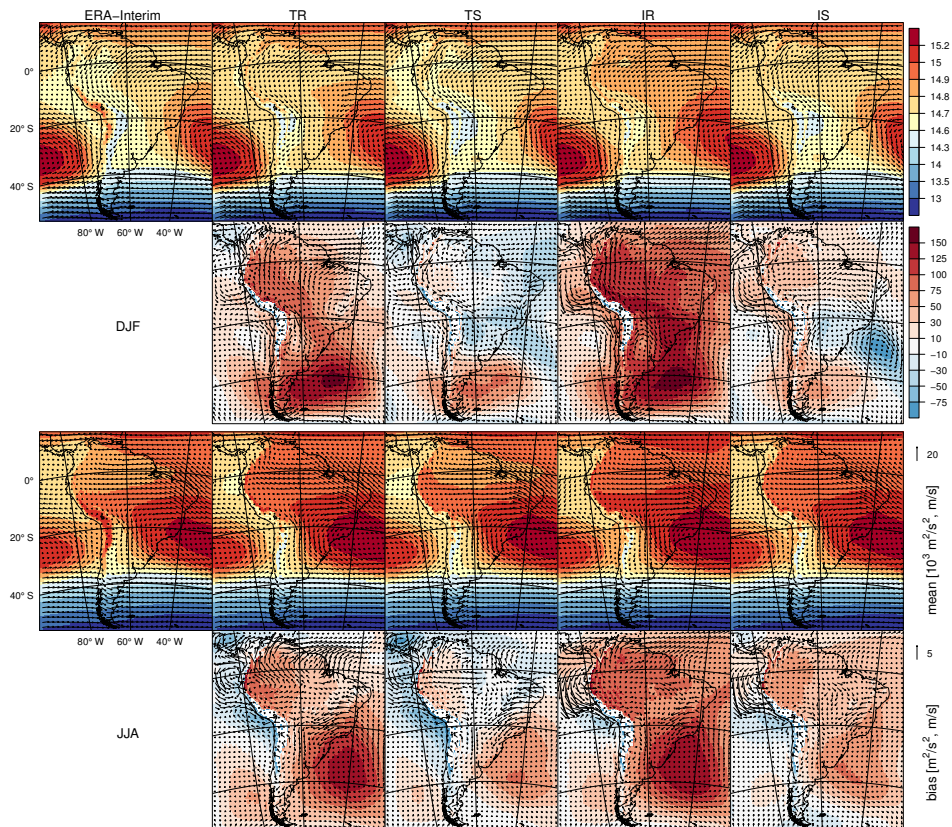


Figure 7.6.: Mean fields of 850 hPa geopotential (colors) and wind (vectors) versus ERA-Interim reanalyses from 1998 to 2011. Layout as described in Fig. 7.2.

found a substantial sensitivity of northern Argentinean DJF 2 m temperatures to the forcing data. Downscaling a GCM simulation, CCLM generated a warm bias of similar magnitude to the one found here. Yet, when forced by ERA40 reanalysis data, the model produced a slight cold bias. Since the predominant DJF low-level inflow to the region is from north, the warm bias might reflect modeling errors over the tropical part of the continent, possibly including a poor representation of the SALLJ. To check this hypothesis, we evaluate the 850 hPa circulation next.

7.1.6. Low-Level Circulation

The DJF and JJA mean fields of 850 hPa geopotential and wind are displayed in Fig. 7.6. The ERA-Interim data show the westerlies in the south, the subtropical anticyclones over the Atlantic and Pacific oceans, the monsoon circulation in summer, and strong trade winds over the tropical Atlantic and northeastern Brazil in winter.

In DJF, CCLM generally exaggerates the relative strength of the Chaco low over northern Argentina, which leads to a regional bias cyclonic circulation that deflects the inflow of moist Amazonian air to the east. This probably contributes to the summer dry bias in northern Argentina.

Over western Amazonia, pressure is too high throughout the year and with all setups, which indicates too weak diabatic heating and is consistent with the underestimation of (convective) precipitation in this area (cf. Fig. 7.1).

Generally, there is a strong dependence of pressure and circulation biases on the representation

of SGS clouds in the radiation parameterization. With the RH scheme, the geopotential is mostly overestimated and we find an all-year bias anticyclone over the subtropical Atlantic as well as a bias antimonsoon circulation in DJF. In simulations with the statistical scheme, the overall low-level pressure and circulation biases are strongly reduced. In DJF, we find a bias cyclonic circulation over the subtropical Atlantic. It explains the northeast displacement and intensification (increased moisture convergence) of the respective SACZ rainband (cf. Fig. 7.1).

Throughout the year and more pronounced with the IFS convection scheme, there is a bias pressure dipole over the Pacific between 0° and 30°S (10°N and 20°S) in summer (winter), which causes bias westerly/northwesterly winds off the Peruvian coast. The reason for this bias remains unclear as does the source of the warm bias during northern Argentinean austral summer. A full understanding of the latter would require further analyses of surface fluxes and atmospheric profiles, which are beyond the scope of this study.

7.2. Amazonia

In the following we focus on simulation results over Amazonia. Solman et al. (2013) have found most discrepancies between climate simulations with different RCMs over this part of South America, which suggests a generally high modeling uncertainty in the region. Fortunately, all flux towers meeting the criteria mentioned in Sec. 6.3 are located in this area, so that we can compare modeled seasonal and diurnal cycles to site measurements. Further below in this section we present DJF statistics of different model variables over Amazonia, which is defined as a latitude-longitude box from 0°S to 10°S and from 50°W to 70°W (cf. Fig. 6.2).

7.2.1. Seasonal Cycles

We start with the seasonal cycles of precipitation, net surface radiation, and 2 m temperature at the five flux tower sites (cf. Tab. 6.3 and Fig. 7.7). In order to assess measurement uncertainties we include cycles from the gridded data sets TRMM, SRB, and CRU as they were used for the evaluation of seasonal mean values above.

While the TRMM and SRB estimates mostly agree with the tower measurements, we find substantial differences between observed temperatures. The tower top temperatures are systematically lower than those estimated by the CRU. The greater measurement height of 40 to 60 m of the towers alone cannot explain the differences of typically 1 to 2 K. We presume that they are mainly due to the different meteorological conditions above a closed rainforest canopy, as represented by the tower measurements, and at a regular rainforest weather station, as represented by the CRU data. The fact that the differences are smaller in dry than in wet season supports this presumption. Since modeled 2 m temperatures represent values above vegetation, the tower top data are the more suitable reference. This implies that the Amazonian cold bias diagnosed in Sec. 7.1.5 is at least less severe or even negligible, especially during the wet season.

In the following we discuss the results for each site individually, as measured cycles as well as model biases vary considerably between them.

Among the five towers, the K34 tower is the most centrally located in the Amazon basin. Together with the CAX site it has the least pronounced dry season with monthly mean precipitation rates remaining above 3 mm/day throughout the year; most rain falls in March-April-May. Both characteristics are reproduced by all CCLM simulations. The peak rain rates are strongly underestimated by all simulations though, especially with TR and IR. The net surface radiation is underestimated

7. The Sensitivity Study: Results

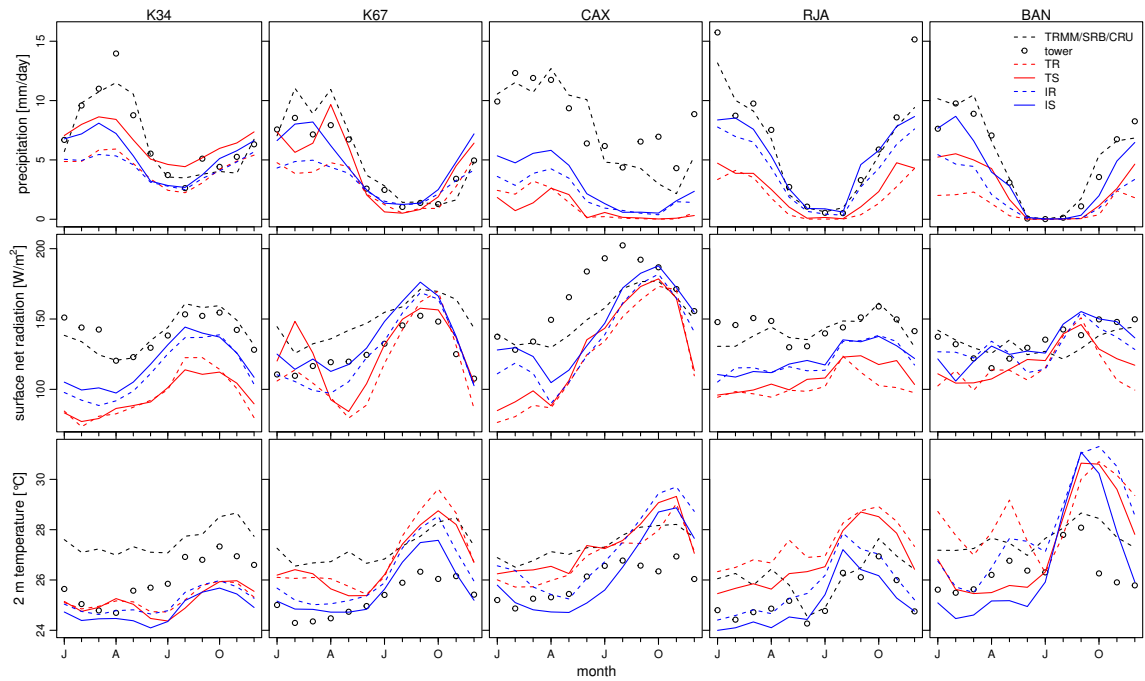


Figure 7.7.: Mean seasonal cycles of precipitation (top row), net surface radiation (middle row), and 2 m temperature (bottom row) modeled with the CCLM with four different setups (Tab. 6.1) versus measurements at the five LBA flux tower sites (columns, Tab. 6.3). Also included are cycles from the gridded data sets TRMM, SRB, and CRU for precipitation, radiation, and temperature, respectively.

with all model setups in all months and by up to 50 W/m^2 in January-February-March. The seasonal cycles of 2 m temperatures do never differ by more than 1 K between setups, have too small amplitudes, and show an average underestimation of 1 K.

At the K67 site, the seasonal cycles of all three variables are well captured with the IS setup, whereas with the other setups, the model is either too dry, too warm, or overestimates the net radiation's interseasonal variability.

The CAX tower is located close to the Amazon river delta and we recognize the severe dry bias discussed in Sec. 7.1.1. For all model setups we find a strong underestimation of net radiation from April to August. Note that according to the SRB data the latter problem is less significant. The discrepancy between ground measurement and satellite product might be due to the complex shape of the coastline, which is nearby and cannot be properly represented at a horizontal resolution of 1° . Temperatures differ by up to 2 K between model setups with drier simulations being warmer. In September-October-November-December the model is too warm with all setups.

The rainforest around the RJA site is subject to a high amplitude seasonal cycle of precipitation with mean rates below 2 mm/day in JJA and at up to 15 mm/day in DJF. The rain peaks are underestimated with all model setups but apart from that the seasonal cycle is well captured by the IS simulation. Surface net radiation is underestimated with all model setups in all months. The temperature cycle is simulated well with the IS setup while with the others, temperatures are overestimated by up to 2 K.

The BAN site, situated in a transition region between rainforest and savanna, features the most

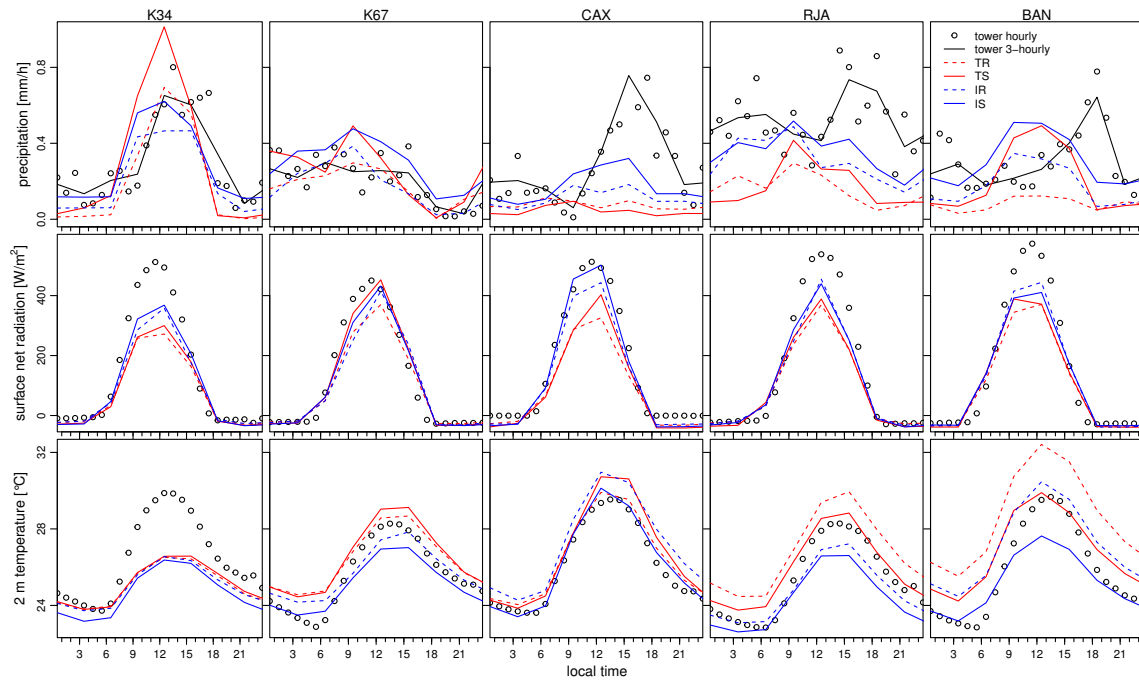


Figure 7.8.: Mean DJF diurnal cycles of precipitation, net surface radiation, and 2 m temperature, simulated with CCLM versus measured at the LBA flux towers. Layout as described in Fig. 7.7.

pronounced dry season. With every setup, the model underestimates rainfall during the onset of the wet season, which results in temperature overestimations by 3 to 4 K. Inter-setup differences are large for precipitation and, consequently, temperature.

In summary, we find a systematic underestimation of surface net radiation at the western sites K34 and RJA. As previously pointed out in Sec. 7.1.1, the model is not able to generate monthly mean rain rates of more than 10 mm/day over Amazonia. Temperatures show a strong response to precipitation at all sites subject to (simulated) dry stress. We do not see this response at the K34 site because there no simulation is dry enough to let soil moisture control evaporation rates (Koster et al., 2004) and in turn temperatures. The IS setup yields the best overall performance.

7.2.2. Diurnal Cycles

In the following we focus on the austral summer season since this is the wettest season at all flux tower sites except K34. The DJF diurnal cycles of precipitation, net surface radiation, and 2 m temperature at the LBA flux towers are depicted in Fig. 7.8.

We observe that the underestimations of net surface radiation diagnosed before occur mainly at daytime. We find the strongest of those underestimations at the K34 site and see that it results in temperatures being 4 K too low at noon. At all sites except CAX, the amplitude of the diurnal temperature cycle is too small for simulations with the IFS convection scheme.

However, the most striking deviations between modeled and measured diurnal cycles are found for precipitation. While CCLM simulates peak rain rates at noon or earlier at all sites, the measurements show them between 15 and 18 h local time—except at the K67 tower, where precipitation does not have a pronounced diurnal cycle. Especially at the CAX site there is a large difference between

morning and afternoon rain rates that is not adequately captured by CCLM.

The problem of a proper representation of the diurnal cycle of convective precipitation over land is shared by various RCMs and GCMs (e.g. Dai et al., 1999; Betts and Jakob, 2002; Grabowski et al., 2006; da Rocha et al., 2009; Nikulin et al., 2012). The reason for the too early precipitation peak was found to be a too easy triggering of moist convection by many convection schemes (Dai et al., 1999; Bechtold et al., 2004). Dai et al. (1999) conclude that “this keeps the model atmosphere from building up high CAPE and prevents intense precipitation from occurring.” Bechtold et al. (2014) show that slowing down the convective adjustment over tropical land can indeed lead to a higher buildup of CAPE prior to the onset of deep convection, which then occurs later and features greater peak rain rates. As these changes are shown to also result in enhanced mean precipitation, we think that CCLM’s inability to simulate monthly mean precipitation rates of more than 10 mm/day over Amazonia can be attributed to its poor representation of the diurnal cycle of convection.

Considering the diurnal and seasonal cycles of precipitation, net surface radiation, and 2 m temperature in synopsis, the model is most accurate at the K67 tower. According to Vera et al. (2006b, Fig. 5), occurrences of deep convective systems are rare around this site. This exemplifies that the model does fine where it does not need to simulate such systems.

7.2.3. Precipitation Intensities

So far, we have only evaluated climatological mean rain rates. When it comes to climate impacts, especially those of extreme events, there is yet another important characteristic of rainfall—the statistics of daily precipitation intensity. In the following, we evaluate two of these statistics over Amazonia in DJF from 1998 to 2011 (Fig. 7.9).

CCLM and ERA-Interim show considerable biases in the frequency distribution of daily rain amounts. Both simulate too many wet days (> 0.1 mm/day) and too infrequent heavy rain events (> 20 mm/day), i.e. they rain a bit every day instead of remaining dry on some days and raining fiercely on others. These problems are shared by many climate models (Dai, 2006). Especially with the IFS convection scheme, the underestimation of the number of days with less than 0.1 mm/day by CCLM is dramatic.

ERA-Interim strongly overestimates the frequency of days with 5 to 16 mm precipitation. Depending on its setup, CCLM produces too many days with precipitation between 1 to 9 (TR) and 3 to 17 mm/day (IS). A swap of the representation of SGS clouds in the radiation parameterization from the RH to the statistical scheme moves the frequency distribution to higher intensities.

As a result of those differences, the contributions of light (< 10 mm/day), moderate (10 to 20 mm/day), and heavy (> 20 mm/day) rain events to precipitation totals vary across models and setups. According to the TRMM data, heavy rainfall should contribute 55%, light and moderate rainfall only 20% and 25%, respectively. In contrast, ERA-Interim and CCLM with the IS setup attribute the largest contribution to light precipitation with about 45% and consequently underestimate the contribution of heavy rain events.

With the other setups, CCLM overestimates the contribution of light rainfall as well, but simulates that of heavy rainfall more adequately. With the TR setup, heavy rainfall even contributes more than 60% due to the very low total precipitation in combination with the simulation of some extreme events of more than 100 mm/day. Such extremes are only generated with the Tiedtke convection scheme. A swap of the representation of SGS clouds in the radiation parameterization from the RH to the statistical scheme yields a favorable doubling of the contribution of moderate rain events to the total precipitation.

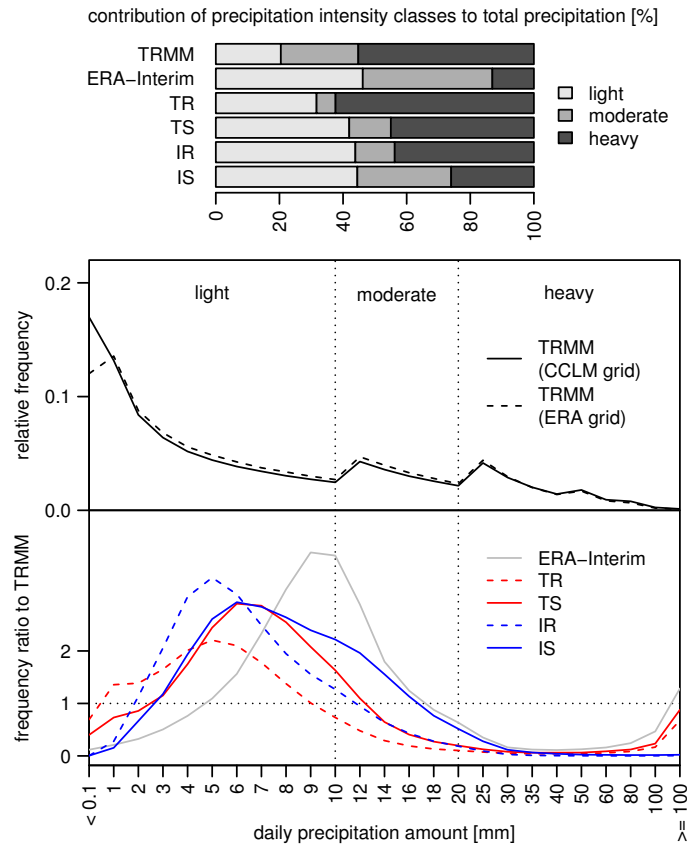


Figure 7.9.: Simulated and observed statistics of daily precipitation intensities over Amazonia in DJF from 1998 to 2011. (top) Relative contributions of daily precipitation amounts from different intensity classes to the total amount, with discrimination between light (< 10 mm/day), moderate (10 to 20 mm/day), and heavy (> 20 mm/day) precipitation events. (middle) Frequency distribution of daily rain amounts according to TRMM, interpolated to the CCLM and ERA-Interim grids. (bottom) Model-to-TRMM ratios of these frequencies for ERA-Interim and the four CCLM runs, with TRMM data interpolated to the respective grids.

7.2.4. Cloud Profiles

In Sec. 7.1 we have shown that simulations with the statistical parameterization of nonprecipitating SGS clouds typically feature higher (lower) net surface shortwave (longwave) radiation than with the RH scheme. At daytime, this sums up to a greater total net radiation (cf. Fig. 7.8) which enables more vigorous convection and higher rain rates (cf. Figs. 7.1 and 7.8). We now want to illuminate how it is possible that the enhanced shortwave and reduced longwave net values coincide with an increased total cloud cover over Amazonia in DJF. To that end, the respective space-time averages of simulated vertical profiles of cloud cover fraction C and cumulus cloud cover fraction C^{cum} as well as of specific cloud ice and liquid water contents q_i^{rad} and q_l^{rad} are depicted in Fig. 7.10.

We observe that with the statistical scheme, on average, clouds contain 40% less water and 75% less ice than with the RH scheme. An analysis of the distribution of simulated stratiform cloud cover C^{str} reveals that this reduction is due to a practically complete disappearance of nonprecipitating

7. The Sensitivity Study: Results

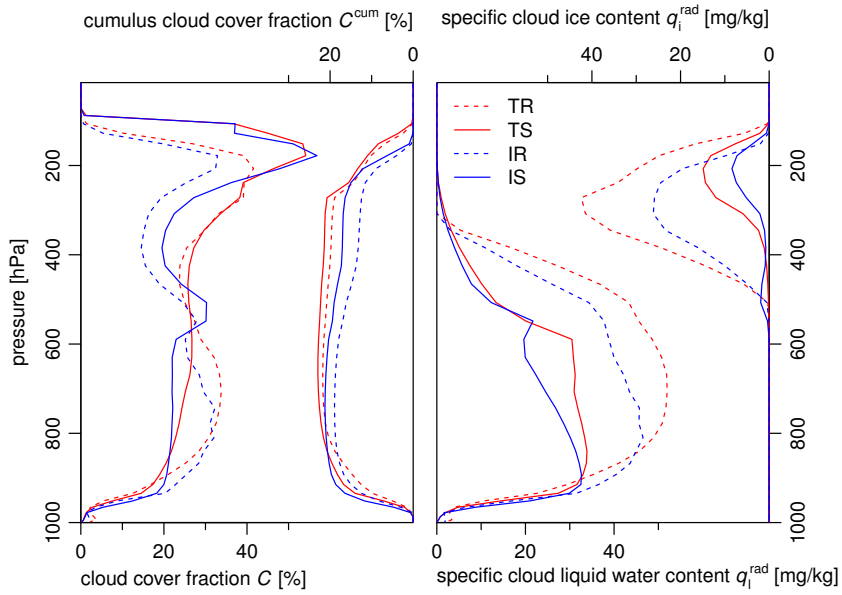


Figure 7.10.: Mean DJF vertical profiles of cloud cover fraction C and cumulus cloud cover fraction C^{cum} [left, Eqs. (3.19) and (3.21)] as well as of specific cloud ice content q_i^{rad} and specific cloud liquid water content q_l^{rad} [right, Eqs. (3.22) and (3.24)] over Amazonia, as simulated with the four CCLM setups from 1998 to 2011.

SGS clouds with the statistical scheme, i.e. with this scheme, all simulated clouds over Amazonia in DJF are either convective or GS. In contrast, warm and cold nonprecipitating SGS clouds do occur with the RH scheme, which leads to the respective increases in q_l^{rad} and q_i^{rad} .

A reduced cloud water content results in an atmosphere that is more translucent, the net surface shortwave radiation increases and more energy is available for buoyancy and convection. Consequently, we observe enhanced mean convective cloud cover C^{cum} at all levels (cf. Fig. 7.10) and greater mean rain rates (cf. Fig. 7.1) with the statistical scheme.

Consistent with these changes we also find a marked increase of the mean high cloud cover (Fig. 7.10), probably due to more frequent occurrences of cirrus forming from the anvils of thunderstorm clouds. (Not shown: The Amazonian DJF mean high cloud cover has a diurnal cycle that lags the convection cycle by about four hours and is strongly amplified with the statistical scheme.) This increase is the primary reason for the 5% to 15% increase in DJF mean total cloud cover over Amazonia found in simulations with the statistical scheme (Fig. 7.2). Since high cirrus clouds are typically optically thin, their increased frequency of occurrence does not contradict a concurrently enhanced net surface shortwave radiation.

8. Summary and Discussion I

In the first part of this dissertation we provide the first comprehensive evaluation of CCLM over South America. Our analyses focus on precipitation, cloud cover, and surface radiation. We compare the performance of the model with four different setups, which differ in the parameterizations of SGS clouds.

The simulated climate is proven to be highly sensitive to the parameterization choices, particularly in tropical latitudes. While precipitation biases are large with the default parameterization schemes which are an adapted version of the Tiedtke (1989) scheme for cumulus convection and a RH scheme for nonprecipitating SGS clouds, they can be strongly reduced using the cumulus convection scheme from the ECMWF IFS Cy33r1 and a statistical scheme for nonprecipitating SGS clouds. With the latter setup, biases are within the range of those produced with other state-of-the-art RCMs. CCLM is now ready for applications such as regional climate projections or the investigation of climate sensitivities to land-use change in South America, and can take part in RCM ensemble studies over the region via frameworks such as CORDEX. Furthermore, our findings will help to improve the model's performance over other tropical domains.

Since a large fraction of tropical precipitation falls out of cumulus clouds, it was expected that simulated precipitation is sensitive to the parameterization of cumulus convection. We reveal that its sensitivity to the parameterization of SGS clouds in the radiation scheme can be of similar magnitude. We explain this latter sensitivity via the surface radiation budget. With the statistical in place of the RH SGS cloud scheme, ice and liquid water contents of clouds are strongly reduced, which allows more solar radiation to reach the surface. As previously described by other authors (Hohenegger et al., 2008; Xu and Small, 2002; Morcrette et al., 2008), this allows for more vigorous moist convection and, in turn, enhanced precipitation rates. To our knowledge, this is the first RCM sensitivity study to compare simulations with a statistical and a RH scheme for the parameterization of nonprecipitating SGS clouds in combination with different schemes for the parameterization of cumulus convection. Although we only present results for a specific RCM over a specific domain, our findings may benefit the development of other numerical atmospheric models over other domains as well.

For the variables considered in this study, the CCLM setup with the IFS convection and the statistical nonprecipitating SGS cloud scheme yields the best overall performance. Remaining model biases include an all-year dry bias over Amazonia with a pronounced land-sea bias contrast around the Amazon river outlet. The low-level pressure is generally overestimated over the tropical part of the continent. A substantial austral summer dry bias is present in northern Argentina and contributes to a pronounced warm bias found in the same region and season. Temperatures are generally too low in the tropics when compared to the CRU data. However, when considering the LBA flux tower measurements, this bias may be less distinct or even negligible in some cases.

The remaining dry biases occur in areas over which mesoscale convective systems propagate frequently in nature. Besides northern Argentina (Vera et al., 2006b; Boers et al., 2013), these areas include Amazonia, where mesoscale organization of moist convection usually occurs in the form of squall lines that develop at the northeastern coast of South America as a result of sea-breeze induced instabilities and then propagate westward across the Amazon basin (Garstang et al., 1994; Cohen

8. *Summary and Discussion I*

et al., 1995). Such propagating mesoscale convective systems cannot be captured in simulations with conventional cumulus convection schemes because these schemes do not admit the nonlocal and nonequilibrium diurnal physics that govern mesoscale convective organization (Pritchard et al., 2011). Hence it is reasonable to assume that a considerable fraction of the remaining precipitation dry biases over tropical and subtropical South America are associated with a deficient simulation of propagating mesoscale convective systems.

Moreover and probably connected to this deficiency, we find considerable remaining misrepresentations of the diurnal precipitation cycle and of the distribution of daily precipitation amounts over Amazonia. From a general point of view, our study underlines the important role clouds play in the climate system. The model sensitivities we find illustrate the complicated feedbacks between the radiative and hydrological properties of clouds and the impacts they exert on other parts of the system. Overall, our results confirm that the parameterization of clouds remains one of the most important and difficult problems in numerical atmospheric modeling.

II.

Complex Networks for Climate Model Evaluation with Application to Dynamical versus Statistical Regional Climate Modeling over South America

9. Introduction II

The analysis presented in the previous part was an example of a conventional climate model evaluation in the sense that it was *limited* to the simulation-observation comparison of statistics of time series representing *individual* locations. We examined the simulation quality of temporal mean values and frequency distributions. Other statistics considered in comparable *univariate model evaluation* studies include extreme value percentiles (Ban et al., 2014), temporal variabilities at various time scales (Randall et al., 2007; Lin et al., 2009), season onset dates and lengths (Liebmann et al., 2007), and serial correlations (Koster and Suarez, 2001). The results are often presented in the form of bias maps, which in turn may be spatially aggregated to root-mean-square deviations (Willmott, 1981; Decker et al., 2011) or Taylor diagrams (Taylor, 2001; Pincus et al., 2008).

In the second part of this thesis we develop and apply new performance metrics for climate model evaluation. Such an effort was explicitly requested by the Fourth Assessment Report of the IPCC (Randall et al., 2007; Lucarini and Ragone, 2011), given that the quantification of the accuracy of numerical climate simulations is necessary not only for model improvement as exemplified above, but also for the assessment of the uncertainty of future climate projections (Wigley and Raper, 2001; Stott and Kettleborough, 2002; Murphy et al., 2004), for the selection or weighting of climate simulations for climate impact studies (Pierce et al., 2009; Christensen et al., 2010), and where hypotheses about climate dynamics, feedbacks, or sensitivities are tested by means of numerical simulation to advance our general understanding of the climate system (Held, 2005; Lucarini, 2008).

In its Fifth Assessment Report the IPCC acknowledges that model performance metrics have been increasingly applied in the meantime (Flato et al., 2013). Yet a closer look at the referenced model intercomparison studies (Gleckler et al., 2008; Pincus et al., 2008; Waugh and Eyring, 2008; Reichler and Kim, 2008; Cadule et al., 2010) reveals that the metrics employed therein are still based on univariate statistics. This is suboptimal considering that such statistics are only partly representative of the complicated spatiotemporal dynamics of the climate system. In particular, they cannot capture the fundamental statistical relationships between dynamics at *different* locations.

Walker (1928) ascribed the first finding of connections between weather in different parts of the earth to Hoffmeyer who pointed out the association between pressure over the North Atlantic and weather in Europe in 1878. In the meantime, a multitude of such connections has been found in the form of recurrent spatial patterns of meteorological anomalies relative to the respective climatological mean fields. Prominent examples of such fluctuating anomaly patterns include the North Atlantic Oscillation (Hurrell, 1995), the Madden-Julian Oscillation (Madden and Julian, 1994), and the El Niño Southern Oscillation (Trenberth, 1997).

A promising recent approach to the quantification and analysis of these spatial relationship patterns is based on network theoretical concepts. In a *climate network*, nodes correspond to meteorological² anomaly time series at different locations and links between the nodes represent statistical relationships between the corresponding time series (Fig. 9.1). This identification sets the stage for

²We write *meteorological* here and in the following because in this dissertation we are only concerned with *atmospheric* dynamics. In general, of course, climate networks may represent spatiotemporal dynamics within and/or between any of the five components of the climate system, which are the atmosphere, the hydrosphere, the cryosphere, the lithosphere, and the biosphere (Baede, 2001).

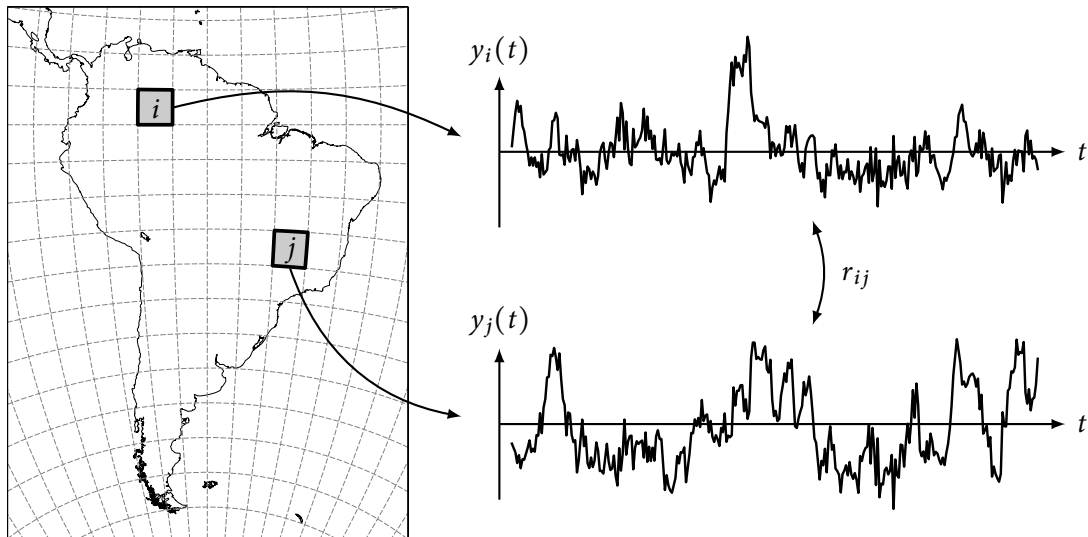


Figure 9.1.: Climate networks represent statistical relationships r_{ij} between anomaly time series $y_i(t)$, $y_j(t)$ that represent meteorological² variability around climatological mean values at locations i , j .

the application of various network analysis methods and promises new insights into the spatial interdependency structure of atmospheric dynamics (Tsonis and Roebber, 2004; Tsonis et al., 2006). The climate network approach has been applied to investigate monsoon system dynamics (Boers et al., 2013; Stolbova et al., 2014), to study impacts of El Niño events (Tsonis and Swanson, 2008; Gozolchiani et al., 2011), to detect dynamical transitions in the climate system (van der Mheen et al., 2013; Rehfeld et al., 2014), and to predict selected weather and climate events (Ludescher et al., 2013; Boers et al., 2014).

Only lately the community has begun to employ climate networks for *multivariate model evaluation* purposes (Fountalis et al., 2013; Steinhäuser and Tsonis, 2013; Fountalis et al., 2014). In these studies, network nodes are first grouped into geographically connected subsets with strong internal network connectivities, and these clusterings are then compared between networks constructed from observed and simulated data. A potential drawback of this approach is that relevant information may be lost by the clustering; in any case only a fraction of the information contained in the climate networks enters the comparison.³ Our objective is to advance the *network approach to climate model evaluation* by developing tools for network comparison that take the full network structure into account.

We will introduce such tools in the following chapter. Later on, we are going to demonstrate their capabilities as model performance metrics in two RCM evaluation studies over South America, where we compare the performance of CCLM to that of a statistical RCM. The latter will be introduced in the chapter after the next.

³Climate model evaluation with empirical orthogonal functions (Lau, 1981; Miller et al., 2006; Handorf and Dethloff, 2012) has the same conceptual limitation.

10. Network Theory

A *network* or *graph* is a set of items, called *vertices* or *nodes*, with connections between them, called *edges* or *links*. The study of complex system dynamics with network theoretical concepts has thrived for some time (Newman, 2003; Boccaletti et al., 2006). Applications cover many branches of science as virtually any multidimensional dynamical system may be considered a network of dynamically interacting components. Beyond climate science, network methods have been employed for the analysis of financial markets (Lux and Marchesi, 1999), social dynamics (Erbach-Schoenberg et al., 2014), neural activity (Zhou et al., 2006; Vertes et al., 2012), genetic regulatory systems (de Jong, 2002; Ho and Charleston, 2011), and transportation networks (Woolley-Meza et al., 2013), to name just a few examples.

Various types of graphs have been devised to mathematically describe differently networked systems. Among climate networks, one can find any of the examples given in Fig. 10.1: With different node and link types one can distinguish nodes from different atmospheric layers and intra-layer from inter-layer links (Donges et al., 2011); node weights are useful to take varying grid cell sizes into account (Zemp et al., 2014); link weights allow for the representation of varying strengths of connection between nodes (Berezin et al., 2012); and with directed links one can capture the direction of atmospheric flows (Boers et al., 2014). For the sake of simplicity, we will focus our derivations on undirected climate networks first. A generalization of our concepts to directed networks will be discussed towards the end of Sec. 10.2.

10.1. Climate Network Construction

Undirected climate networks are usually constructed as follows. In the first step, $i = 1, \dots, N$ local meteorological time series $x_i(t)$ are preprocessed to anomaly time series $y_i(t)$, often including some filtering in the time or frequency domain. Then, the relationship between any two of those anomaly time series is estimated using some *undirected* statistical dependence measure, which results in a *symmetric* $N \times N$ matrix of relationship coefficients r_{ij} . This matrix can already be interpreted as the representation of a fully connected undirected network of N nodes and with link weights r_{ij} . Statistical dependencies are calculated between anomaly time series $y_i(t)$ to have networks representing nontrivial spatial relationships of fluctuations around climatological mean values. If they were calculated between the precursor time series $x_i(t)$ they would mainly represent relationships between mean seasonal cycles.

Statistical dependence measures that have been used to construct climate networks include linear correlations (Tsonis and Roebber, 2004; Yamasaki et al., 2008) as well as nonlinear measures such as mutual information (Donges et al., 2009a; Barreiro et al., 2011), event synchronization (Malik et al., 2012; Boers et al., 2013), and transfer entropy (Runge et al., 2012). Given that atmospheric dynamics are nonlinear, dependences between time series can be expected to be nonlinear too. Following up this reasoning, Donges et al. (2009b) constructed surface air temperature networks with correlations and with mutual information, but did not find any major structural differences between them. Therefore, we stick to the simpler correlation measures where appropriate. In order to study

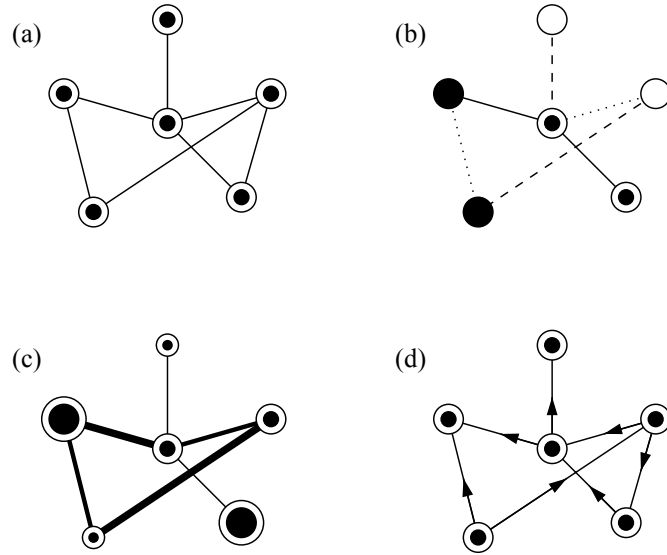


Figure 10.1.: Examples of climate network types. Undirected networks with (a) only a single node type and a single link type, (b) a number of discrete node and link types, and (c) varying node and link weights versus (d) a directed network (from Newman, 2003).

spatial relationships between binary extreme event time series, we employ the event synchronization, which was originally introduced to measure synchronicity and time delay patterns between electroencephalogram signals (Quiroga et al., 2002).

To simplify the network analysis, the matrix (r_{ij}) is usually further processed to a binary adjacency matrix with components $a_{ij} = 1$ if nodes i and j are connected and $a_{ij} = 0$ otherwise (Donges et al., 2009b; Simpson et al., 2013). These unweighted links are typically assigned according to the significance of the respective statistical relationship, i.e. by setting a_{ij} to 1 iff r_{ij} exceeds some threshold value. If the statistical dependence measure is such that r_{ii} represents a trivial relationship of a time series with itself, then a_{ii} is set to zero for all i . In this typical case (a_{ij}) represents a network that mathematicians call a *simple graph*.

In summary, undirected climate networks are typically constructed according to

$$\{x_i(t)\} \xrightarrow{P} \{y_i(t)\} \xrightarrow{S} (r_{ij}) \xrightarrow{T} (a_{ij}), \quad (10.1)$$

where P represents the preprocessing algorithm that turns the original time series into anomaly time series, S is the statistical dependence measure used to quantify undirected bilateral statistical relationships between anomaly time series, and T denotes the thresholding of statistical relationship coefficients that yields simple graph adjacency matrices.

An important trait of climate networks is that they are *spatially embedded*, which means that their nodes are associated with points in a metric space. The embedding can have a considerable effect on the network structure (Boccaletti et al., 2006; Donges, 2012). In particular, the strength (in the r_{ij} case) or existence (in the a_{ij} case) of a link between two nodes i and j is usually related to the distance $d(i, j)$ of the nodes. This relationship can be quantified by the dependence of the average link strength $\langle r_{ij} \rangle$ or link density $\langle a_{ij} \rangle$ on the node distance $d(i, j)$. Another consequence of the embedding is that climate network nodes typically represent subsets of the metric space that vary in size. This volumetric information can be taken into account by node weights (Heitzig et al., 2012).

10.2. Dissimilarity Measures for Climate Networks

We will now introduce new dissimilarity measures for climate networks represented by matrices of both the (r_{ij}) and the (a_{ij}) type. We are going to denote the two networks to be compared A and B , and we will assume them to have a common set of N nodes, which presumes that model output and observations are mapped onto a common grid or location set prior to network construction. Such a spatial interpolation of data prior to comparison is commonplace in climate model evaluations.

Given the correspondence of nodes between networks A and B , we can aim at a local network comparison, i.e. at the assessment of network dissimilarity from the perspective of each individual node/location. These local dissimilarities can then be depicted in the form of bias maps, and they can be spatially aggregated to obtain an estimate of the global network dissimilarity. With this picture in mind we are going to define local and global network dissimilarity measures in the following.

Please note that, in principle, we could as well work with network *similarity* instead of *dissimilarity* measures. The two are typically equivalent as for a bounded similarity measure $s(A, B) \in [0, 1]$ an equivalent dissimilarity measure is given by $d(A, B) = 1 - s(A, B)$. Yet we prefer to quantify network dissimilarity since it enables the aforementioned map plots of local dissimilarities, which shall resemble the bias maps found in typical climate model evaluation studies. We think that this increases the chances for the network approach to be appreciated by the climate model evaluation community.

The network science community has already tackled the problem of quantifying graph similarity from the perspective of individual nodes since potential applications are abundant. It has developed a concept termed *vertex similarity* and has applied it to compare nodes of the same (Jaccard, 1901; Leicht et al., 2006) and of different (Blondel et al., 2004; Zager and Verghese, 2008) networks. The older and simpler concept of structural equivalence considers nodes similar if they have many common network neighbors (Lorrain and White, 1971; Leicht et al., 2006) while the more recent concept of regular equivalence considers nodes similar if the nodes they are connected to are themselves similar (Blondel et al., 2004; Zager and Verghese, 2008). To make sense, the latter concept requires transitivity of similarity through network links and therefore does not apply to networks where nodes are linked iff the entities they represent are dissimilar. Since networks of this latter kind can occur in our context, as we are going to exemplify by anticorrelation climate networks in Ch. 13, we define local network dissimilarity measures in accordance with the concept of structural equivalence. To our knowledge, we are the first to employ this concept to quantify the (dis)similarity of nodes of different networks.

We will begin with the simplest case of simple graphs, continue with the cases of edge-weighted and node-weighted undirected graphs, and end with the most general case of directed graphs with and without edge and node weights.

10.2.1. Simple Graphs

Let us first recall some basic graph theoretical notions. A *simple graph* $G = (V, E)$ consists of a vertex set $V = \{1, \dots, N\}$ and an edge set $E = \{\{i, j\}: i, j \in V\}$. It can be represented by a symmetric binary $N \times N$ *adjacency matrix* (a_{ij}) with a zero diagonal and $a_{ij} = 1 \Leftrightarrow \{i, j\} \in E$. Nodes which are connected are called *neighbors*. The set of all nodes connected to node i is *i 's neighborhood*. The number of its neighbors is *i 's degree* k_i and can be written as

$$k_i = \sum_{j=1}^N a_{ij}. \quad (10.2)$$

The average degree over all nodes, divided by $N - 1$, is the *link density* ρ of the network,

$$N(N - 1)\rho = \sum_{i,j=1}^N a_{ij} = \sum_{i=1}^N k_i = 2|E|. \quad (10.3)$$

In other words, ρ is the probability to find a link between two randomly chosen nodes of the network.

Now let us consider two such simple graphs with adjacency matrices (a_{ij}^A) and (a_{ij}^B) . One way to compare them from the perspective of an individual node i is to compare the neighborhoods of i in the two networks. This can be done by comparing the i th columns or rows of (a_{ij}^A) and (a_{ij}^B) . A simple distance function for such binary vectors was proposed by Hamming (1950) based on the logical operation *exclusive or*, which, using arithmetic operations, can be written as

$$a_{ij}^A \text{ XOR } a_{ij}^B = |a_{ij}^A - a_{ij}^B| = (a_{ij}^A - a_{ij}^B)^2 = a_{ij}^A + a_{ij}^B - 2a_{ij}^A a_{ij}^B \quad (10.4)$$

for $a_{ij}^A, a_{ij}^B \in \{0, 1\}$. Apparently, XOR detects differences between binary variables, which Hamming (1950) used when he defined his binary vector distance as the sum over the exclusive ors of the vector components. Applying his idea to our problem of comparing network neighborhoods, we define the *Local Hamming Distance* (LHD) H_i between simple graphs A and B at node i as

$$H_i(A, B) = \sum_{j=1}^N a_{ij}^A \text{ XOR } a_{ij}^B. \quad (10.5)$$

The LHD counts the number of nodes, which are either a neighbor of i in network A but not in B or vice versa. It is thus equal to the minimal number of adjacency relation changes necessary to make the two neighborhoods match. A global network dissimilarity measure corresponding to the LHD is easily defined by

$$H(A, B) = \sum_{i=1}^N H_i(A, B) = \sum_{i,j=1}^N a_{ij}^A \text{ XOR } a_{ij}^B, \quad (10.6)$$

and we call $H(A, B)$ the *Global Hamming Distance* (GHD) of A and B (cf. Zhou et al., 2006; Donges et al., 2009b).

Figure 10.2(c) shows LHDs between regional climate networks over South America with degree fields displayed in Figs. 10.2(a) and (b). We observe large LHDs in areas with large degree discrepancies, which is a behavior we expect from a local network dissimilarity measure. A less ideal behavior becomes apparent over the Atlantic off the Argentinian coast, where both degree fields concordantly display some fine structure that is related to the Malvinas Current. We observe that the LHD field features the same fine structure, which hints at a positive correlation between LHD and degree.

This correlation is unfavorable because it implies that the LHD has no absolute meaning. Imagine two nodes i, j with $k_i^A = k_i^B \neq k_j^A = k_j^B$. Equal LHD values at these nodes would mean different relative agreements of neighborhoods. It is therefore difficult to interpret LHD values without considering the degrees. We would like to have a more intuitive difference measure which quantifies the dissimilarity of neighborhoods relative to their size. An equivalent problem has been encountered by those studying vertex similarity concepts (Leicht et al., 2006). While, to our knowledge, the network science community has always made do with ad hoc normalizations (Jaccard, 1901; Salton, 1989; Ravasz et al., 2002), we take a different approach in the following.

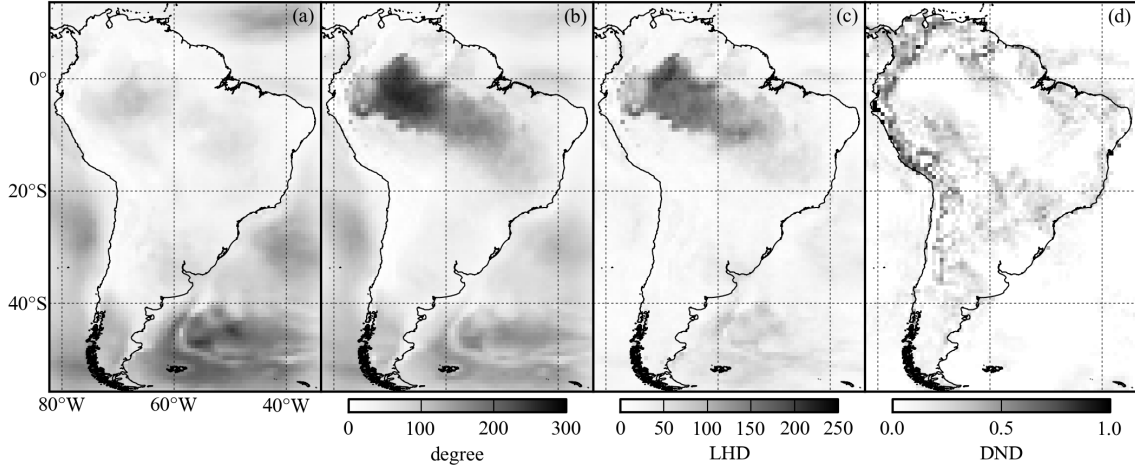


Figure 10.2.: Comparison of example climate networks based on 1996–2011 DJF 2 m temperature anomaly time series over South America (cf. Ch. 12). Panels (a) and (b) show degree fields of such networks constructed from ERA-Interim reanalysis data and from CCLM simulation data, respectively. Panels (c) and (d) show Local Hamming Distances [Eq. (10.5)] and Degree-conditional Neighborhood Dissimilarities [Eq. (10.12)] between these networks, respectively. Note that the grayscale below (b) is also valid for (a).

Our starting point is a statistical null model which explains the observed LHD-degree dependence: Let i be some fixed node with degrees k_i^A in graph A and k_i^B in graph B , and let us assume i 's neighborhoods in A and B to be statistically unrelated. This can be modeled considering $a_{i\neq j}^A$ and $a_{i\neq j}^B$ to be random binary variables that are statistically independent between networks and equal to one with identical probability within networks. Using Eq. (10.4), this null model yields an LHD expectation value of $\langle H_i(A, B) \rangle = k_i^A + k_i^B - 2k_i^A k_i^B / (N - 1)$.

Beyond illustrating the relationship between LHD and degree, this null model can be used to define a new local network dissimilarity measure, which is degree-independent. To that end, we relate the actually measured LHD value $H_i(A, B)$ to the null model probability distribution of possible LHD values for the degrees k_i^A and k_i^B . More specifically, $H_i(A, B)$ is mapped to its null model p -value, i.e. to the probability of the LHD to take a value less than or equal to $H_i(A, B)$, if i 's neighborhoods of size k_i^A in A and k_i^B in B were statistically unrelated.

We now derive a formula for those p -values, i.e. we derive the Cumulative Distribution Function (CDF) of LHDs generated by our null model. According to (10.2) and (10.4) we can write

$$H_i(A, B) = k_i^A + k_i^B - 2 \sum_{j \neq i} a_{ij}^A a_{ij}^B. \quad (10.7)$$

The sum in Eq. (10.7) counts the number of common neighbors of i in A and B . We denote this number by $N_i(A, B)$ and have

$$N_i(A, B) = \frac{1}{2} (k_i^A + k_i^B - H_i(A, B)). \quad (10.8)$$

For fixed k_i^A and k_i^B , this implies a one-to-one correspondence between $N_i(A, B)$ and $H_i(A, B)$, with changes of the former by +1 corresponding to changes of the latter by -2 . Let us denote LHDs

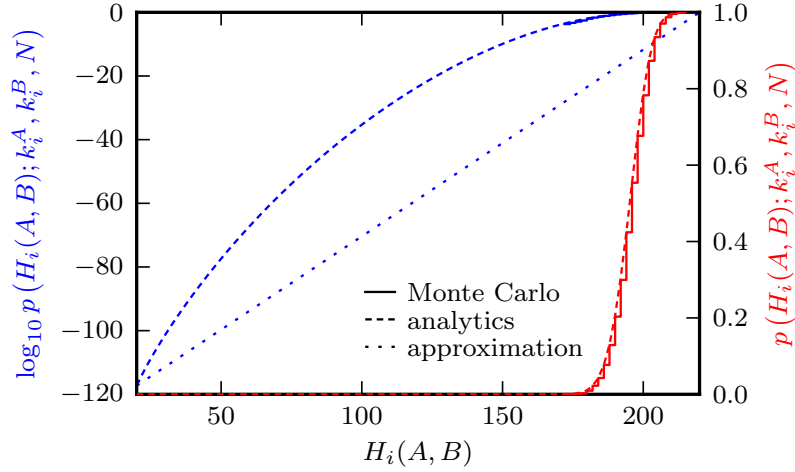


Figure 10.3.: Null model p -values of $H_i(A, B)$ for $k_i^A = 120$, $k_i^B = 100$, $N = 1000$, both from 10 000 Monte Carlo trials (solid lines) and from Eq. (10.10) (dashed lines). The dotted line is the $\log p$ approximation used in Eqs. (10.21) and (10.23).

generated with the null model by $h = k_i^A + k_i^B - 2n$, in the spirit of Eq. (10.8). The null model probability of node i to have exactly n common neighbors in the two networks is equal to the probability of having exactly n successes in k_i^B draws without replacement from a population of size $N - 1$ containing k_i^A successes. This probability is given by

$$P(n; k_i^A, k_i^B, N) = \binom{k_i^A}{n} \binom{N-1-k_i^A}{k_i^B-n} \binom{N-1}{k_i^B}^{-1}, \quad (10.9)$$

the probability density function of a hypergeometric distribution (Graham et al., 1989; Petkovšek et al., 1996). Note that $P(n; k_i^A, k_i^B, N)$ is symmetric with respect to exchanging k_i^A with k_i^B . The desired p -value formula results from (10.9) via

$$\begin{aligned} p(H_i(A, B); k_i^A, k_i^B, N) &= P(h \leq H_i(A, B); k_i^A, k_i^B, N) \\ &= P(n \geq N_i(A, B); k_i^A, k_i^B, N) \\ &= \sum_{n=N_i(A, B)}^{\min\{k_i^A, k_i^B\}} P(n; k_i^A, k_i^B, N). \end{aligned} \quad (10.10)$$

In order to numerically evaluate this complementary CDF of a hypergeometric distribution, we use the HyperQuick algorithm devised by Berkopec (2007). This algorithm has the advantage of being easily logarithmized, which is important because of the following observation. The p -values of LHDs between climate networks from observational and simulated meteorological data studied in Ch. 12 and Ch. 13 turn out to typically be many orders of magnitude smaller than one. In other words, the climate models studied here are much better than our null model. To still be able to reasonably visualize p -values, we move to their logarithms. The agreement of our analytical result for $p(H_i(A, B); k_i^A, k_i^B, N)$ and its Monte Carlo simulation is exemplified in Fig. 10.3.

Unfortunately, $\log p$ is degree-dependent, again. For instance, for its minimum value

$$\begin{aligned} \min_h \log p(h; k_i^A, k_i^B, N) &= \log P(\min\{k_i^A, k_i^B\}; k_i^A, k_i^B, N) \\ &= \sum_{i=0}^{\min\{k_i^A, k_i^B\}-1} \log \frac{\max\{k_i^A, k_i^B\} - i}{N - 1 - i} \end{aligned} \quad (10.11)$$

we find that, per simultaneous increment of both degrees, $\min_h \log p$ decreases by approximately $-\log \rho$ for small link densities ρ . To overcome this problem, we rescale $\log p$ by its minimum value, thus defining a new local network difference measure

$$d_i(A, B) = 1 - \frac{\log p(H_i(A, B); k_i^A, k_i^B, N)}{\min_h \log p(h; k_i^A, k_i^B, N)}, \quad (10.12)$$

which we call the *Degree-conditional Neighborhood Dissimilarity* (DND). As Fig. 10.2 exemplifies, the DND frees the LHD from its degree correlation. Note that $d_i(A, B)$ is only defined if k_i^A and k_i^B are both positive. The definition is independent of the base of the logarithm. Note also that an equivalent *Degree-conditional Neighborhood Similarity* can easily be defined by $s_i(A, B) = 1 - d_i(A, B)$.

The DND can only take values in $[0, 1]$, with a value of zero (one) meaning maximally (minimally) overlapping neighborhoods of node i in the two networks, given the degrees. Note that $d_i(A, B) = 0$ does not imply a local agreement between networks. Rather, it means the greatest possible agreement given the degrees. Therefore, while a zero LHD implies a zero DND, the converse is not true. The DND should therefore always be considered together with either the LHD or the degrees of the compared networks.

Another advantage of the DND over the LHD pertains to artifacts originating from the spatial embedding of climate networks (Rheinwalt et al., 2012). As we can see in Fig. 10.2, nodes that are closer to the domain boundary tend to have smaller degrees, and owing to the correlation between the degrees and the LHD, this boundary effect is passed on to the LHD. Per construction, the DND does not show this artifact.

10.2.2. Edge-Weighted Graphs

As outlined in the Sec. 10.1, simple graphs representing atmospheric dynamics usually result from a binarization of a matrix of statistical relationship coefficients r_{ij} . Such a procedure artificially degrades the network information content. Moreover, it usually involves the introduction of binarization parameters, which many properties of the resulting simple graphs depend on.

In the model evaluation context it may be desirable to omit this problematic procedure, i.e. to directly evaluate the simulation accuracy with respect to the (r_{ij}) matrix. To that end, a dissimilarity measure for such matrices is needed. We will now introduce one for r_{ij} being Pearson correlation coefficients.

In formal analogy to the Local Hamming Distance, we define the *Local Correlation Distance* (LCD) C_i between networks A and B at node i as

$$C_i^2(A, B) = \sum_{j \neq i} (F(r_{ij}^A) - F(r_{ij}^B))^2, \quad (10.13)$$

$$\text{with } F: (-1, 1) \rightarrow (-\infty, \infty), r \mapsto \operatorname{arctanh} r. \quad (10.14)$$

The use of the Fisher transformation (Fisher, 1915) F in the LCD definition is motivated as follows. The confidence interval width of Pearson correlation estimates depends on their value. An r_{ij} value around 0 usually has a wider confidence interval than a value close to ± 1 . Therefore, at correlation coefficient values around 0, we expect $|r_{ij}^A - r_{ij}^B|$ to be greater than at values close to ± 1 . The use of Fisher transformed coefficients balances this disparity. For normally distributed time series, the standard estimation error of $F(r_{ij})$ is approximately independent of r_{ij} (Fisher, 1915, 1921; Fieller et al., 1957; Fieller and Pearson, 1961). Thus, in definition (10.13), differences of r_{ij} values close to ± 1 contribute as much to $C_i(A, B)$ as those at values around 0. Furthermore, using the nontransformed correlation coefficients in (10.13) would make $C_i(A, B)$ dependent on $\sum_{j \neq i} r_{ij}^X$, $X = A, B$, analogously to the relationship between LHD and degree in the case of simple graphs. Employing the Fisher transformation prevents such a dependency and hence renders a DND analog for correlation networks unnecessary.

For later reference, we define the *Global Correlation Distance* (GCD) C of networks A and B by

$$C^2(A, B) = \sum_i C_i^2(A, B) = \sum_{i, j \neq i} (F(r_{ij}^A) - F(r_{ij}^B))^2. \quad (10.15)$$

In principle, the ansatz just outlined for networks based on Pearson correlations can be applied to networks based on any measure of statistical relationship. However, as we have tried to argue, prior to any distance calculation, relationship coefficients should be transformed such that their uncertainties become value-independent. For measures of statistical relationship that currently lack an estimation error theory similar to that of Fisher (1915) for correlations, this should be seen as an incentive to close the research gap.

10.2.3. Node-Weighted Graphs

The time series behind climate network nodes often represent atmospheric dynamics averaged over grid cells of varying size. For example, the cells of a geographical grid [cf. Fig. 2.1(a)] decrease in area as latitude increases. Instead of counting the number of grid cells a given grid cell is connected to, it makes more sense to measure the total area represented by the grid cells a given grid cell is connected to (Tsonis et al., 2006). In mathematical terms, this can be achieved by considering a node-weighted degree

$$k_i^* = \sum_j a_{ij} w_j \quad (10.16)$$

with node weights w_i proportional to grid cell areas. Heitzig et al. (2012) have formalized this idea to the concept of *node splitting invariance* and provide a recipe for defining a node-weighted version of any network measure. We basically follow their idea to introduce node-weighted variants of our network dissimilarity measures.

We define the node-weighted LHD H_i^* and GHD H^* according to

$$H_i^*(A, B) = \sum_j (a_{ij}^A \text{ XOR } a_{ij}^B) w_j, \quad (10.17)$$

$$H^*(A, B) = \sum_i w_i H_i^*(A, B) = \sum_{i, j} w_i (a_{ij}^A \text{ XOR } a_{ij}^B) w_j, \quad (10.18)$$

and observe that H^* penalizes link misplacements in proportion to the product of the areas of the

grid cells in question. Analogously, we define the node-weighted LCD C_i^* and GCD C^* by

$$C_i^{*2}(A, B) = \sum_{j \neq i} (F(r_{ij}^A) - F(r_{ij}^B))^2 w_j, \quad (10.19)$$

$$C^{*2}(A, B) = \sum_i w_i C_i^{*2}(A, B) = \sum_{i, j \neq i} w_i (F(r_{ij}^A) - F(r_{ij}^B))^2 w_j. \quad (10.20)$$

Deriving a node-weighted version of the DND is less straightforward. In formal analogy to Eq. (10.12), $d_i^*(A, B)$ should be a function of the node-weighted LHD $H_i^*(A, B)$, the node-weighted degrees k_i^{*A} , k_i^{*B} , and the number of nodes N . In contrast to k_i , however, any rearrangement of i 's neighborhood potentially changes k_i^* , depending on the spectrum of node weights. The combinatoric null model approach that led from LHD to DND is thus unsuitable for a derivation of $d_i^*(A, B)$. We could numerically compute the node-weighted null model CDF using Monte Carlo techniques, but a general closed-form analytical solution appears to be out of reach.

As the node-weighted DND should equal the DND in the case of constant node weights, we can nevertheless provide an approximation to the unknown $d_i^*(A, B)$ based on an approximation to $d_i(A, B)$: In Fig. 10.3 we observe that the function $\log p(h; k_i^A, k_i^B, N)$ may be approximated by a straight line through its extreme points, preserving its strict monotonicity and range of values. These extreme points are the least and greatest possible LHD value for fixed degrees k_i^A, k_i^B . The least possible LHD value occurs in the case of a greatest possible neighborhood overlap and is equal to $|k_i^A - k_i^B|$. The greatest possible LHD value goes along with a least possible neighborhood overlap and is given by $k_i^A + k_i^B$ if this number is less than N . In this case, the linear approximation of $\log p$ in Eq. (10.12) yields

$$d_i(A, B) \approx \frac{H_i(A, B) - |k_i^A - k_i^B|}{k_i^A + k_i^B - |k_i^A - k_i^B|} = \frac{H_i(A, B) - |k_i^A - k_i^B|}{2 \min\{k_i^A, k_i^B\}} \quad (10.21)$$

$$= 1 - \frac{N_i(A, B)}{\min\{k_i^A, k_i^B\}}, \quad (10.22)$$

and the expression (10.22) shows that in this case and approximation, the DND is equivalent to the structural vertex similarity measure introduced by Ravasz et al. (2002). If $k_i^A + k_i^B \geq N$, then the roles of zeros and ones in the LHD calculation swap, and the greatest possible LHD value becomes $(N - 1 - k_i^A) + (N - 1 - k_i^B)$. In this case we obtain

$$d_i(A, B) \approx \frac{H_i(A, B) - |k_i^A - k_i^B|}{2N - 2 - k_i^A - k_i^B - |k_i^A - k_i^B|} = \frac{H_i(A, B) - |k_i^A - k_i^B|}{2(N - 1 - \max\{k_i^A, k_i^B\})}. \quad (10.23)$$

Since the hypergeometric distribution is log-concave (Hörmann, 1994), $\log p(h; k_i^A, k_i^B, N)$ is a concave function in h (Bagnoli and Bergstrom, 2005). Consequently, the approximate DND values are always less than or equal to their true counterparts. Following the same line of thought and using $W_i = \sum_{j \neq i} w_j$, we can define an analogous approximation to the node-weighted DND by

$$d_i^*(A, B) \approx \begin{cases} \frac{H_i^*(A, B) - |k_i^{*A} - k_i^{*B}|}{2 \min\{k_i^{*A}, k_i^{*B}\}} & \text{if } k_i^{*A} + k_i^{*B} \leq W_i, \\ \frac{H_i^*(A, B) - |k_i^{*A} - k_i^{*B}|}{2(W_i - \max\{k_i^{*A}, k_i^{*B}\})} & \text{otherwise.} \end{cases} \quad (10.24)$$

10.2.4. Directed Graphs

Generalizations of our network dissimilarity measures to the case of directed graphs can be obtained by treating outgoing and incoming links separately. In this section we will consider networks with-out node weights only, both to keep things concise and because a generalization to the case with node weights is straightforward.

Let r_{ij} or a_{ij} describe a link that goes out of i and comes into j . With this convention, the i th row (column) of (r_{ij}) or (a_{ij}) represents the outgoing (incoming) links of node i . The numbers of outgoing and incoming links, termed the *out-degree* k_i^+ and the *in-degree* k_i^- of node i , respectively (Boccaletti et al., 2006), are given by

$$k_i^+ = \sum_j a_{ij} \quad \text{and} \quad k_i^- = \sum_j a_{ji}. \quad (10.25)$$

We can define the out-LHD H_i^+ and the in-LHD H_i^- between graphs A and B at node i by

$$H_i^+(A, B) = \sum_j a_{ij}^A \text{ XOR } a_{ij}^B \quad \text{and} \quad H_i^-(A, B) = \sum_j a_{ji}^A \text{ XOR } a_{ji}^B \quad (10.26)$$

and see that the GHD can be reobtained via

$$H(A, B) = \sum_i H_i^+(A, B) = \sum_i H_i^-(A, B). \quad (10.27)$$

The corresponding out-DND d_i^+ and in-DND d_i^- are then simply given by

$$d_i^\pm(A, B) = 1 - \frac{\log p(H_i^\pm(A, B); k_i^{\pm A}, k_i^{\pm B}, N)}{\min_h \log p(h; k_i^{\pm A}, k_i^{\pm B}, N)}, \quad (10.28)$$

based on the same formulas as the undirected DND [Eq. (10.12)]. For edge-weighted graphs, out-LCD and in-LCD can be defined analogously to out-LHD and in-LHD.

10.2.5. Normalization to Network Size

All network dissimilarity measures devised so far are extensive, i.e. they can be expected to grow with N if simultaneously the link density ρ is kept constant. To obtain intensive versions of our dissimilarity measures we need to normalize the various sums in their definitions by the number of summands. We are going to denote the intensive dissimilarity measures by the lowercase version of the letter that denotes their extensive brothers, which, by the way, is why we used a lowercase letter for the DND in the first place. If we assume $\sum_i w_i = N$, which is equivalent to an average node weight of 1, we can even define intensive dissimilarity measures for node-weighted graphs without any additional complication, according to

$$h_i^*(A, B) = \frac{H_i^*(A, B)}{N-1}, \quad h^*(A, B) = \frac{H^*(A, B)}{N(N-1)} = \frac{1}{N} \sum_i w_i h_i^*(A, B), \quad (10.29)$$

$$c_i^{*2}(A, B) = \frac{C_i^{*2}(A, B)}{N-1}, \quad c^{*2}(A, B) = \frac{C^{*2}(A, B)}{N(N-1)} = \frac{1}{N} \sum_i w_i c_i^{*2}(A, B). \quad (10.30)$$

10.3. Random Network Models

Random network models will help us to develop a feeling for the magnitude of dissimilarity we can expect between climate networks constructed from simulated and from observational reference data. Using such models, we can generate networks that have certain properties in common with the reference network but whose structure is otherwise random, to then quantify the dissimilarity between these random networks and the reference network. This tells us which performance could be expected from the evaluated climate models if they reproduced the structure of the reference network with respect to those certain properties alone. We are going to employ the following three random network models to obtain such benchmarks.

Erdős-Rényi (ER) Model With this most simple random network model we mimic the performance of a worst possible climate model by generating simple graphs which have nothing in common with the reference graph but the link density ρ (Erdős and Rényi, 1959). Links are randomly assigned such that every nondiagonal component a_{ij} of the adjacency matrix equals 1 with uniform probability ρ . Using (10.3) and (10.4), we can easily compute the expectation value of the normalized GHD h between a simple graph A and ER random graphs B with the same link density $\rho = \langle a_{i \neq j}^B \rangle$ according to (cf. Donges et al., 2009b)

$$\begin{aligned} N(N-1) \langle h(A, B) \rangle &= \langle H(A, B) \rangle = 2N(N-1)\rho - 2 \sum_{i,j} a_{ij}^A \langle a_{ij}^B \rangle \\ \Rightarrow \langle h(A, B) \rangle &= 2\rho - 2\rho^2 = 2\rho(1 - \rho). \end{aligned} \quad (10.31)$$

Since $h(A, B)$ is the average of $h_i(A, B)$ over all nodes i , the normalized LHD between a simple graph and ER random graphs with the same link density is of the same average magnitude.

Viger-Latapy (VL) Model We use this model to generate connected simple graphs with the same degree sequence (k_i) as the reference graph (Viger and Latapy, 2005). Per definition, the graphs generated by the VL model also conserve the link density of the reference network, so we can expect them to be closer to the latter than the ER random graphs.

Spatially Embedded Random Network (SERN) Model This model was introduced to estimate the effects of spatial node embedding on network structure (Barnett et al., 2007). Recently, it was used to study the effect of domain boundaries on network measures in regional climate networks (Rheinwalt et al., 2012). Graphs generated with the SERN model have the same link density and the same geographical link length distribution as the reference graph, with *geographical link length* meaning the geographical distance between the nodes/locations connected by a given link. Since the degree sequence is not conserved by this model it is not clear a priori if the SERNs will be closer to or farther from the reference graph than the VL random graphs.

11. Statistical Downscaling and STARS

In Ch. 4 we introduced dynamical downscaling with RCMs such as CCLM as a means to bridge the resolution gap between available GCM output and required climate impact model input. Another approach to the solution of this problem is *statistical downscaling*. Its main advantage over dynamical downscaling is that it is computationally much less expensive. Reviews of statistical downscaling methods have been given by Wilby and Wigley (1997); Xu (1999), and Maraun et al. (2010). Classical tools such as regression models, weather pattern-based techniques, and conditional weather generators exploit statistical relationships between historical coarse- and high-resolution weather data to downscale GCM future climate projections.

The statistical downscaling tool we employ here is the STatistical Analogue Resampling Scheme (STARS) version 2.4. It was devised as a simple means of generating ensembles of, first local and later regional, future climate projections under global warming scenarios by resampling from past daily meteorological observations such that a prescribed temperature trend is matched (Werner and Gerstengarbe, 1997; Orłowsky et al., 2008). Since the resampling is conditioned by the temperature trend only, STARS is located somewhere between classical statistical downscaling methods and stand-alone climate modeling approaches (Orłowsky et al., 2010).

Any climate simulation generated with STARS consists of a day-to-day mapping from the simulation period, characterized by the prescribed temperature trend, to the observation period. This means that each day of the simulation period is assigned some day from the observation period with its respective meteorological data. The conditional resampling typically yields different assignment probabilities for the different observation days; under a warming scenario, warmer days are more likely to be assigned. The day-to-day mapping is applied to every meteorological variable in all locations, which ensures physical consistency across variables and locations but for any such inconsistency in the observations.

A Monte Carlo method is used to generate the day-to-day mapping based on temperature data only. The way this is done in single-location, i.e. local applications is sketched in Fig. 11.1. In the first step, the scheme generates a *first approximation* by creating an ensemble of yearwise resamplings of the observational daily temperature time series (i.e. entire years are drawn at random with replacement) and then choosing the resampling whose trend is closest to the prescribed trend. In the second step, this first approximation is stochastically fine-tuned by iteratively exchanging 12-day⁴ blocks of data so as to further improve the trend fit. The main difference in multi-location, i.e. regional applications is that the trend comparisons, the yearwise resamplings of step one, and the block exchanges of step two all become multidimensional. To reduce the computational cost of regional applications, usually, a cluster analysis is used to identify climatologically similar locations and only one representative location per cluster is considered in the construction of the day-to-day mapping, with a location being considered representative for a cluster if its climatology is closest to this cluster's centroid climatology. For further details of the resampling scheme see Orłowsky et al. (2008).

⁴In principle, the block length is a freely adjustable model parameter, but for the STARS simulations we refer to in the following two sections, the default value of 12 days was applied. Experience tells that this is a reasonable choice with regard to the conservation of persistence in weather time series.

11. Statistical Downscaling and STARS

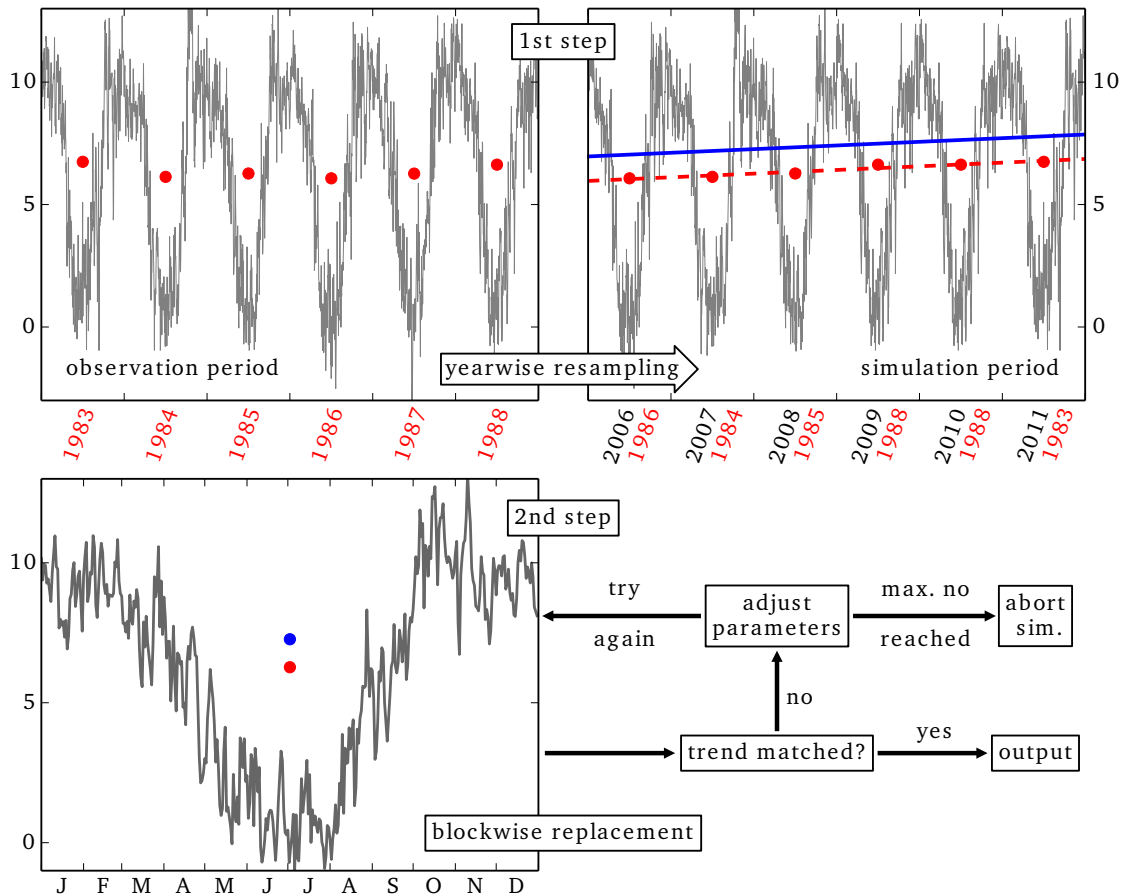


Figure 11.1.: Basic principle of STARS (contributed by Jan H. Feldhoff): At first (top panel), entire years from the observation period are resampled for their yearly means (red dots) to approximate a prescribed trend line (blue). Then, by iteratively replacing 12-day blocks (bottom panel), the resulting time series is further tuned to improve the matching of the actual (red dot) and prescribed (blue dot) yearly mean values.

The STARS approach towards climate modeling has two fundamental limitations per definition. Firstly, the quality of the model output data is limited by the quality of the model input data, and secondly, as resampling cannot create any new weather situations, the applicability of STARS is limited to similar input and output climates. Quite recently, Wechsung and Wechsung (2014) exposed possible consequences of an ignorance of the latter limitation. They mathematically proved that, essentially, STARS translates short-term interannual covariabilities between temperature and its covariables into long-term climate trends. Using the example of centennial STARS climate projections for Germany they revealed that this conceptual flaw of the scheme yields reputedly unrealistic centennial precipitation and radiation trends. Fortunately, these findings do not devalue the results we present in the following since we employ decadal STARS climate projections for illustrational purposes only.

12. Bivariate versus Univariate Climate Model Evaluation

In a first application we want to demonstrate how the bivariate network approach to climate model evaluation complements conventional univariate approaches. To that end, we compare the performances of the regional climate models CCLM and STARS over South America, measuring these performances by the Global Hamming Distance of climate networks versus root-mean-square deviations of climatological mean values and variances. In other words, we evaluate the simulation quality of bivariate spatial covariabilities versus univariate means and variabilities. We include two RCMs in the evaluation to get model rankings for each combination of error measure, season, and variable considered. Two error measures are proven complementary if we can show that their application yields different model rankings for a certain variable in a certain season. To keep the study simple, we use ERA-Interim (ERA-I) reanalysis data as our observational reference, as initial and lateral boundary conditions for the dynamical downscaling with CCLM, and as input data for the statistical resampling with STARS. We consider 2 m temperature, precipitation, 500 hPa geopotential height, and sea level pressure in austral summer and winter.

12.1. Study Design

In the following we outline our study design in detail. We first describe the simulation setup of CCLM and STARS, then introduce our network construction methods, thereafter define our model performance measures, and finally sketch how we enable a fairer model intercomparison using a bootstrap.

12.1.1. Climate Model Simulations

As a rule of thumb, the length of a STARS simulation period should not exceed the length of the observation period from which data is fed into the model. This rule is supposed to prevent unnaturally low variability in the model output. Since ERA-I data are available from 1979, Jan H. Feldhoff simulated the period from 1996 to 2011 based on daily input data from 1979 to 1995 and the reanalysis temperature trend from the simulation period. The simulation domain (cf. Fig. 12.1) is a latitude-longitude box from 13.7°N to 55.8°S and from 82.3°W to 33.8°W. Given the native ERA-I grid resolution of approximately 0.7° in both latitude and longitude, this domain contains exactly $N = 7000$ grid cells. Jan used STARS version 2.4 in combination with 8 representative locations which were determined by clustering the local time series with respect to their temperature and precipitation climatology (cf. Ch. 11). By running the scheme multiple times, he generated an ensemble of 200 climate realizations.

The CCLM simulation was set up with the IS configuration, which we found to yield the best performance over South America in Pt. I. We ran the model over the CORDEX domain again (cf. Fig. 12.1), but this time covering the period 1979 to 2011 to let the model spin up properly during the first 17 years of simulation. For the evaluation, the model output from 1996 onwards is temporally

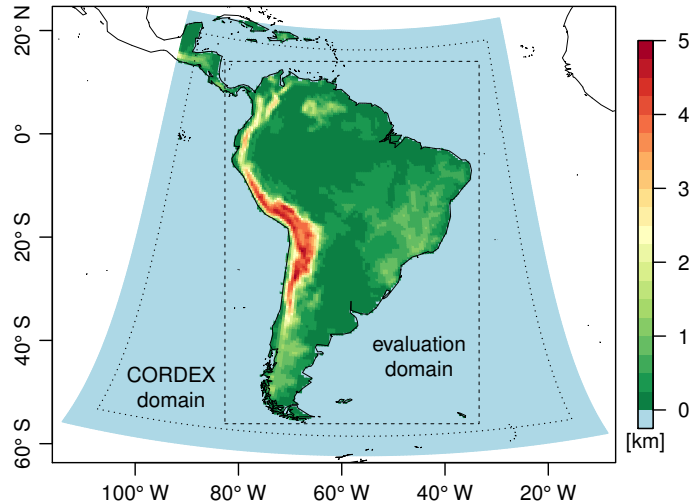


Figure 12.1.: CCLM's domain of computation including the sponge frame (colored), the CORDEX South America domain (dotted), and the common domain of evaluation (dashed), which is also the STARS simulation domain. Colors indicate surface elevation.

aggregated to daily mean values, which are then interpolated back to the coarser ERAI grid, conservatively (Jones, 1999) in the case of precipitation and bilinearly otherwise. Note that since STARS was set up to resample ERAI data its output is on the ERAI grid already.

12.1.2. Network Construction

We construct undirected climate networks from austral summer (DJF) and winter (JJA) space-time series $x_i(t)$ of daily mean 2 m temperature (T2M), precipitation (PREC), 500 hPa geopotential height (Z500), and sea level pressure (SLP). We choose T2M and PREC because these are the surface variables of greatest importance to the biosphere and the anthroposphere, and Z500 and SLP since these represent the atmospheric circulation in the middle troposphere and at the earth's surface, respectively.

Our construction methods follow the general recipe given in Sec. 10.1: (i) To make our time series $x_i(t)$ represent synoptic weather situations, we filter them with a central moving average of length $l = 7$ days. (ii) From these smoothed time series we compute anomalies $y_i(t)$ with respect to local climatological mean time series. (iii) Statistical relationships between any two of the anomaly time series are quantified by linear correlation coefficients r_{ij} . (iv) These coefficients are thresholded such that only the 1% most positive correlations are represented by links in a corresponding simple graph. Note that a link density of $\rho = 0.01$ is considered an effectual trade-off between structural richness and statistical significance (Donges et al., 2009b). Sensitivities of our results to the parameters l and ρ are discussed in Sec. 12.2.3.

Steps (ii) and (iii) of the construction procedure need some special attention because their details differ between T2M, Z500, and SLP on the one hand, and PREC on the other hand. In order to conduct step (ii), we need an approximation of the climatological mean time series at each location in daily resolution, which we construct by calculating the 1996–2011 mean values of the moving average time series for each calendar day, and further smoothing the resulting time series with a 7-day Gaussian filter to account for the rather short evaluation period.

For the practically unbound variables T2M, Z500, and SLP we *subtract* the climatological mean time series from the moving average time series to obtain approximately normally distributed anomaly time series $y_i(t)$. Undirected statistical relationships between the latter are quantified by *Pearson correlation coefficients* (Pearson, 1895).

In the case of PREC, which has a natural lower bound of zero, we *divide* the moving average time series by the climatological mean time series instead of subtracting it. Since the resulting anomaly values are not normally distributed (Li et al., 2013), we quantify statistical relationships by *Spearman rank correlation coefficients* (Spearman, 1904), handling ties according to the mid-rank method (Kendall, 1945). We prefer this division by climatological daily values over their subtraction, because only the scaling guarantees a common rank of all zero precipitation events. Moreover, since mean and variance of stationary precipitation time series can be well reproduced with exponential distributions (Li et al., 2013), the scaling makes the anomaly time series approximately homoscedastic in time. To avoid division by zero, we define a minimum climatological value of 0.1 mm/day, which we divide by whenever it is underrun. We chose this value since it is usually referred to as the smallest measurable daily precipitation amount. In our data, this case actually occurs only in northern Chile and over the adjacent part of the Pacific ocean.

It should be noted that climate networks are often constructed by thresholding the matrix of the absolute values of correlation coefficients (Tsonis and Roebber, 2004; Donges et al., 2009a,b). In the context of network comparison, however, this could lead to the problematic situation in which, for two networks with adjacency matrices (a_{ij}^A) and (a_{ij}^B) , $a_{ij}^A = 1$ is due to a positive correlation while $a_{ij}^B = 1$ is due to a negative correlation. Hence, although the relation of i to j is of wholly different nature in the two networks, a comparison of them would yield agreement. In order to prevent this case we focus on positive correlations.

12.1.3. Bivariate and Univariate Model Error Measures

Our network dissimilarity measure of choice for this study is the normalized node-weighted Global Hamming Distance (GHD) h^* [cf. Eqs. (10.18) and (10.29)]. Node weights w_i are introduced to take into account grid cell sizes, which vary considerably between the equator and the southern domain boundary. Provided that grid cell i is at latitude ϕ_i , we set $w_i \propto \cos(\phi_i)$, with the factor of proportionality chosen such that $\sum_i w_i = N$.

We evaluate CCLM and STARS in the conventional univariate way by the Root-Mean-Square Error (RMSE; Willmott, 1981) of climatological mean values and the Root-Mean-Square Log Error (RMSLE; Golding, 1998; Gregg and Casey, 2004) of climatological standard deviations. To ensure comparability to the node-weighted GHD, we use node-weighted versions e^* of the RMSE and l^* of the RMSLE. For observed (A) and simulated (B) spatial fields of climatological mean values $\mu_i = \langle x_i(t) \rangle_t$ and variances $\sigma_i^2 = \langle (x_i(t) - \mu_i)^2 \rangle_t$, these are defined by

$$e^{*2}(A, B) = \frac{1}{N} \sum_{i=1}^N w_i (\mu_i^A - \mu_i^B)^2 \quad \text{and} \quad l^{*2}(A, B) = \frac{1}{N} \sum_{i=1}^N w_i \left(\log \frac{\sigma_i^A}{\sigma_i^B} \right)^2. \quad (12.1)$$

The measures h^* , e^* , and l^* are comparable in that they are equal to zero in the case of perfect agreement and grow with disagreement. They are complementary in that they are based on distinct features of the underlying space-time series, namely the mean value and variance fields in the case of e^* and l^* , and the spatial correlation matrix in the case of h^* .

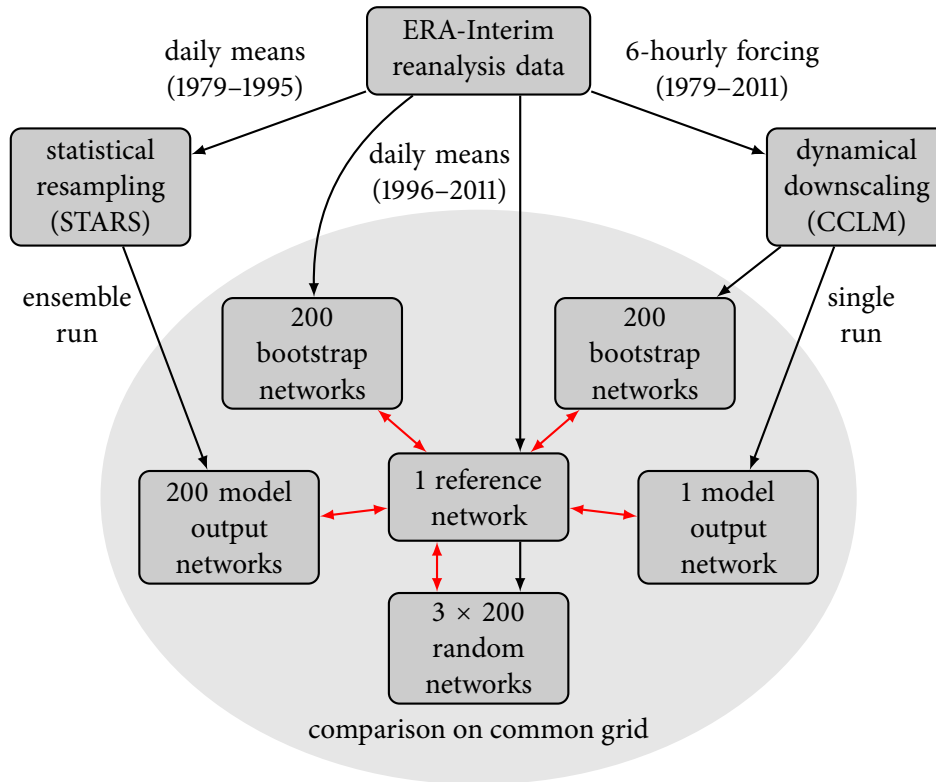


Figure 12.2.: Schematic diagram of our model evaluation study in which regional climate simulations with CCLM and STARS are both driven by and evaluated against ERAI reanalysis data. Climate networks for different variables and seasons are constructed after all model output has been interpolated onto a common grid. The inclusion of networks from bootstrapped ERAI and CCLM time series enables a fair model intercomparison of CCLM and STARS. Random networks that mimic selected properties of the ERAI reference network are generated to provide baseline performances. The red double-headed arrows indicate network comparisons with the Global Hamming Distance.

12.1.4. A Fairer Model Intercomparison with Bootstraps

Before we begin with our evaluation of CCLM and STARS, we still need to address a fundamental difference between the climate simulations done with the two models. Since the CCLM simulation is driven with reanalysis data, it more or less precisely replicates the weather history of the evaluation period. STARS, in contrast, scrambles its input data, which implies that, even if the resampling scheme was fed with data from the evaluation period, its output would only have the correct chronology with negligibly small probability. Since we evaluate both models against ERAI data from the evaluation period, this will result in a performance advantage for CCLM as long as there is interannual variability in the data.

To overcome this bias in our evaluation study design, we need to somehow adjust the CCLM and STARS simulations with respect to their chronological order. Because fitting the STARS simulations with any fixed chronology is impossible, the only way is to strip the CCLM simulation of its correct chronology. If we did not have any computational constraints, that could be achieved by driving CCLM with an ensemble of resampled lateral boundary data. Alternatively, we can resample the

output data of our single CCLM run with some simplified version of STARS. As described in Ch. 11, in its first step, STARS randomly draws entire years of data with replacement. Such a resampling is known as *bootstrap* among statisticians (Efron, 1979).

Consequently, we bootstrap the CCLM output by randomly drawing entire seasons with replacement, such that the length of the bootstrapped time series equals the original, and apply this resampling synchronously to the whole output time series field to conserve spatial relationships. This way, we generate an ensemble of 200 STARS-like climate realizations, which we denote by CCLMb.

In the same manner, we bootstrap the ERAI data. With the resulting 200 ERAIb climate realizations we intend to quantify the optimum model performance in the sense that, in our setting, perfect CCLM and STARS simulations would yield statistics of $h^*(\text{ERAI}, \text{CCLMb})$ and $h^*(\text{ERAI}, \text{STARS})$ that resemble those of $h^*(\text{ERAI}, \text{ERAIb})$, and similarly for e^* and l^* . A graphic summary of the setup of our evaluation study is given in Fig. 12.2.

12.2. Results

In the first part of the results section, we focus on the network part of our evaluation study. Subsequently, we compare model performance rankings according to bivariate versus univariate error measures to demonstrate that the former do complement the latter in climate model evaluation studies. We finish with a short discussion of the robustness of our results with respect to variations in the network construction parameters.

12.2.1. Bivariate Evaluation

As an introduction to the network part of our evaluation study we take a look at distributions of normalized node-weighted GHDs h^* between the ERAI reference network and model networks of austral summer 2 m temperature time series (Fig. 12.3).

As expected, we find the ERAIb networks to bear the closest resemblance, i.e. the smallest GHD to the reference network, while the random network models are at the other end of the performance spectrum. Among the latter, the ER model yields graphs with the least similarity to the reference graph, as hypothesized in Sec. 10.3. The VL model does not perform much better either although it conserves the reference network's degree sequence. Much smaller GHDs are attained by the SERN model, which tells us that the geographical link length distribution of the reference DJF T2M network contains much information about the network structure. The reason is that links in our climate networks represent the 1% most positive correlation coefficients and thus tend to be short, because those greatest correlations tend to occur between close-by locations. We will come back to this aspect and discuss it in greater detail in Ch. 13. Note that all random network models produce very narrow $h^*(\text{ERAI}, \cdot)$ distributions due to the rather low link density and the high number of nodes (law of large numbers); for a better visualization, the cusps of these distributions were cut off in Fig. 12.3.

Of the RCMs, we find that STARS outperforms CCLM. There are remarkable differences in the shape of the distributions, those of the bootstrap ensembles ERAIb and CCLMb being more than twice as wide as that of the STARS ensemble. This shows that unbiased bootstrapping yields greater variability than biased bootstrapping. As we see in Fig. 12.4, this difference in variability is most pronounced for T2M. The reason is that the STARS resampling algorithm is conditioned by a T2M trend only (cf. Ch. 11), and that the constraints this imposes are passed on to the other variables only inasmuch as these are statistically related to T2M.

12. Bivariate versus Univariate Climate Model Evaluation

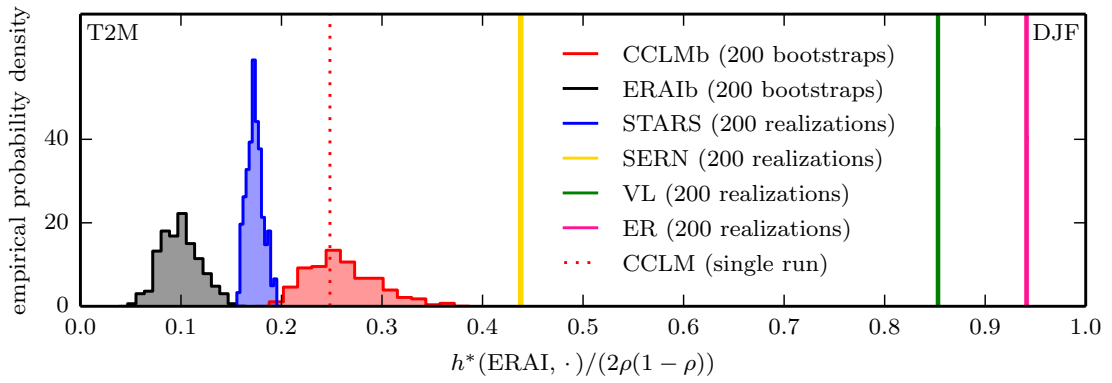


Figure 12.3.: Histograms of normalized node-weighted GHD h^* between the ERAI reference network and model networks of austral summer 2 m temperature time series. The SERN, VL, and ER random network models were set up to reproduce the reference network’s geographical link length distribution, degree sequence, and link density, respectively (cf. Sec. 10.3). Note that h^* has been scaled by the expectation value $\langle h(\text{ERAI}, \text{ER}) \rangle$ of the normalized unweighted GHD between the reference network and an Erdős-Rényi random network with the same link density ρ [Eq. (10.31)].

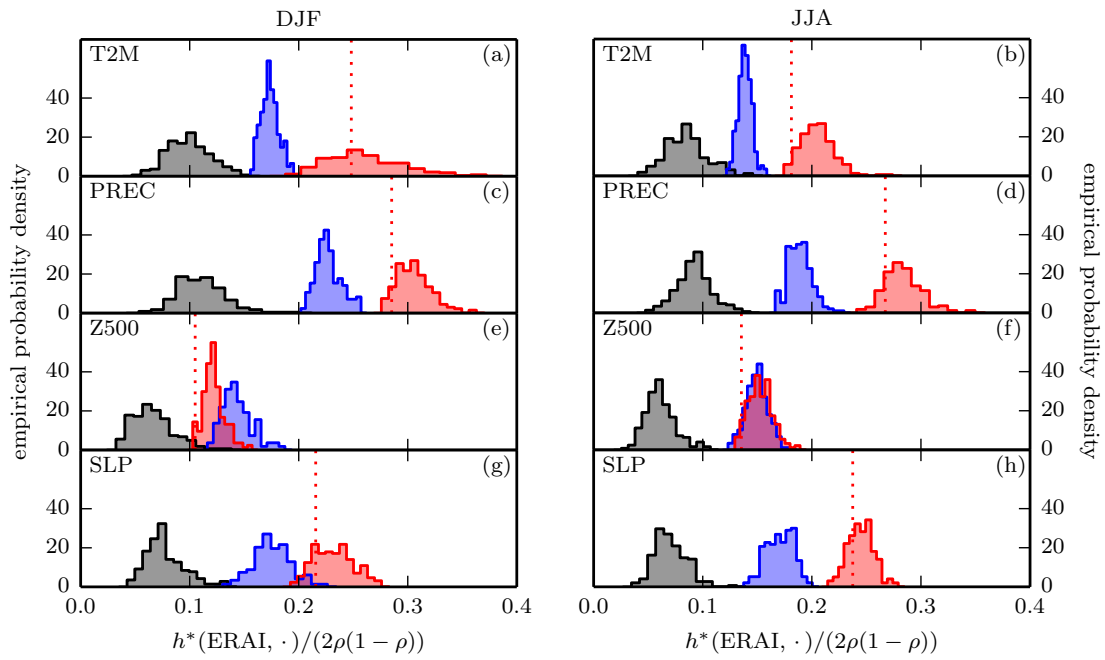


Figure 12.4.: Same as Fig. 12.3 for 2 m temperature, precipitation, 500 hPa geopotential height, and sea level pressure (from top to bottom) in austral summer (left) and winter (right). Note that the random networks were omitted here.

We have left out the GHD distributions of the random networks in Fig. 12.4 because their position hardly differs between variables. For CCLMb, ERAIb, and STARS, we observe that GHDs are greatest for PREC and least for Z500 across data sets and seasons. This indicates that, out of those variables considered in this study, the dynamics of precipitation are hardest and those of the 500 hPa geopotential are easiest to model.

Comparing the ensemble average GHDs across models, we find that STARS has a rather constant relative distance to ERAIb, which simply reflects the functional principle of the statistical model (cf. Ch. 11). In contrast, the performance of CCLM varies strongly between variables. Compared to STARS, it generates T2M, PREC, and SLP networks that are less similar, and a Z500 network that is more similar to the respective reanalysis reference. These larger deviations at the surface reflect that model physics have a larger impact there than in the free troposphere, which is mainly governed by large-scale thermo- and hydrodynamics.

Performance differences between seasons are smaller than those between models. In austral winter (JJA), the modeling of Z500 by CCLM is slightly less accurate than in summer (still only 8% of the STARS realizations perform better than the single CCLM run). This might be attributed to a higher complexity of the extratropical cyclogenesis during winter (Mendes et al., 2010) and its relatively greater influence on the South American climate due to the JJA northward displacement of general circulation patterns.

12.2.2. Bivariate versus Univariate Evaluation

In Fig. 12.5 we compare RCM performance rankings according to h^* versus according to e^* or l^* . We find only agreement in rankings for T2M and PREC, with STARS performing better than CCLM. Yet there is disagreement for the pressure variables in DJF, most visibly in panel (i) for Z500, where h^* and e^* yield different rankings, and in panel (n) for SLP, where h^* and l^* disagree.

We also note a consistent difference in model rankings according to e^* versus according to l^* . While the mean-based RMSE favors STARS in all cases but panel (k), the variance-based RMSLE favors STARS for T2M and PREC, i.e. in half of all cases only. This demonstrates that statistical resampling is unbeatable at retaining mean values, but that dynamical downscaling can catch up at retaining variabilities. With respect to retaining spatial covariabilities, this study clearly sees STARS in front again.

12.2.3. Sensitivity to Network Construction Parameters

So far, we have only presented results for one set of network construction parameters, namely $l = 7$ days for the length of the moving average and $\rho = 0.01$ for the link density of all simple graphs. However, calculations were carried out for a wider range of these parameters. We found that varying $l \in [3, 11]$ and $\rho \in [0.005, 0.02]$ did not alter the results qualitatively.

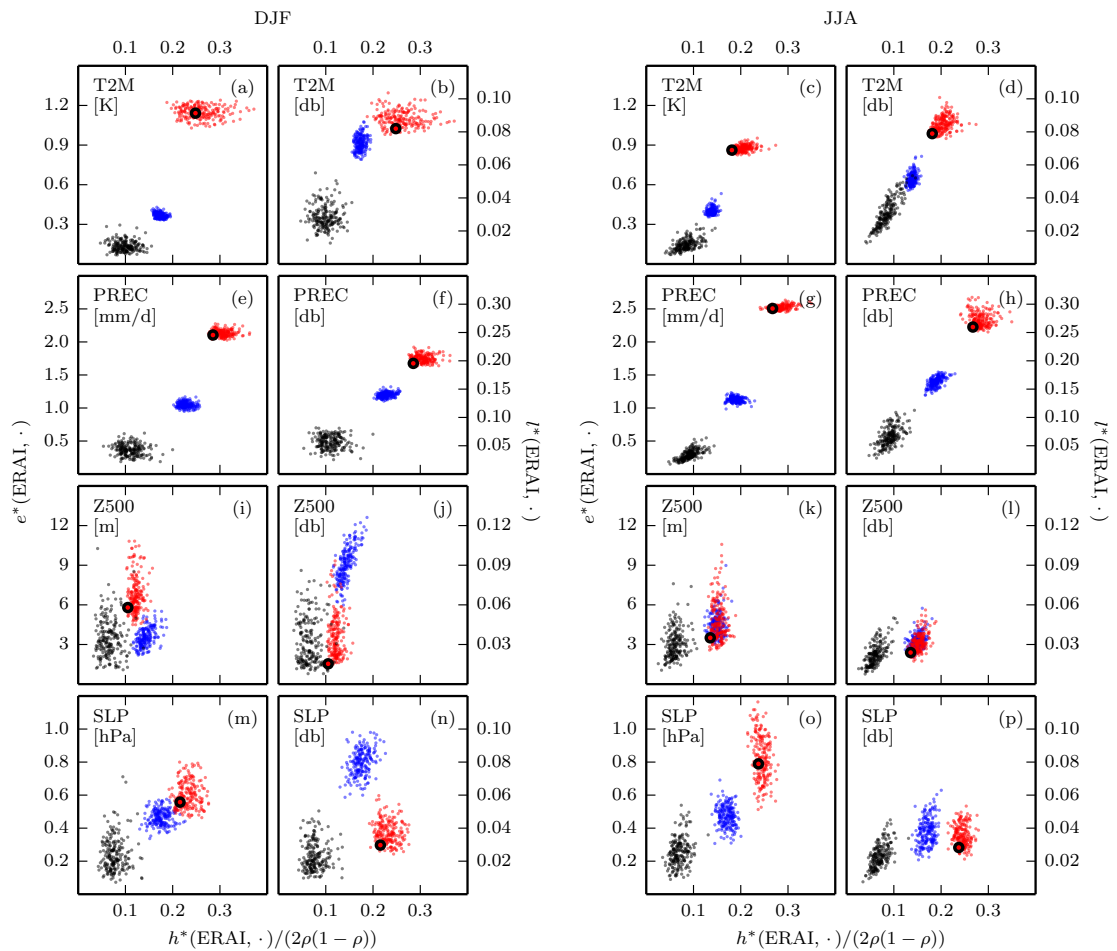


Figure 12.5.: Mean-based RMSE e^* and variance-based RMSLE l^* versus covariance-based GHD h^* for 2 m temperature, precipitation, 500 hPa geopotential height, and sea level pressure (from top to bottom) in austral summer (left) and winter (right). Coloring as in Fig. 12.4; the single CCLM run is depicted by an accentuated red dot. The units of e^* and l^* are specified inside the subplots.

13. Precipitation Climate Networks of the South American Monsoon System

The evaluation study presented in the previous chapter saw STARS outperform CCLM in terms of the value retained by statistical versus dynamical downscaling over South America—an outcome that confirms the results of earlier similar model evaluation studies (Orlowsky et al., 2008, 2010; Lutz et al., 2013). Now one might argue that a comparison of simulation data against the driving reanalysis data does not constitute a proper model evaluation, but that the latter would require a comparison against independent observational data.

This point is well taken since reanalysis data are a blend of historical weather observations with a NWP model simulation (cf. Ch. 2). As pointed out by Kalnay et al. (1996), different reanalysis output variables are subject to different relative influences of the observations and the model. According to these relative influences, the authors classify the output variables of the NCEP/NCAR 40-year reanalysis. For the variables considered in the previous chapter, this classification also applies to the ERAI reanalysis. It sees the 500 hPa geopotential height among the variables that are most strongly influenced by observational data and that are therefore most reliable; the 2 m temperature and the sea level pressure are considered intermediately reliable because, although they are affected by observed data, they are also strongly influenced by the model; and precipitation is in the class of the least reliable variables since there are no precipitation observations included in the ERAI data assimilation.

Therefore, in the following, we use the network approach to *reevaluate* our STARS and CCLM simulations over South America with regard to precipitation—this time against a reference network built from *independent* observational data. Also, to add spatial detail to the evaluation, we deploy our newly developed local network dissimilarity measures LCD, LHD, and DND alongside their global counterparts GCD and GHD (cf. Ch. 10).

13.1. Study Design

A graphic representation of the design of our reevaluation study is given in Fig. 13.1. Next to our STARS and CCLM simulations, we include the ERAI reanalysis in this evaluation to enable an assessment of the value added by statistical and dynamical downscaling. Moreover, we again include random networks and networks based on bootstrapped space-time series, both for the same reasons as in the previous evaluation. This time, however, we only generate random networks with the SERN model, because it clearly outperformed the VL and ER models in the previous evaluation, and can thus be considered the best representative of a worst-case model performance.

13.1.1. Precipitation Reference Data

We employ daily precipitation estimates from the TRMM 3B42 V7 satellite product as our reference observational data (cf. Ch. 6). The reevaluation starts in 1998 since the TRMM data are only available from that year onwards. We also need to shorten the latitudinal extent of the evaluation domain

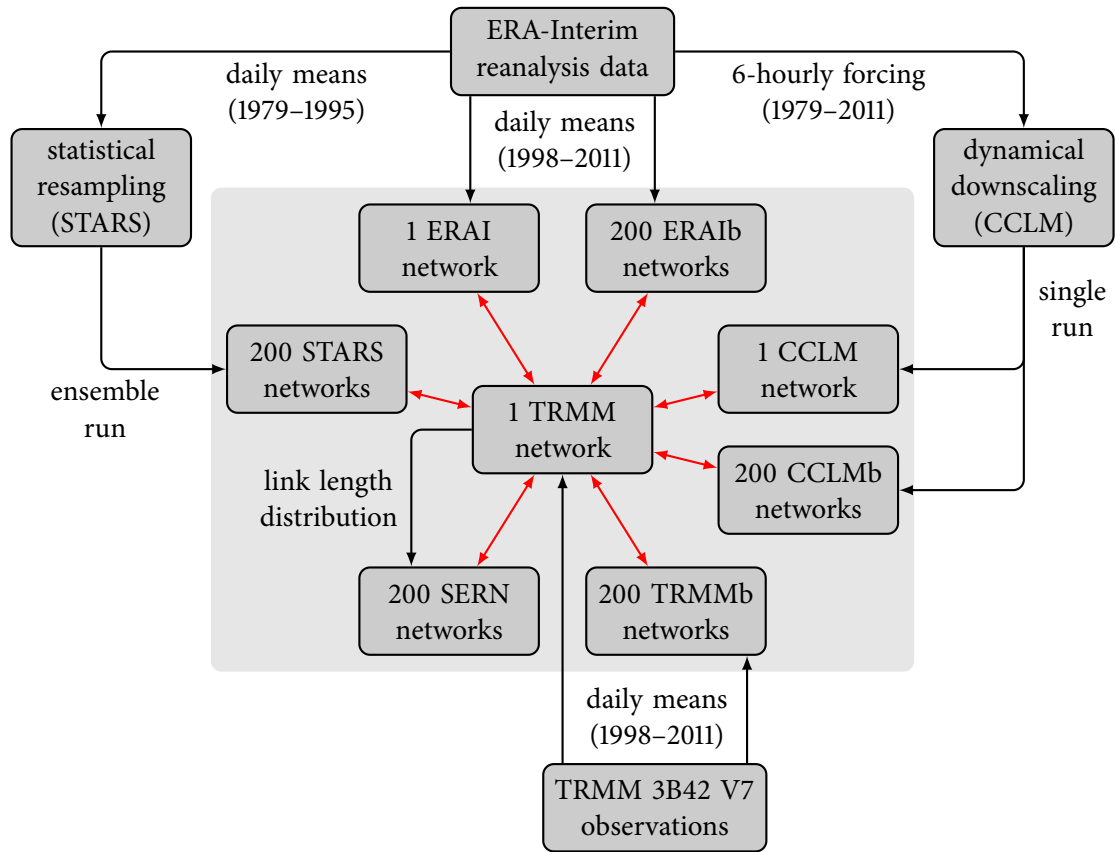


Figure 13.1.: Schematic diagram of our model reevaluation study in which regional climate simulations with CCLM and STARS are driven by ERAI reanalysis data and evaluated against TRMM observations. ERAI data are included in the evaluation to enable an assessment of the value added by statistical and dynamical downscaling. Monsoon season climate networks are constructed from daily precipitation space-time series after all observed and simulated data have been interpolated to the ERAI grid. Networks from bootstrapped space-time series enable a fairer model intercomparison (in the cases of CCLM and ERAI), or represent an optimum model performance (in the case of TRMM), and are denoted by the suffix b. Random networks generated with the SERN model represent a pessimum model performance. The red double-headed arrows indicate network comparisons with our local and global network dissimilarity measures.

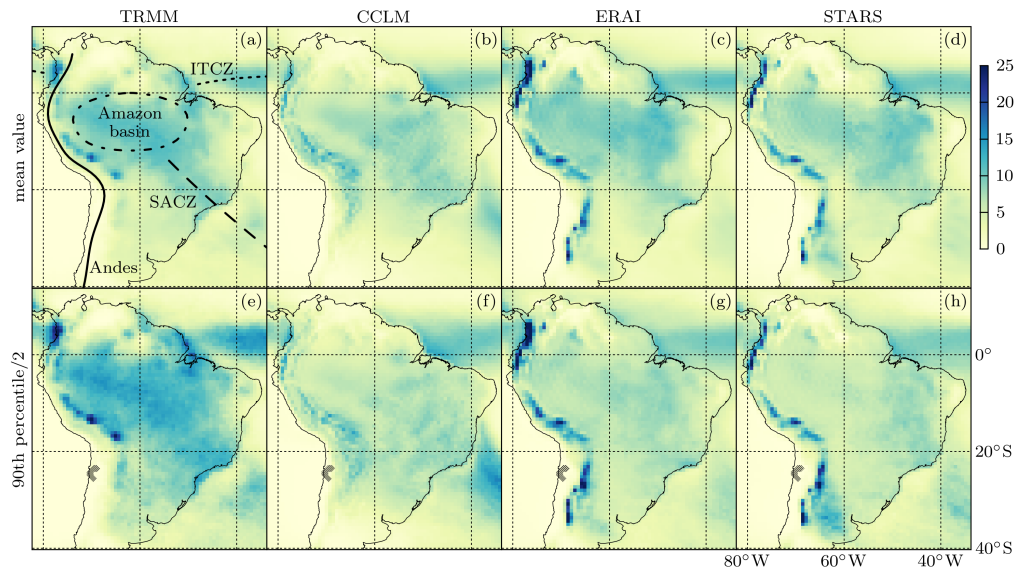


Figure 13.2.: DJF 1998–2011 mean values (top) and 90th percentiles (bottom) of daily precipitation amounts in mm/day as measured by TRMM and modeled by CCLM, ERAI, and STARS (from left to right). Note that the 90th percentiles have been divided by 2 to fit into the same scale as the mean values. Grid cells with 90th percentiles equal to zero in any of the observed or simulated data sets are hatched in (e–h). The locations of the Andes (solid), the Amazon basin (dash-dotted), the ITCZ (dotted) and the SACZ (dashed) are sketched in (a).

because the reliable TRMM data only extend to 36°S (cf. Fig. 12.1). To facilitate a proper network comparison, the TRMM data are conservatively interpolated from their native 0.25° grid to the 0.7° ERAI grid.

We concentrate our analysis on the austral summer season DJF, when a monsoon system develops over tropical South America and provides for most of the annual precipitation (Zhou and Lau, 1998; Vera et al., 2006b; Marengo et al., 2012b). Our reevaluation domain is depicted in Fig. 13.2, where we show the DJF mean values and 90th percentiles of daily precipitation amounts as measured by TRMM and modeled by CCLM, ERAI, and STARS from 1998 through 2011. The TRMM data exhibit the typical pattern of abundant rainfall in the Intertropical and the South Atlantic Convergence Zone (ITCZ and SACZ, respectively), and along the eastern slopes of the Andes.

These main rainfall patterns are reproduced by the models but we find substantial differences in intensities. Regarding the seasonal mean values, CCLM mostly underestimates rainfall, while ERAI and STARS are closer to TRMM except along the Andes, where we find strong overestimations. The 90th percentiles, which quantify the intensity of extreme rain events, are mostly and substantially underestimated by all models. While TRMM shows values greater than twice the respective mean values throughout the study domain, the models simulate a smaller ratio at most locations. Such intensity underestimations of extreme rainfall events are shared by many climate models (Dai, 2006).

13.1.2. Network Construction

Precipitation climate networks are built from DJF 1998–2011 daily precipitation space-time series. Since we discard the incomplete seasons January–February 1998 and December 2011 from our anal-

13. Precipitation Climate Networks of the South American Monsoon System

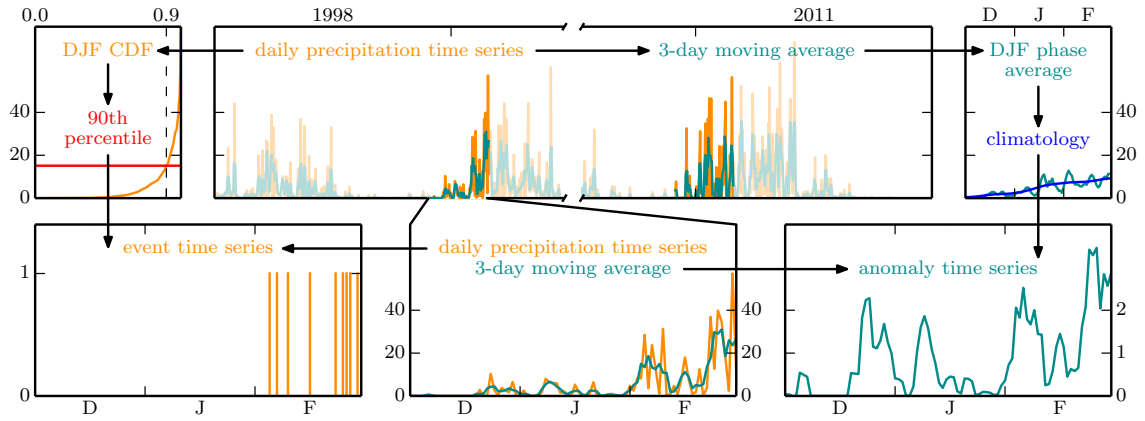


Figure 13.3.: Schematic of local precipitation time series preprocessing to extreme event and anomaly time series. We start with daily precipitation values from the austral summer seasons DJF of 1998 through 2011 (dark orange, top middle) and their 3-day moving averages (dark cyan, top middle). The 90th percentile of all of those daily values (red, top left) is the threshold used to define extreme events (bottom left). The phase-averaged 3-day moving averages, further smoothed by a 7-day Gaussian filter (blue, top right) serve as a climatological DJF time series, to which we scale the 3-day moving averages of each individual season to obtain anomalies (bottom right).

ysis, this implies time series lengths of $M = 1170$ days. Our domain/network comprises $N = 5460$ grid cells/nodes. We focus on networks without node weights to enable an application of the DND. This is reasonable since LHD and GHD results do not change qualitatively when node weights representing grid cell sizes are introduced, which is because grid cells do not vary much in size within the domain. To capture different aspects of precipitation dynamics, we employ two statistical relationship measures for network construction—the Event Synchronization (ES; Quiroga et al., 2002) and the Spearman Rank correlation coefficient (SR; Spearman, 1904).

The ES may be used to analyze the spatial synchronicity structure of extreme precipitation events (Malik et al., 2012), which has been done over South America based on the TRMM 3B41 V7 data by Boers et al. (2013). We adopt the network construction method described in the latter study. It is based on a transformation of precipitation time series to binary extreme event time series as depicted in the left half of Fig. 13.3. At each location, daily precipitation above the 90th percentile of its climatological (DJF 1998–2011) distribution is defined as an extreme event. Grid cells at which the 90th percentile is zero in any of the observed or simulated data sets [hatched in Fig. 13.2(e–h)] are discarded from the analysis. Between two extreme event time series at different locations, the ES then quantifies the degree of event synchronization, with two events contributing to ES if they can be uniquely associated within a maximum period of 3 days. Since no variance-stabilizing transformation is known for ES, we confine the ES network evaluation to the respective simple graph whose links represent the $\rho = 2\%$ highest ES values and which we denote by ES_p.

Besides focusing on extremes, we also aim at evaluating the general spatiotemporal precipitation dynamics. To that end we employ the SR network construction method described in Sec. 12.1.2, which requires preprocessing of the original precipitation values to anomalies with respect to the 1998–2011 climatology (cf. right half of Fig. 13.3). Deviating from the previous evaluation, we apply a 3-day instead of a 7-day moving average filter here to make the SR and ES networks represent

precipitation dynamics at approximately the same time scale. From the matrix of rank correlation coefficients we derive three networks. The matrix as it stands defines an edge-weighted network, which we denote by SR. Simple graphs representing the 2% most positive and the 2% most negative SR values are defined to disentangle these two different kinds of correlation, and are denoted by SRp and SRn, respectively.

Altogether, our networks are constructed following the recipe (10.1), where in the present case, $x_i(t)$ are the local daily precipitation time series, P represents their preprocessing to anomaly or extreme event time series $y_i(t)$ (cf. Fig. 13.3), $S = SR$, ES marks the application of a statistical dependence measure to all pairs of time series which results in a matrix (r_{ij}) of correlation or synchronization strengths, and T denotes the thresholding that yields the simple graph adjacency matrices (a_{ij}) according to

$$a_{ij} = \begin{cases} \Theta[\tau(\rho) - r_{ij}] & \text{for SRn,} \\ \Theta[r_{ij} - \tau(\rho)] - \delta_{ij} & \text{for SRp, ES,} \end{cases} \quad (13.1)$$

with the Heaviside function Θ , the Kronecker delta δ_{ij} , and the threshold τ set such as to obtain the desired link density ρ .

It should be noted that the modeling accuracy of these networks is, in principle, independent of general rain amount biases. Two pairs of time series can have the same correlations even if standard deviations or means of the time series differ. Similarly, two pairs of (extreme) event time series can agree in synchronicity despite disagreement in the event-defining threshold. Therefore, the discrepancies between observed and modeled precipitation mean values and 90th percentiles we see in Fig. 13.2 do not preclude agreement in the SR or ES network structures.

13.2. Results

Before we study dissimilarities between modeled and observed precipitation networks, we analyze the topologies of the different network types, so as to simplify the subsequent interpretation of network dissimilarities.

13.2.1. Network Topologies

We first want to take a look at the degree fields of our simple graphs. For the SR network, we define a quantity similar to the degree by the mean Fisher transformed rank correlation,

$$f_i = \frac{1}{N-1} \sum_{j \neq i} F(r_{ij}). \quad (13.2)$$

The f_i and k_i fields of the different networks based on TRMM, CCLM, ERAI, and STARS data are shown in Fig. 13.4. The f_i fields are mostly positive, which shows that positive correlations between anomaly time series predominate. The few locations of negative f_i differ in position between data sets. Spatial contrasts between f_i values are least pronounced for TRMM and most for CCLM.

Although SRn and SRp links encode fundamentally different statistical relationships, the degree fields of the respective networks roughly agree in exhibiting and locating three distinct regions of enhanced degree indicated by colored boxes in Fig. 13.4(i). All models reproduce this general pattern. As to the climatological interpretation of the SRp network, we notice that the regions of large degree are adjacent to the zones of most abundant seasonal rainfall (cf. Fig. 13.2), while over those

13. Precipitation Climate Networks of the South American Monsoon System

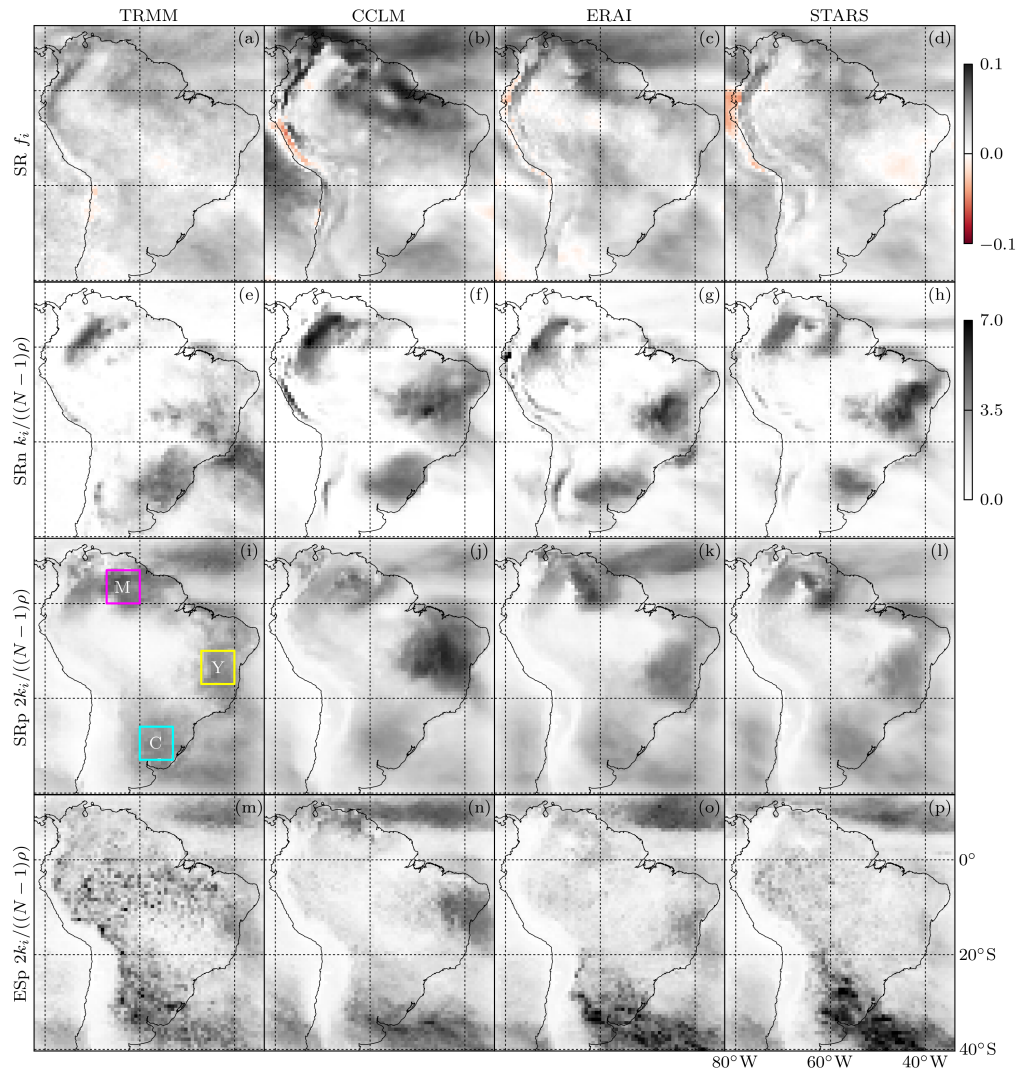


Figure 13.4.: Mean Fisher transformed SRs [top, Eq. (13.2)] and degrees [Eq. (10.2)] of SRn, SRp, and ESsp simple graphs (from top to bottom) from rainfall data measured by TRMM and modeled by CCLM, ERAI, and STARS (from left to right). Degrees are shaded according to the lower color scale and have been rescaled to their average $(N - 1)\rho$. Note further that the ESsp and SRp degrees have been multiplied by 2 to fit them into one scale with the SRn degrees. The three colored $7^\circ \times 7^\circ$ boxes in (i) define the regions referred to later in the text and in Fig. 13.6.

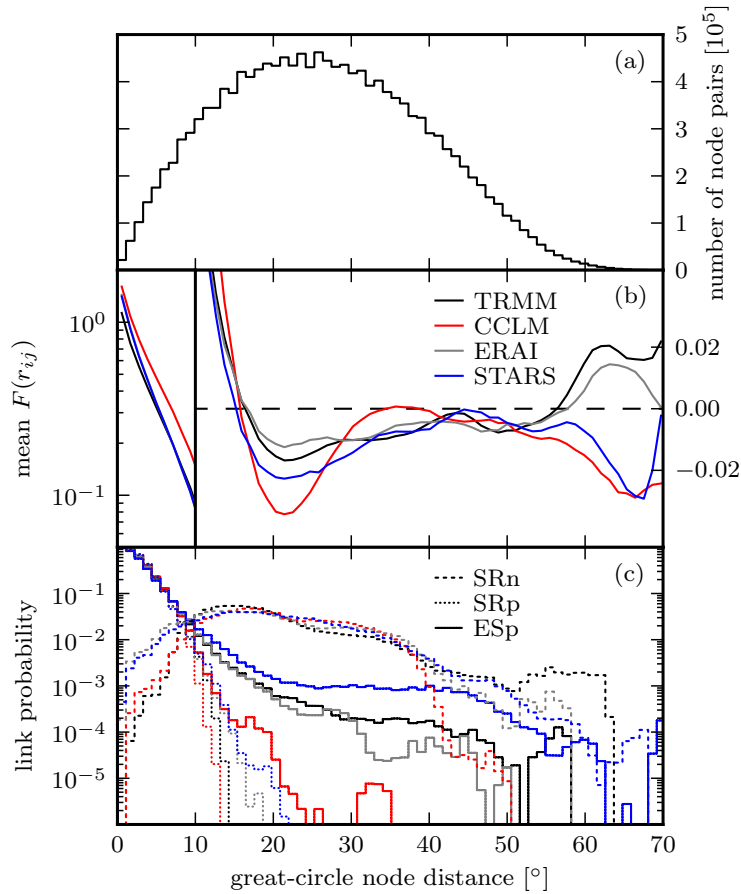


Figure 13.5.: Dependence of rank correlations (b) and simple graph link probabilities (c) on geographical node distance for TRMM, CCLM, ERAI, and STARS networks, based on binned node distances and their absolute number distribution (a). The link probabilities in (c) are the conditional probabilities of finding two nodes linked given their distance. A great-circle distance of 10° corresponds to a geographical distance of approximately 1113 km.

zones themselves (Amazon basin, ITCZ, SACZ), degrees are low, just like over the very dry southern hemispherical Pacific coast. This is explained as follows. Precipitation time series in very dry regions are mostly constant and can therefore not be correlated to other more rainy, less constant time series; the abundant rainfall in the convergence zones is associated with frequent localized convective rain events (Vera et al., 2006b), hence the low correlation levels there; and in the intermediately wet regions adjacent to the convergence zones, wet and dry periods alternate, which causes large intraregional correlations there. Below, we show that the SR_p network links are indeed purely intraregional, and we give a climatological interpretation of the SR_n network. For a detailed climatological interpretation of the ES_p network we refer the reader to Boers et al. (2013).

We proceed by analyzing the dependence of mean correlations and simple graph link probabilities on the geographical distance of nodes (Fig. 13.5). While it is known that correlations between precipitation time series decay with distance (Huff and Shipp, 1969) and a similar behavior has been found for synchronizations of extreme precipitation events (Malik et al., 2012), details of the

SR and ES decays have not yet been compared and we do not know at which distance to expect the anticorrelations represented by the SRn network.

Figure 13.5(b) shows an approximately exponential decay of $F(r_{ij})$ values with node distance for short distances, followed by predominating anticorrelations for intermediate great-circle distances between about 15° and 55° . The distribution of $F(r_{ij})$ values becomes bimodal at distances beyond 60° , with positive and negative modes representing correlations and anticorrelations between anomaly time series in the diagonally opposite corners of the domain; deviations of mean $F(r_{ij})$ values from zero at those distances are therefore not statistically significant. While all models reproduce these characteristics, STARS and particularly CCLM overestimate the absolute values of both the most positive and the most negative correlations; ERAI follows the TRMM observations more closely. We find corresponding deviations in the rank correlation thresholds defining the SR simple graphs: The 2nd and 98th percentiles of SR are -0.16/-0.24/-0.18/-0.23 and 0.43/0.58/0.48/0.47 for TRMM/CCLM/ERAI/STARS, respectively.

For the three simple graphs, the link probability as a function of geographical node distance is shown in Fig. 13.5(c); the related absolute number distribution of node distances is depicted in Fig. 13.5(a). Most of the 2% strongest anticorrelations turn out to connect anomaly time series 10° to 40° away from each other. SRp and ESsp link probabilities decay differently for distances beyond about 10° . In line with $F(r_{ij})$ values, SRp link probabilities go to zero at about 15° , while some nodes much farther apart are linked in the ESsp graph. Distinctly positive rainfall anomaly correlations are hence confined to be short ranged, while some of the 2% strongest extreme rainfall event synchronizations over South America are found between locations thousands of kilometers apart. Across graph types, CCLM produces too many short- and too few long-range links, which means that the model underestimates the strength of teleconnections relative to local anomaly correlations and event synchronizations. ERAI and STARS show less coherent deviations from TRMM with the reanalysis following the observations most closely, overall.

To shed some more light on the network topologies, Fig. 13.6 depicts RGB color coded connectivities to the three regions C, M, Y defined by colored boxes in Fig. 13.4(i). In the TRMM SRn graph, we find nodes south of Y connected to C and nodes in and northeast of C connected to Y. Moreover, we find nodes north of Y connected to M and nodes west of M connected to Y. Rainfall dipole patterns underlying these regional connectivities have been studied in the climatological literature. The M-Y anticorrelation has been associated with active and break phases in the South American monsoon system (Jones and Carvalho, 2002). The C-Y one corresponds to the well-studied SACZ seesaw pattern, which is caused by middle-latitude frontal systems propagating into the tropics (Nogués-Paegle and Mo, 1997; Carvalho et al., 2004). In contrast to SRn, the SRp and ESsp graphs are dominated by short-range links and no interregional connections are found. The models reproduce the general patterns of connectivity to the regions C, M, Y for every graph type, yet with reduced accuracy for SRn compared to SRp and ESsp. In particular, anticorrelations between C and the maritime SACZ are underestimated by every model (cf. Fig. 13.4), and CCLM overestimates the strength of the M-Y anticorrelation.

13.2.2. Global Network Dissimilarities

Global correlation and Hamming distances of modeled to TRMM precipitation networks for the four different network types are depicted in Fig. 13.7. For each of the three simple graph types, the SERN model (cf. Sec. 10.3) was used to generate an ensemble of 200 random networks with the same distribution of geographical link lengths as the respective reference TRMM graph. We have seen that the climate models basically reproduce those distributions with their network-type dependent

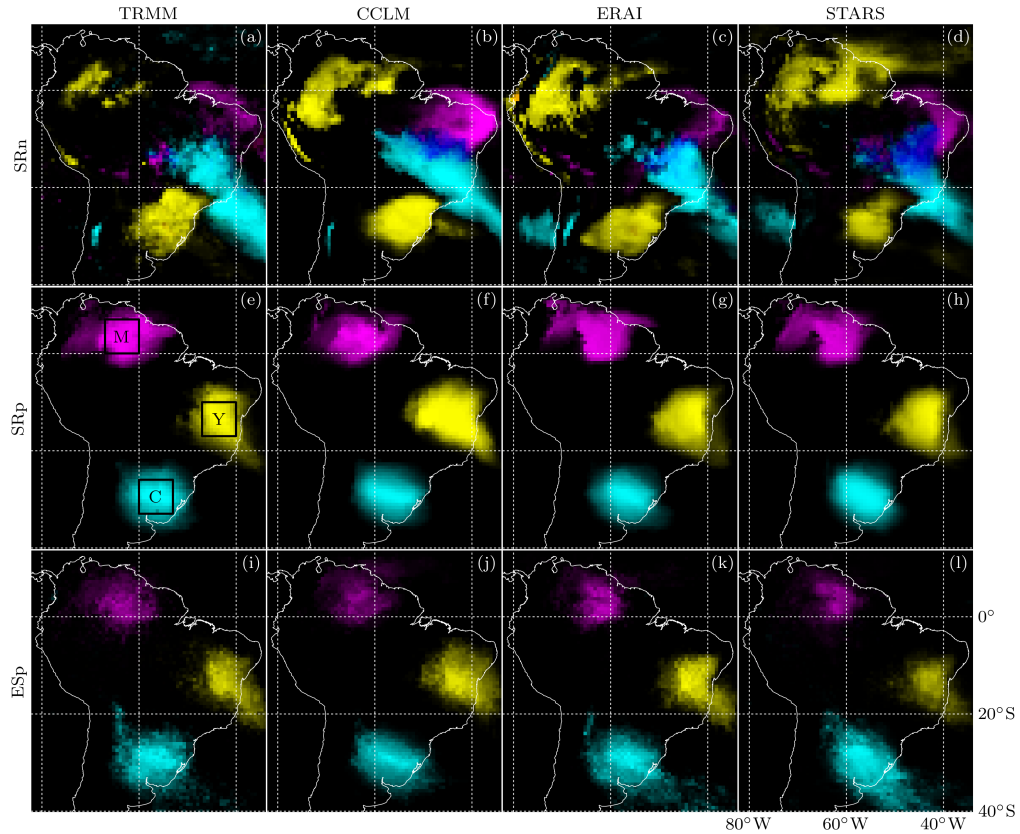


Figure 13.6.: Connectivities to the regions marked by colored boxes in Fig. 13.4(i) for the TRMM, CCLM, ERAI, and STARS (from left to right) SRn, SRp, and ESp (from top to bottom) graphs. For each node i , the connectivity to the three regions [marked again by black boxes in (e)] is transformed to an RGB color with additive color mixing. We use cyan, magenta, and yellow for links to C, M, and Y, respectively, with color intensities proportional to the number of links between i and the respective region. In formulas, if i is connected to n_C , n_M , and n_Y nodes in boxes C, M, and Y, respectively, we calculate a 24-bit RGB color code of $(255 n_C/100, 255 n_M/100, 255 n_Y/100)$ as all boxes contain exactly 100 nodes, and apply an additional hue shift by 180° (Agoston, 2005). Note that, since the hypothetical case of a node connected to all C, M, and Y nodes does not occur, white has a purely decorative meaning.

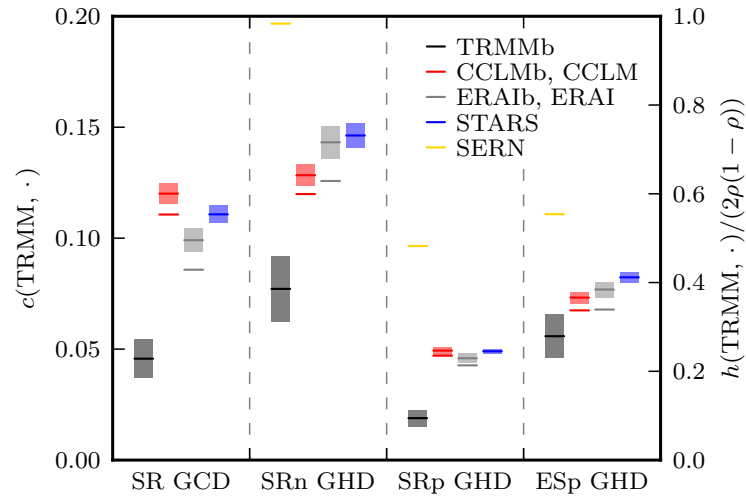


Figure 13.7.: Global correlation and Hamming distances of modeled to TRMM precipitation networks for the four different network types SR, SRn, SRp, ESp (from left to right). The left and right scales apply to the GCDs and GHDs, respectively. The latter have been renormalized by the expectation value of the GHD to an Erdős-Rényi random network with the same link density [Eq. (10.31)]. For ensemble networks (TRMMb, CCLMb, ERAIb, STARS, SERN, 200 realizations each), the range of ± 1 standard deviation around the ensemble mean is shaded. Lines without uncertainty shading represent single realization networks (CCLM, ERAI). The uncertainties of $h(\text{TRMM}, \cdot)$ are invisibly small.

character [cf. Fig. 13.5(c)]. The SERN model performances quantify what could be expected from a correct such reproduction alone; the smaller the GHD between SERNs and the respective TRMM network, the more topological information on the latter is contained in its link length distribution.

Figure 13.7 reveals that performance differences between CCLM and CCLMb or ERAI and ERAIb are minor, which shows that CCLM and ERAI global network dissimilarities to TRMM mainly reflect model deficiencies. Nevertheless, from here on we will compare STARS network errors to those of CCLMb and ERAIb only and thereby facilitate a fairer model intercomparison.

From the bootstrap network ensemble spread of GCDs and GHDs we can also learn something about the interannual variability present in each data set. Irrespective of their type, networks from bootstrapped observational data feature spreads about twice as large as those from bootstrapped reanalysis data and even less variability is present in the CCLMb and STARS ensemble data. The SRp graph exhibits the smallest interannual variability of all simple graphs—a persistence that is arguably due to the predominance of short-range links in this network (cf. Radebach et al., 2013).

Coming back to the SERN model, we observe that its performance varies considerably between graph types. These variations are associated with differences between the respective geographical link length distributions [cf. Fig. 13.5(c)]. In the case of the SRp graph, the distribution is highly informative about the network topology. It allows to infer that only short-range links exist in the network and that geographical neighbors are most likely also topological neighbors. Aside from the existence of several long-range links, this also holds true for the ESp graph, hence the superiority of the SERN model over the ER model for these two graph types. Analogously, the contrastingly poor SERN model performance for the SRn graph is due to the flatness of the respective link length distribution.

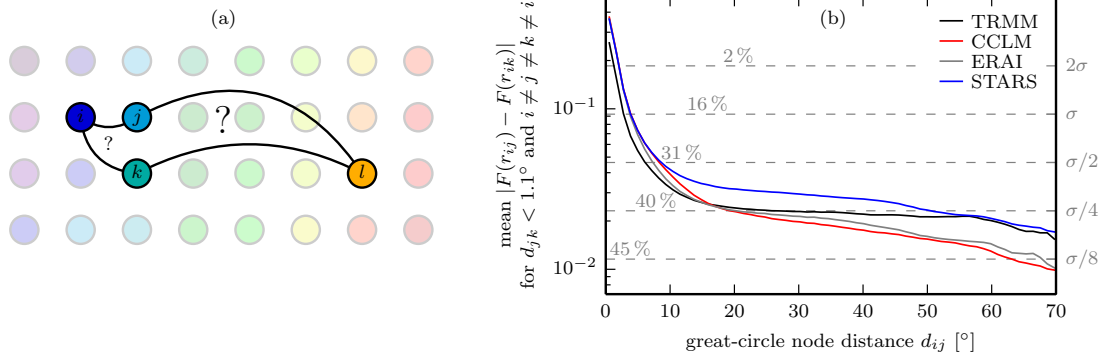


Figure 13.8.: Why in our networks long-range links are statistically more susceptible to misplacement than short-range links. (a) Schematic of a simple graph where the color of a node represents the time series behind it with similarity between colors corresponding to similarity between time series. Note that just like our precipitation climate networks, this schematic graph features roughly constant nearest geographical neighbor distances and decreasing node similarity with increasing geographical node distance. (b) Mean absolute differences between Fisher transformed correlation coefficients r_{ij}, r_{ik} for geographically close nodes j, k versus d_{ij} , the geographical distance between nodes i, j . Since the estimation errors of the Fisher transformed rank correlations are value-independent (Fieller et al., 1957; Fieller and Pearson, 1961), plot (b) shows that with increasing d_{ij} , correlation differences $r_{ij} - r_{ik}$ for geographically close nodes j, k become less robust with respect to the estimation errors of r_{ij}, r_{ik} . As $r_{ij} - r_{ik}$ becomes less robust, so does the relative ranking of r_{ij}, r_{ik} and, hence, the thresholding of r_{ij}, r_{ik} to a_{ij}, a_{ik} [Eq. (13.1)]. Therefore, in the SRn and SRp graphs, the misplacement of a long-range link [j - l versus k - l in (a)] is more likely than the misplacement of a short-range link [i - j versus i - k in (a)]. To give an idea of link misplacement likelihoods, probabilities of false relative rankings of r_{ij}, r_{ik} at different σ levels are marked in (b). The σ levels were calculated using a BART estimator for the effective sample size $M' < M$ to account for autocorrelations in the anomaly time series (Thiébaux and Zwiers, 1984).

Conspicuously, SERN and climate model performances vary quite similarly between graph types. Since SERNs and climate model networks have nothing in common but their link length distribution [cf. Fig. 13.5(c)], the similarity must have something to do with the latter. Yet the explanation of the performance differences between graph types cannot be the same for the random network model and the climate models since CCLM, ERAI, and STARS place links in a manner that is clearly not random (cf. Fig. 13.6). We think that the differences in climate model performances between graph types can be explained by differences in the mean geographical link length between graph types in connection with the conjecture that in our networks long-range links are statistically more susceptible to misplacement than short-range links.

In Fig. 13.8(b) we give a numerical validation of this conjecture for our SR networks; an analogous validation for the ES network is unfeasible at this point as no variance-stabilizing transformation is known for the ES. A heuristic motivation of the conjecture is possible with the help of an analogon from psychology, regarding the network nodes in Fig. 13.8(a) as grown-up humans, for which, owing to the developmental process of perceptual narrowing (Scott et al., 2007), it is easier to discriminate between familiar than between unfamiliar types of perceptual stimuli: Because nodes j and k are

more similar to the close node i than to the distant node l , it is easier for i than for l to distinguish between j and k . Thus, in terms of links, $j-l$ is more likely to be confused with $k-l$ than $i-j$ with $i-k$. The connection between node similarity and link dissimilarity, that is implicit to this analogon, is established via the statistical dependence measures SR and ES and constitutes the core of the conjecture.

In simple terms, the SRn graph is harder to reproduce than the other simple graphs because its links are longer. We propose to account for this purely geometric-statistical effect by relating climate model performances to the respective SERN model performance, which nicely quantifies the effect. And just as $h(\text{TRMM}, \text{SERN})$ represents a worst case performance scenario, the GCDs and GHDs between TRMM and TRMMb networks constitute optimum performance limits for CCLMb, ERAIb, and STARS. In the sense of Murphy (1993), relating climate model performances to these benchmarks yields a more informative measure of the actual climate model skills when comparing performances between different network types. We thus define a model skill score that takes both benchmarks into account by

$$S(A; R, O, P) = \frac{h(R, P) - h(R, A)}{h(R, P) - h(R, O)} \quad (13.3)$$

for model A with reference $R = \text{TRMM}$, optimum $O = \text{TRMMb}$, and pessimum $P = \text{SERN}$. This yields average (over CCLMb, ERAIb, and STARS) model skill scores of 0.480(8)/0.624(4)/0.606(11) for SRn/SRp/ESp, respectively. Like Fig. 13.6, this suggests that the SRn graph is hardest to model, even after taking the link length effect into account. As per Welch's t -test (Welch, 1947), the average SRp and ESp skill scores are not significantly different at the 5% α level. Compared to the untransformed GHDs, the skill scores display considerably increased similarity between network types which means that large parts of the performance differences between network types can be attributed to type-specific network uncertainties due to climate variability and spatial embedding.

A model performance intercomparison for the individual network types is permitted as all differences between ensemble mean GCD or GHD values are significant at the 5% α level according to Welch's t -test. We find that STARS performs worse than ERAI for every network type considered. The best models are ERAI for the edge-weighted SR network and the SRp graph, and CCLM for the SRn and ESp graphs. The poor SR performance of CCLM is in line with its abovementioned overestimation of absolute correlation values [cf. Fig. 13.5(b)].

A comparison of the SRp column of Fig. 13.7 with Fig. 12.4(c) shows that it does make a difference if STARS and CCLM are evaluated against independent observational data or against their driving reanalysis data. In our reevaluation against TRMM, STARS and CCLM perform about equally well ($h(\text{TRMM}, \text{CCLM}) < \langle h(\text{TRMM}, \text{STARS}) \rangle < \langle h(\text{TRMM}, \text{CCLMb}) \rangle$), while in the evaluation against ERAI, STARS clearly outperforms CCLM ($h^*(\text{ERAI}, \text{CCLM}) > \langle h^*(\text{ERAI}, \text{STARS}) \rangle < \langle h^*(\text{ERAI}, \text{CCLMb}) \rangle$).

13.2.3. Local Network Dissimilarities

We now come to the application of the new local network dissimilarity measures. LCDs, LHDs, and DNDs between TRMM and model precipitation networks are depicted in Fig. 13.9. We do not show the LHDs between ESp graphs because they are dominated by the degree dependence which motivated the introduction of the DND, nor the DNDs between SRn graphs since they are undefined in many locations due to a multitude of isolated nodes in these graphs.

Starting with the LCD, we find virtually no spatial variability in $c_i(\text{TRMM}, \text{TRMMb})$, which is

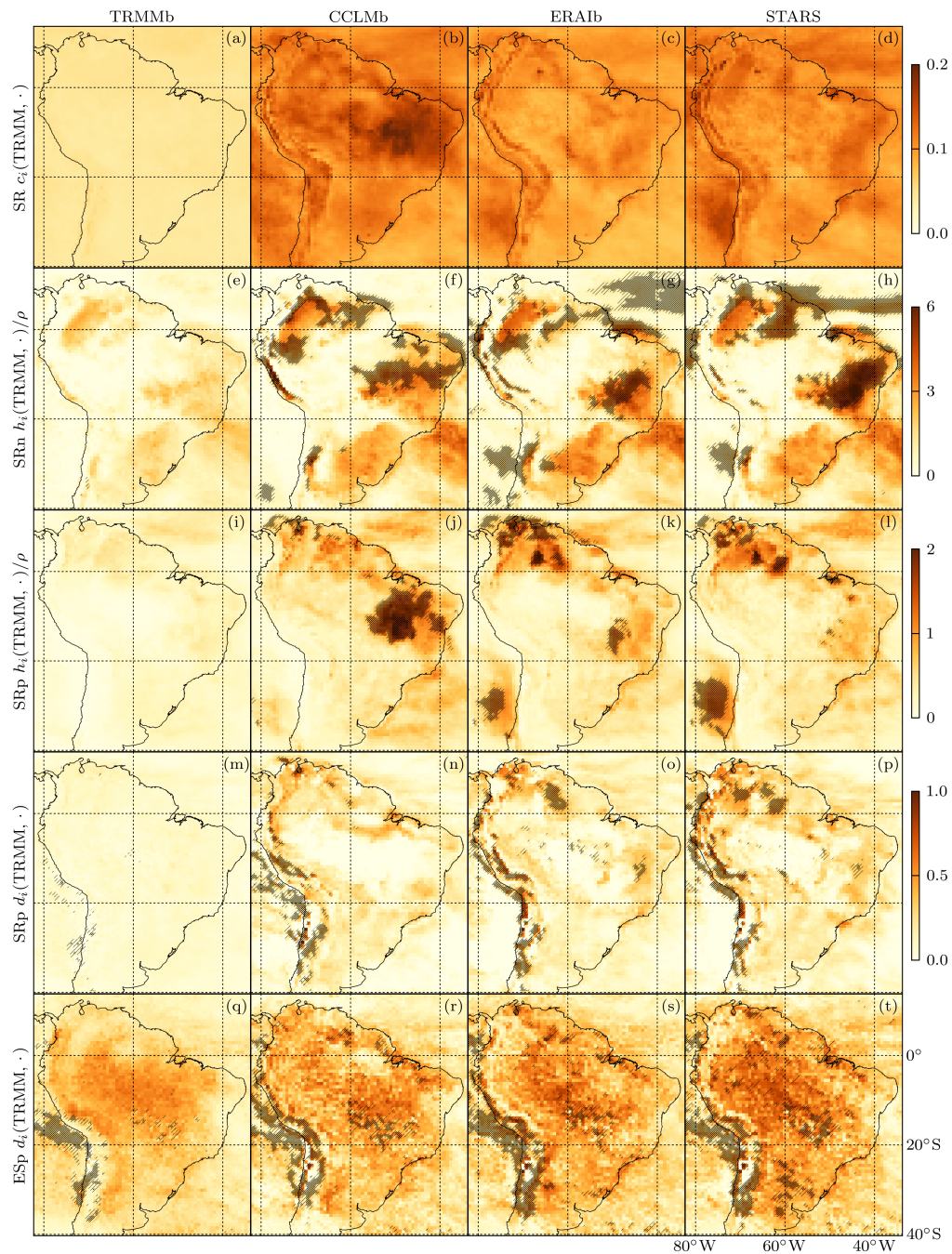


Figure 13.9.: Ensemble mean local differences of TRMMb, CCLMb, ERAIb, and STARS (from left to right) to TRMM precipitation networks. SR (a–d) network LCDs [Eq. (10.13)], SRn (e–h) and SRp (i–l) graph LHDs [Eq. (10.5)], SRp (m–p) and ES p (q–t) graph DNDs [Eq. (10.12)]. Note that the LHDs have been renormalized by $(N - 1)\rho$, analogously to the degrees (Fig. 13.4). The color scale next to (p) is also applicable to (q–t). Hatching in (e–l) puts LHDs in relation to $h_i(\text{TRMM}, \text{SERN})$ of the respective graph type; same for DNDs in (m–t); light hatching indicates insignificantly different values at the 5% α level according to Welch's t -test (Welch, 1947); heavy (no) hatching indicates a significantly better (worse) local performance by the random network model.

due to the use of the Fisher transformation in the LCD definition [Eq. (10.13)] if we consider differences between TRMM and TRMMb correlations to quantify estimation errors. The contrasting spatial dependence of climate model LCDs hints at model deficiencies with spatially inhomogeneous consequences. Higher correlation differences common to all models can be observed along the Andes, in northeastern Brazil and over the Pacific south of 20°S while lower values occur over the Atlantic south of the SACZ. We observe LCD contrasts along the coasts and find a larger LCD spread across models over land than over sea. The largest correlation distances to TRMM are produced by CCLM over central Brazil.

The LHDs of SRn and SRp simple graphs are clearly degree-dependent (cf. Fig. 13.4). We see that high LCDs may coincide with high LHDs as for instance over the Pacific off the Chilean coast for STARS or over central and northeastern Brazil for CCLM. Yet where correlations are not strong enough to be represented by links in the simple graphs, high LCDs may come along with low LHDs as can be observed along the Andes.

Hatching in Fig. 13.9(e–t) visualizes the respective relative local SERN model performances. Light hatching indicates insignificantly different local network dissimilarities at the 5% α level according to Welch's t -test (Welch, 1947) while heavy (no) hatching indicates a significantly better (worse) local performance by the random network model. In line with GHD results (cf. Fig. 13.7), the climate models perform better in most locations. Yet there are areas where mere knowledge of the observed all-domain link length distribution allows for a better neighborhood prediction than the use of a climate model. With the LHD, these areas differ considerably between models.

A more coherent picture only emerges with the DND, shown for SRp and ESsp graphs in Figs. 13.9(m–p) and 13.9(q–t), respectively. We observe larger DNDs over land than over sea and find particularly high values in the Guiana Highlands and along the Andes. DNDs between TRMM and TRMMb are much larger for the ESsp than for the SRp graph. Climatic uncertainties of extreme event synchronizations are most pronounced in the Amazon basin and along the eastern slopes of the Andes, which is consistent with the outstanding noisiness of TRMM's ESsp degree field in those areas [cf. Fig. 13.4(m)]. In line with the respective GHDs (Fig. 13.7), the ESsp DNDs to TRMM increase slightly from TRMMb to CCLMb to ERAIb to STARS while their spatial patterns do not vary much across data sets. This shows that most of the differences between TRMM and climate model ESsp graphs can be explained by interannual climate variability.

In this context, note that, generally, the local network difference fields based on the original CCLM and ERAI time series do not differ much from the respective bootstrap ensemble mean fields. The latter are smoother and feature slightly larger values but apart from that show the same spatial patterns. Hence, where climate model bootstrap network dissimilarities to TRMM clearly exceed the corresponding difference between TRMM and TRMMb, network imperfections cannot be explained by climatic uncertainty but must be due to model deficiencies.

14. Summary and Discussion II

In the second part of this dissertation we introduce new performance metrics for climate model evaluation based on climate networks. These metrics enable the evaluation of climate models with respect to spatial covariabilities and thus offer a bivariate model evaluation perspective. New network dissimilarity measures for the comparison of climate networks constructed from simulated and observed spatiotemporal data constitute the core of our approach. We define both local and global network dissimilarity measures to facilitate the depiction of local dissimilarities in the form of network bias maps as well as the aggregation of those local network dissimilarities to global ones for the purposes of climate model intercomparison and ranking. To cover as wide a range of applications as possible, our measures are defined for directed as well as for undirected climate networks with and without edge weights and/or node weights.

For graphs without edge weights, we adopt the distance function proposed by Hamming (1950) to define the Local and the Global Hamming Distance (LHD and GHD). We demonstrate that the LHD comes with a disadvantageous degree dependence, which we propose to overcome using a suitable statistical null model, relating the actual LHD value to the null model probability distribution of possible LHD values given the degrees of the respective node. This way a second local network dissimilarity measure is defined which we call the Degree-conditional Neighborhood Dissimilarity (DND). The relationship between network LHD and DND is similar to the one between absolute and relative precipitation biases. Large LHDs can coincide with small DNDs and vice versa. The two measures should therefore always be considered conjointly to prevent misinterpretations. Our ansatz to render the LHD degree-independent via a statistical null model goes beyond existing ad hoc normalization methods used by the vertex similarity community to solve the equivalent problem occurring when comparing different nodes of the same network (Leicht et al., 2006). As our ansatz has the virtue of an explicit probabilistic motivation and is easily transferred to the equivalent vertex similarity problem, we propose it to supersede the ad hoc approaches common in that field.

For climate networks with edge weights, we argue that a suitable dissimilarity measure should account for estimation uncertainties inherent to the edge weights, as the latter usually represent the strength of statistical relationships between time series at different locations. For the case of the edge weights being correlation coefficients, we propose to employ the variance-stabilizing Fisher transformation for this purpose and define the Local and the Global Correlation Distance (LCD and GCD). For other measures of statistical relationship, our argument should be seen as an incentive to develop lacking estimation error theories.

We apply our novel network dissimilarity measures to comparatively evaluate regional climate simulations over South America with a statistical and a dynamical regional climate model. In the first of two such studies, simulations are both driven by and evaluated against ERA-Interim (ERA-Interim) reanalysis data. The evaluation is done for the 2 m temperature, precipitation, the 500 hPa geopotential, and sea level pressure in austral summer (DJF) and winter (JJA).

For each variable and season, climate networks are constructed based on spatial correlations between anomaly time series, and compared using the GHD. We find that the statistical model STARS is better at reproducing the network structure of the 2 m temperature, precipitation, and sea level

pressure time series, while the dynamical model CCLM performs better for the 500 hPa geopotential. The least and the greatest network dissimilarities across models and seasons are found for the 500 hPa geopotential and for precipitation, respectively. This indicates that spatial covariabilities of the 500 hPa geopotential are easiest and those of precipitation are hardest to model. The special position of the 500 hPa geopotential comes as no surprise since it is the only upper-level variable, i.e. it is undisturbed by orographic or other surface-based influences, and since its dynamics have been found relatively easy to model before (Steinhaeuser and Tsonis, 2013). The difficulty of precipitation modeling does not astonish us either, given the results of the first part of this dissertation, and considering the outstanding complexity of precipitation dynamics in general (Huff and Shipp, 1969; Matsoukas et al., 2000; Peters et al., 2001). The plausibility of this outcome demonstrates the suitability and reliability of our network approach to climate model evaluation.

In parallel, we quantify model performances with conventional univariate root-mean-square deviations in climatological mean values and variances. When we compare model rankings according to dissimilarities between climate networks versus conventional model error measures, we mostly find agreement, but there are also cases in which the network structure was better reproduced by a model which was less favored by a conventional measure or vice versa, most notably for sea level pressure and the 500 hPa geopotential. Although the construction of climate networks and their comparison takes more effort than applying rather simple univariate model error measures, these complementary findings demonstrate the novelty and justification of our approach.

Since reanalysis precipitation data are not necessarily reliable, in a second application we reevaluate the STARS and CCLM simulations against observational data provided by the Tropical Rainfall Measuring Mission (TRMM) 3B42 V7. We focus on the austral summer season when a monsoon system develops over tropical and subtropical South America. ERAI data are included in the reevaluation to enable an assessment of the value added by statistical and dynamical downscaling. In this study, we deploy all of our newly developed network dissimilarity measures.

Different types of precipitation networks are constructed to capture different aspects of the monsoon system dynamics. Based on spatial rank correlations between anomaly time series, we define an edge-weighted graph called SR and two simple graphs with links representing the 2% most positive and the 2% most negative correlations called SRp and SRn, respectively. Another simple graph called ESp is based on the 2% strongest spatial synchronizations between extreme event time series. We show that the ESp and SRp graphs are dominated by short-range links while teleconnections prevail in the SRn graph. Visualizing these teleconnections using an RGB color model, we reveal that they represent the two major rainfall dipoles of the South American monsoon system. It is shown that these teleconnections are reasonably well reproduced by CCLM and STARS. A distinct shortcoming of CCLM is that, for all graph types, it produces too many short- and too few long-range links, which implies that the model underestimates the strength of teleconnections relative to local anomaly correlations and event synchronizations.

Global distances between TRMM and ERAI/CCLM/STARS simple graphs vary strongly across network types, which allows us to uncover how climate variability and spatial embedding effects impose limits on the fidelity of network reproduction. It is shown that as geographical link lengths increase, so does the likelihood of their misplacement, which explains why GHDs are much larger for the SRn than for the SRp and ESp graphs. We employ Spatially Embedded Random Networks (SERNs) to model this effect. The fraction of network differences due to interannual climate variability is quantified using a bootstrap approach. We find that the ESp graph is most affected by this source of uncertainty, in agreement with the fickle nature of extreme events. Based on SERN and bootstrap network dissimilarities to TRMM, a model skill score is defined that accounts for the mentioned uncertainties. According to this score, the SRp and ESp graphs are reproduced with similar

and higher fidelity than the SRn graph. This result makes sense inasmuch as more than the former graphs, the latter contains nontrivial information about the system dynamics.

Comparing performances between the reanalysis and the RCMs, we find that CCLM performs better than ERAI at two out of four network types, while STARS performs worse than ERAI in all cases. As both CCLM and STARS were driven by ERAI data, this suggests that dynamical down-scaling may retain value at the resolution of the driving data while statistical resampling can only impair data quality. For the SRp graph, our reevaluation against the independent TRMM data yields a relative performance ranking of CCLM versus STARS that is opposite to the one obtained in the first evaluation against the driving reanalysis data.

From the ensemble spread of bootstrap network distances to TRMM we infer that ERAI and even more so CCLM and STARS underestimate the interannual variability of the precipitation dynamics encoded in our networks. As for the reanalysis, this finding complements documented deficiencies in reproducing the variability of spatiotemporal rainfall totals over tropical continents (Bechtold et al., 2008; Nikulin et al., 2012). The loss of large-scale variability in the CCLM simulations might have been prevented by spectral nudging (Castro et al., 2005; Rockel et al., 2008b). In the case of STARS, we conclude that its resampling algorithm tends to reduce the variability present in its input data.

We suspect deficiencies in cloud physics parameterizations of contributing substantially to the variability underestimations by ERAI and CCLM since simulated precipitation characteristics over monsoon season South America have been shown in Pt. I to be highly sensitive to modifications of these parameterizations while the latter are known to lack flexibility in reacting to variations in the large-scale environment (Bechtold et al., 2008, 2014). Another factor are model parameters that in reality vary from year to year but are represented by climatological mean values in ERAI (Loveland et al., 2000; Dee et al., 2011) and CCLM (Smiatek et al., 2008; Doms et al., 2011a), such as aerosol concentrations, forest albedos, and leaf area indices, which means that the models are unable to account for interannual variabilities in aerosol or land-atmosphere feedbacks due to, e.g. volcanic eruptions, bushfires, and droughts.

From our local network dissimilarity measures, the DND proves to be most useful to identify commonalities across data sets. Larger DNDs over land than over sea are consistent with land surface-atmosphere interactions being more complex than sea surface-atmosphere interactions, and relatively high DNDs in the Guiana Highlands and along the Andes confirm model deficiencies in simulating precipitation over complex terrain (Bachner et al., 2008; Ward et al., 2011). Using the DND, we also reveal that for the given observational record length, differences between ES_p graphs are dominated by the interannual variability of extreme events, which impedes a reasonable evaluation of their spatial synchronization at this point.

The situation is different for the correlation networks and we find model-specific spatial patterns in the LHD and LCD fields. The largest SR, SRn, and SRp network dissimilarities of CCLM to TRMM are found over central and northeastern Brazil. We suppose these biases to be associated with an erroneous northward displacement of the SACZ (cf. Pt. I). A common deficiency of ERAI, CCLM, and STARS is an underestimation of the relative strength of the maritime part of the SACZ precipitation seesaw. As both the reanalysis and the dynamical model employ prescribed sea surface temperatures (Pt. I; Dee et al., 2011), this might be due to an imperfect ocean-atmosphere coupling (Braconnot et al., 2007).

In general, the value of the network approach to climate model evaluation stands and falls with the information content of the network considered. By way of example, we have shown that for monsoon season precipitation networks over South America, simple graphs from negative correlations are more interesting than simple graphs from positive correlations. Future efforts towards promot-

ing the approach should thus focus on designing networks that represent pertinent spatiotemporal relationships in climate dynamics. Only when a couple of such networks are found can we expect the climate modeling community to include the network approach in their standard repertoire of model evaluation methods.

Furthermore, it should be investigated whether the novel model performance metrics provide an added value for the assessment of uncertainties of future climate projections. Ideally, the performance of climate models measured by the network metrics in hindcast simulations of some recent climate period would correlate with their accuracy in reproducing observed climate change during the past century.

Beyond climate science, the network approach to model evaluation has the potential to benefit modelers of real-world multidimensional dynamical systems of any background. For instance, it could be used to evaluate models of social dynamics (Erbach-Schoenberg et al., 2014), financial markets (Lux and Marchesi, 1999), neural activity (Zhou et al., 2006; Vértés et al., 2012) or genetic regulatory systems (de Jong, 2002; Ho and Charleston, 2011). The key is to consider multidimensional dynamical systems as networks of dynamically interacting components.

The new network dissimilarity measures by themselves can be employed to compare networks of any functional or structural background as long as these have a common set of nodes. They might be useful additional tools for investigations of network evolution (such as in Spoormaker et al., 2010; Radebach et al., 2013) or for studying the impact of disorders and disasters on network topologies (similar to Greicius et al., 2007; Lynall et al., 2010; Woolley-Meza et al., 2013; Levermann, 2014). Further attention should be paid to the issue of estimation uncertainty for networks that are based on measured or sampled data. Dissimilarities between network structures should be given less weight if they are subject to greater uncertainties. We have provided a solution for the arguably simplest case of networks based on correlation coefficients. More work on this matter needs to be done and is certainly worthwhile, given that uncertainty is ubiquitous where science meets reality.

Bibliography

- Abbe, C. (1901), *The Physical Basis of Long-Range Weather Forecasts*, Monthly Weather Review, 29(12):551–561, doi: 10.1175/1520-0493(1901)29[551c:TPBOLW]2.0.CO;2.
- Agoston, M. K. (2005), *Computer Graphics and Geometric Modelling*, vol. 1, chap. 8, pp. 301–304, Springer London.
- Arakawa, A. (2004), *The Cumulus Parameterization Problem: Past, Present, and Future*, Journal of Climate, 17(13):2493–2525, doi: 10.1175/1520-0442(2004)017<2493:RATCPP>2.0.CO;2.
- Arakawa, A., and W. H. Schubert (1974), *Interaction of a Cumulus Cloud Ensemble with the Large-Scale Environment, Part I*, Journal of the Atmospheric Sciences, 31(3):674–701, doi: 10.1175/1520-0469(1974)031<0674:IOACCE>2.0.CO;2.
- Bachner, S., A. Kapala, and C. Simmer (2008), *Evaluation of daily precipitation characteristics in the CLM and their sensitivity to parameterizations*, Meteorologische Zeitschrift, 17(4):407–419, doi: 10.1127/0941-2948/2008/0300.
- Baede, A. P. M. (2001), *Climate Change 2001: The Scientific Basis. Contribution of Working Group I to the Third Assessment Report of the Intergovernmental Panel on Climate Change*, chap. Appendix I: Glossary, Cambridge University Press, Cambridge, UK and New York, NY, USA.
- Bagnoli, M., and T. Bergstrom (2005), *Log-concave probability and its applications*, Economic Theory, 26(2):445–469, doi: 10.1007/s00199-004-0514-4.
- Baker, I. T., L. Prihodko, A. S. Denning, M. Goulden, S. Miller, and H. R. da Rocha (2008), *Seasonal drought stress in the Amazon: Reconciling models and observations*, Journal of Geophysical Research, 113(G1):G00B01, doi: 10.1029/2007JG000644.
- Baldauf, M., A. Seifert, J. Förstner, D. Majewski, M. Raschendorfer, and T. Reinhardt (2011), *Operational Convective-Scale Numerical Weather Prediction with the COSMO Model: Description and Sensitivities*, Monthly Weather Review, 139(12):3887–3905, doi: 10.1175/MWR-D-10-05013.1.
- Ban, N., J. Schmidli, and C. Schär (2014), *Evaluation of the convection-resolving regional climate modeling approach in decade-long simulations*, Journal of Geophysical Research: Atmospheres, 119(13):7889–7907, doi: 10.1002/2014JD021478.
- Barnett, L., E. Di Paolo, and S. Bullock (2007), *Spatially embedded random networks*, Physical Review E, 76:056115, doi: 10.1103/PhysRevE.76.056115.
- Barreiro, M., A. C. Marti, and C. Masoller (2011), *Inferring long memory processes in the climate network via ordinal pattern analysis*, Chaos: An Interdisciplinary Journal of Nonlinear Science, 21(1), 013101, doi: 10.1063/1.3545273.

- Bechtold, P., J.-P. Chaboureaud, A. Beljaars, A. K. Betts, M. Köhler, M. Miller, and J.-L. Redelsperger (2004), *The simulation of the diurnal cycle of convective precipitation over land in a global model*, Quarterly Journal of the Royal Meteorological Society, 130(604):3119–3137, doi: 10.1256/qj.03.103.
- Bechtold, P., M. Köhler, T. Jung, F. Doblas-Reyes, M. Leutbecher, M. J. Rodwell, F. Vitart, and G. Balsamo (2008), *Advances in simulating atmospheric variability with the ECMWF model: From synoptic to decadal time-scales*, Quarterly Journal of the Royal Meteorological Society, 134(634):1337–1351, doi: 10.1002/qj.289.
- Bechtold, P., N. Semane, P. Lopez, J.-P. Chaboureaud, A. Beljaars, and N. Bormann (2014), *Representing Equilibrium and Nonequilibrium Convection in Large-Scale Models*, Journal of the Atmospheric Sciences, 71(2):734–753, doi: 10.1175/JAS-D-13-0163.1.
- Berezin, Y., A. Gozolchiani, O. Guez, and S. Havlin (2012), *Stability of Climate Networks with Time*, Scientific Reports, 2(666), doi: 10.1038/srep00666.
- Berkopec, A. (2007), *HyperQuick algorithm for discrete hypergeometric distribution*, Journal of Discrete Algorithms, 5(2):341–347, doi: 10.1016/j.jda.2006.01.001.
- Betts, A. K. (1973), *Non-precipitating cumulus convection and its parameterization*, Quarterly Journal of the Royal Meteorological Society, 99(419):178–196, doi: 10.1002/qj.49709941915.
- Betts, A. K., and C. Jakob (2002), *Evaluation of the diurnal cycle of precipitation, surface thermodynamics, and surface fluxes in the ECMWF model using LBA data*, Journal of Geophysical Research: Atmospheres, 107(D20):LBA 12–1–LBA 12–8, doi: 10.1029/2001JD000427.
- Bjerknes, J. (1938), *Saturated-adiabatic ascent of air through dry-adiabatically descending environment*, Quarterly Journal of the Royal Meteorological Society, 64(275):325–330.
- Bjerknes, V. (1904), *Das Problem der Wettervorhersage, betrachtet von Standpunkte der Mechanik und der Physik*, Meteorologische Zeitschrift, 21:1–7, doi: 10.1127/0941-2948/2009/416.
- Blondel, V., A. Gajardo, M. Heymans, P. Senellart, and P. Van Dooren (2004), *A Measure of Similarity between Graph Vertices: Applications to Synonym Extraction and Web Searching*, SIAM Review, 46(4):647–666, doi: 10.1137/S0036144502415960.
- Boccaletti, S., V. Latora, Y. Moreno, M. Chavez, and D.-U. Hwang (2006), *Complex networks: Structure and dynamics*, Physics Reports, 424(4–5):175–308, doi: 10.1016/j.physrep.2005.10.009.
- Boers, N., B. Bookhagen, N. Marwan, J. Kurths, and J. Marengo (2013), *Complex networks identify spatial patterns of extreme rainfall events of the South American Monsoon System*, Geophysical Research Letters, 40(16):4386–4392, doi: 10.1002/grl.50681.
- Boers, N., B. Bookhagen, H. M. J. Barbosa, N. Marwan, J. Kurths, and J. A. Marengo (2014), *Prediction of extreme floods in the eastern Central Andes based on a complex networks approach*, Nature Communications, 5(5199), doi: 10.1038/ncomms6199.
- Böhm, U., F.-W. Gerstengarbe, D. Hauffe, M. Kücken, H. Österle, and P. C. Werner (2003), *Dynamic regional climate modeling and sensitivity experiments for the northeast of Brazil*, in *Global Change and Regional Impacts*, edited by T. Gaiser, M. Krol, H. Frischkorn, and J. C. de Araújo, pp. 153–170, Springer Berlin Heidelberg New York.

- Bookhagen, B., and M. R. Strecker (2008), *Orographic barriers, high-resolution TRMM rainfall, and relief variations along the eastern Andes*, *Geophysical Research Letters*, 35(6):L06403, doi: 10.1029/2007GL032011.
- Braconnot, P., F. Hourdin, S. Bony, J. Dufresne, J. Grandpeix, and O. Marti (2007), *Impact of different convective cloud schemes on the simulation of the tropical seasonal cycle in a coupled ocean-atmosphere model*, *Climate Dynamics*, 29(5):501–520, doi: 10.1007/s00382-007-0244-y.
- Brockhaus, P., P. Bechtold, O. Fuhrer, C. Hohenegger, D. Lüthi, and C. Schär (2009), *The ECMWF IFS convection scheme applied to the COSMO-CLM limited-area model*, *Quarterly Journal of the Royal Meteorological Society*, submitted.
- Cadule, P., P. Friedlingstein, L. Bopp, S. Sitch, C. D. Jones, P. Ciais, S. L. Piao, and P. Peylin (2010), *Benchmarking coupled climate-carbon models against long-term atmospheric CO₂ measurements*, *Global Biogeochemical Cycles*, 24(2), doi: 10.1029/2009GB003556.
- Carvalho, L. M. V., C. Jones, and B. Liebmann (2004), *The South Atlantic Convergence Zone: Intensity, Form, Persistence, and Relationships with Intraseasonal to Interannual Activity and Extreme Rainfall*, *Journal of Climate*, 17(1):88–108, doi: 10.1175/1520-0442(2004)017<0088:TSACZI>2.0.CO;2.
- Carvalho, L. M. V., C. Jones, A. N. D. Posadas, R. Quiroz, B. Bookhagen, and B. Liebmann (2012), *Precipitation Characteristics of the South American Monsoon System Derived from Multiple Data-sets*, *Journal of Climate*, 25(13):4600–4620, doi: 10.1175/JCLI-D-11-00335.1.
- Castro, C. L., S. Pielke, Roger A., and G. Leoncini (2005), *Dynamical downscaling: Assessment of value retained and added using the Regional Atmospheric Modeling System (RAMS)*, *Journal of Geophysical Research*, 110(D5):D05108, doi: 10.1029/2004JD004721.
- Ceselski, B. F. (1974), *Cumulus Convection in Weak and Strong Tropical Disturbances*, *Journal of the Atmospheric Sciences*, 31(5):1241–1255, doi: 10.1175/1520-0469(1974)031<1241:CCIWAS>2.0.CO;2.
- Christensen, J. H., K. E. F. Giorgi, G. Lenderink, and M. Rummukainen (2010), *Weight assignment in regional climate models*, *Climate Research*, 44(2–3):179–194, doi: 10.3354/cr00916.
- Cohen, J. C. P., M. A. F. Silva Dias, and C. A. Nobre (1995), *Environmental Conditions Associated with Amazonian Squall Lines: A Case Study*, *Monthly Weather Review*, 123(11):3163–3174, doi: 10.1175/1520-0493(1995)123<3163:ECAWAS>2.0.CO;2.
- Cook, B., N. Zeng, and J.-H. Yoon (2011), *Will Amazonia Dry Out? Magnitude and Causes of Change from IPCC Climate Model Projections*, *Earth Interactions*, 16(3):1–27, doi: 10.1175/2011EI398.1.
- Correia, F. W. S., R. C. S. Alvalá, and A. O. Manzi (2008), *Modeling the impacts of land cover change in Amazonia: a regional climate model (RCM) simulation study*, *Theoretical and Applied Climatology*, 93(3–4):225–244, doi: 10.1007/s00704-007-0335-z.
- Cushman-Roisin, B., and J.-M. Beckers (2011), *Introduction to Geophysical Fluid Dynamics: Physical and Numerical Aspects*, *International Geophysics*, vol. 101, 2 ed., Academic Press.
- da Rocha, R. P., C. A. Morales, S. V. Cuadra, and T. Ambrizzi (2009), *Precipitation diurnal cycle and summer climatology assessment over South America: An evaluation of Regional Climate Model*

- version 3 simulations, *Journal of Geophysical Research: Atmospheres*, 114(D10):D10108, doi: 10.1029/2008JD010212.
- Dai, A. (2006), *Precipitation Characteristics in Eighteen Coupled Climate Models*, *Journal of Climate*, 19(18):4605–4630, doi: 10.1175/JCLI3884.1.
- Dai, A., F. Giorgi, and K. E. Trenberth (1999), *Observed and model-simulated diurnal cycles of precipitation over the contiguous United States*, *Journal of Geophysical Research: Atmospheres*, 104(D6):6377–6402, doi: 10.1029/98JD02720.
- Davies, H. C. (1976), *A lateral boundary formulation for multi-level prediction models*, *Quarterly Journal of the Royal Meteorological Society*, 102(432):405–418, doi: 10.1002/qj.49710243210.
- Davin, E. L., and S. I. Seneviratne (2012), *Role of land surface processes and diffuse/direct radiation partitioning in simulating the European climate*, *Biogeosciences*, 9(5):1695–1707, doi: 10.5194/bg-9-1695-2012.
- de Jong, H. (2002), *Modeling and Simulation of Genetic Regulatory Systems: A Literature Review*, *Journal of Computational Biology*, 9(1):67–103, doi: 10.1089/10665270252833208.
- de Rooy, W. C., P. Bechtold, K. Fröhlich, C. Hohenegger, H. Jonker, D. Mironov, A. Pier Siebesma, J. Teixeira, and J.-I. Yano (2013), *Entrainment and detrainment in cumulus convection: an overview*, *Quarterly Journal of the Royal Meteorological Society*, 139(670):1–19, doi: 10.1002/qj.1959.
- Decker, M., M. A. Brunke, Z. Wang, K. Sakaguchi, X. Zeng, and M. G. Bosilovich (2011), *Evaluation of the Reanalysis Products from GSFC, NCEP, and ECMWF Using Flux Tower Observations*, *Journal of Climate*, 25(6):1916–1944, doi: 10.1175/JCLI-D-11-00004.1.
- Dee, D. P., S. M. Uppala, A. J. Simmons, P. Berrisford, P. Poli, S. Kobayashi, U. Andrae, M. A. Balmaseda, G. Balsamo, P. Bauer, P. Bechtold, A. C. M. Beljaars, L. van de Berg, J. Bidlot, N. Bormann, C. Delsol, R. Dragani, M. Fuentes, A. J. Geer, L. Haimberger, S. B. Healy, H. Hersbach, E. V. Hólm, L. Isaksen, P. Kållberg, M. Köhler, M. Matricardi, A. P. McNally, B. M. Monge-Sanz, J.-J. Morcrette, B.-K. Park, C. Peubey, P. de Rosnay, C. Tavolato, J.-N. Thépaut, and F. Vitart (2011), *The ERA-Interim reanalysis: configuration and performance of the data assimilation system*, *Quarterly Journal of the Royal Meteorological Society*, 137(656):553–597, doi: 10.1002/qj.828.
- Dickinson, R., A. Henderson-Sellers, P. Kennedy, and M. Wilson (1986), *Biosphere-atmosphere transfer scheme (BATS) forcing the ncar community climate model*, *NCAR Technical Note TN275+STR*, NCAR.
- Dickinson, R., R. Errico, F. Giorgi, and G. Bates (1989), *A regional climate model for the western United States*, *Climatic Change*, 15(3):383–422, doi: 10.1007/BF00240465.
- Dickinson, R. E. (1984), *Climate Processes and Climate Sensitivity*, vol. 29, chap. Modeling Evapotranspiration for Three-Dimensional Global Climate Models, pp. 58–72, American Geophysical Union, John Wiley & Sons Ltd, doi: 10.1029/GM029p0058.
- Dobler, A., and B. Ahrens (2010), *Analysis of the Indian summer monsoon system in the regional climate model COSMO-CLM*, *Journal of Geophysical Research*, 115:D16101, doi: 10.1029/2009JD013497.

- Doms, G., J. Förstner, E. Heise, H.-J. Herzog, D. Mironov, M. Raschendorfer, T. Reinhardt, B. Ritter, R. Schrodin, J.-P. Schulz, and G. Vogel (2011a), *A Description of the Nonhydrostatic Regional COSMO Model, Part II: Physical Parameterization*, Deutscher Wetterdienst.
- Doms, G., U. Schättler, and M. Baldauf (2011b), *A Description of the Nonhydrostatic Regional COSMO Model, Part I: Dynamics and Numerics*, Deutscher Wetterdienst.
- Donges, J. F. (2012), *Functional network macroscopes for probing past and present Earth system dynamics – complex hierarchical interactions, tipping points, and beyond*, Ph.D. thesis, Humboldt-Universität zu Berlin, Mathematisch-Naturwissenschaftliche Fakultät I.
- Donges, J. F., Y. Zou, N. Marwan, and J. Kurths (2009a), *The backbone of the climate network*, Europhysics Letters, 87(4):48007, doi: 10.1209/0295-5075/87/48007.
- Donges, J. F., Y. Zou, N. Marwan, and J. Kurths (2009b), *Complex networks in climate dynamics*, The European Physical Journal Special Topics, 174(1):157–179, doi: 10.1140/epjst/e2009-01098-2.
- Donges, J. F., H. C. H. Schultz, N. Marwan, Y. Zou, and J. Kurths (2011), *Investigating the topology of interacting networks*, The European Physical Journal B, 84(4):635–651, doi: 10.1140/epjb/e2011-10795-8.
- Donner, L., W. Schubert, and R. Somerville (Eds.) (2011), *The Development of Atmospheric General Circulation Models: Complexity, Synthesis and Computation*, Cambridge University Press, Cambridge, UK.
- ECMWF (2009), *IFS Documentation Cy33r1, Part IV: Physical Processes*, Shinfield Park, Reading, RG2 9AX, England.
- Efron, B. (1979), *Bootstrap Methods: Another Look at the Jackknife*, The Annals of Statistics, 7(1):1–26, doi: 10.1214/aos/1176344552.
- Erbach-Schoenberg, E. z., S. Bullock, and S. Brailsford (2014), *A Model of Spatially Constrained Social Network Dynamics*, Social Science Computer Review, 32(3):373–392, doi: 10.1177/0894439313511934.
- Erdős, P., and A. Rényi (1959), *On Random Graphs I*, Publicationes Mathematicae Debrecen, 6:290–297.
- Feldhoff, J. H., S. Lange, J. Volkholz, J. F. Donges, J. Kurths, and F.-W. Gerstengarbe (2015), *Complex networks for climate model evaluation with application to statistical versus dynamical modeling of South American climate*, Climate Dynamics, 44(5–6):1567–1581, doi: 10.1007/s00382-014-2182-9.
- Fieller, E. C., and E. S. Pearson (1961), *Tests for Rank Correlation Coefficients: II*, Biometrika, 48(1–2):29–40, doi: 10.2307/2333127.
- Fieller, E. C., H. O. Hartley, and E. S. Pearson (1957), *Tests for Rank Correlation Coefficients. I*, Biometrika, 44(3–4):470–481, doi: 10.2307/2332878.
- Fischer, E. M., U. Beyerle, and R. Knutti (2013a), *Robust spatially aggregated projections of climate extremes*, Nature Climate Change, 3(12):1033–1038, doi: 10.1038/nclimate2051.

Bibliography

- Fischer, T., C. Menz, B. Su, and T. Scholten (2013b), *Simulated and projected climate extremes in the Zhujiang River Basin, South China, using the regional climate model COSMO-CLM*, International Journal of Climatology, 33:2988–3001, doi: 10.1002/joc.3643.
- Fisher, R. A. (1915), *Frequency Distribution of the Values of the Correlation Coefficient in Samples from an Indefinitely Large Population*, Biometrika, 10(4):507–521.
- Fisher, R. A. (1921), *On the “probable error” of a coefficient of correlation deduced from a small sample*, Metron, 1:3–32.
- Flato, G., J. Marotzke, B. Abiodun, P. Braconnot, S. C. Chou, W. Collins, P. Cox, F. Driouech, S. Emori, V. Eyring, C. Forest, P. Gleckler, E. Guilyardi, C. Jakob, V. Kattsov, C. Reason, and M. Rummukainen (2013), *Climate Change 2013: The Physical Science Basis. Contribution of Working Group I to the Fifth Assessment Report of the Intergovernmental Panel on Climate Change*, chap. Evaluation of Climate Models, pp. 741–866, Cambridge University Press, Cambridge, UK and New York, NY, USA.
- Fountalis, I., A. Bracco, and C. Drovolis (2013), *Spatio-temporal network analysis for studying climate patterns*, Climate Dynamics, 42(3–4):879–899, doi: 10.1007/s00382-013-1729-5.
- Fountalis, I., A. Bracco, and C. Drovolis (2014), *ENSO in CMIP5 simulations: network connectivity from the recent past to the twenty-third century*, Climate Dynamics, doi: 10.1007/s00382-014-2412-1.
- Fritsch, J. M., and C. F. Chappell (1980), *Numerical Prediction of Convectively Driven Mesoscale Pressure Systems. Part I: Convective Parameterization*, Journal of the Atmospheric Sciences, 37(8):1722–1733, doi: 10.1175/1520-0469(1980)037<1722:NPOCDM>2.0.CO;2.
- Galbraith, D., P. E. Levy, S. Sitch, C. Huntingford, P. Cox, M. Williams, and P. Meir (2010), *Multiple mechanisms of Amazonian forest biomass losses in three dynamic global vegetation models under climate change*, New Phytologist, 187(3):647–665, doi: 10.1111/j.1469-8137.2010.03350.x.
- Garreaud, R. D., M. Vuille, R. Compagnucci, and J. Marengo (2009), *Present-day South American climate*, Palaeogeography, Palaeoclimatology, Palaeoecology, 281(3–4):180–195, doi: <http://dx.doi.org/10.1016/j.palaeo.2007.10.032>.
- Garstang, M., H. L. Massie, J. Halverson, S. Greco, and J. Scala (1994), *Amazon Coastal Squall Lines. Part I: Structure and Kinematics*, Monthly Weather Review, 122(4):608–622, doi: 10.1175/1520-0493(1994)122<0608:ACSLPI>2.0.CO;2.
- Giorgi, F. (1990), *Simulation of Regional Climate Using a Limited Area Model Nested in a General Circulation Model*, Journal of Climate, 3(9):941–963, doi: 10.1175/1520-0442(1990)003<0941:SORCUA>2.0.CO;2.
- Giorgi, F., C. Jones, and G. R. Asrar (2009), *Addressing climate information needs at the regional level: the CORDEX framework*, WMO Bulletin, 58(3):175–183.
- Gleckler, P. J., K. E. Taylor, and C. Doutriaux (2008), *Performance metrics for climate models*, Journal of Geophysical Research: Atmospheres, 113(D6), doi: 10.1029/2007JD008972.
- Golding, B. W. (1998), *Nimrod: a system for generating automated very short range forecasts*, Meteorological Applications, 5(1):1–16, doi: 10.1017/S1350482798000577.

- Görsdorf, U., A. Seifert, V. Lehmann, and M. Köhler (2011), *Cloud statistics and NWP-model validation based on long term measurements of a 35 GHz radar*, in *35th Conference on Radar Meteorology*, pp. 26–30.
- Gozolchiani, A., S. Havlin, and K. Yamasaki (2011), *Emergence of El Niño as an Autonomous Component in the Climate Network*, *Physical Review Letters*, 107:148501, doi: 10.1103/PhysRevLett.107.148501.
- Grabowski, W. W., P. Bechtold, A. Cheng, R. Forbes, C. Halliwell, M. Khairoutdinov, S. Lang, T. Nasuno, J. Petch, W.-K. Tao, R. Wong, X. Wu, and K.-M. Xu (2006), *Daytime convective development over land: A model intercomparison based on LBA observations*, *Quarterly Journal of the Royal Meteorological Society*, 132(615):317–344, doi: 10.1256/qj.04.147.
- Graham, R. L., D. E. Knuth, and O. Patashnik (1989), *Concrete mathematics: a foundation for computer science*, Addison-Wesley, Boston, MA, USA.
- Gregg, W. W., and N. W. Casey (2004), *Global and regional evaluation of the SeaWiFS chlorophyll data set*, *Remote Sensing of Environment*, 93(4):463–479, doi: 10.1016/j.rse.2003.12.012.
- Gregory, D., J.-J. Morcrette, C. Jakob, A. C. M. Beljaars, and T. Stockdale (2000), *Revision of convection, radiation and cloud schemes in the ECMWF integrated forecasting system*, *Quarterly Journal of the Royal Meteorological Society*, 126(566):1685–1710, doi: 10.1002/qj.49712656607.
- Greicius, M. D., B. H. Flores, V. Menon, G. H. Glover, H. B. Solvason, H. Kenna, A. L. Reiss, and A. F. Schatzberg (2007), *Resting-State Functional Connectivity in Major Depression: Abnormally Increased Contributions from Subgenual Cingulate Cortex and Thalamus*, *Biological Psychiatry*, 62(5):429–437, doi: 10.1016/j.biopsych.2006.09.020.
- Hamming, R. (1950), *Error Detecting and Error Correcting Codes*, *Bell System Technical Journal*, 29(2):147–160, doi: 10.1002/j.1538-7305.1950.tb00463.x.
- Handorf, D., and K. Dethloff (2012), *How well do state-of-the-art atmosphere-ocean general circulation models reproduce atmospheric teleconnection patterns?*, *Tellus A*, 64(0), doi: 10.3402/tellusa.v64i0.19777.
- Harris, I., P. D. Jones, T. J. Osborn, and D. H. Lister (2013), *Updated high-resolution grids of monthly climatic observations – the CRU TS3.10 Dataset*, *International Journal of Climatology*, doi: 10.1002/joc.3711.
- Heitzig, J., J. F. Donges, Y. Zou, N. Marwan, and J. Kurths (2012), *Node-weighted measures for complex networks with spatially embedded, sampled, or differently sized nodes*, *The European Physical Journal B*, 85:1–22, doi: 10.1140/epjb/e2011-20678-7.
- Held, I. M. (2005), *The Gap between Simulation and Understanding in Climate Modeling*, *Bulletin of the American Meteorological Society*, 86(11):1609–1614, doi: 10.1175/BAMS-86-11-1609.
- Ho, J. W. K., and M. A. Charleston (2011), *Network modelling of gene regulation*, *Biophysical Reviews*, 3(1):1–13, doi: 10.1007/s12551-010-0041-4.
- Hodges, J. S., and J. A. Dewar (1992), *Is It You or Your Model Talking? A Framework for Model Validation*, R-4114-AF/A/OSD, RAND, Santa Monica, CA, USA.

Bibliography

- Hohenegger, C., P. Brockhaus, and C. Schar (2008), *Towards climate simulations at cloud-resolving scales*, *Meteorologische Zeitschrift*, 17(4):383–394, doi: 10.1127/0941-2948/2008/0303.
- Hohenegger, C., P. Brockhaus, C. S. Bretherton, and C. Schär (2009), *The Soil Moisture-Precipitation Feedback in Simulations with Explicit and Parameterized Convection*, *Journal of Climate*, 22(19):5003–5020, doi: 10.1175/2009JCLI2604.1.
- Hörmann, W. (1994), *A universal generator for discrete log-concave distributions*, *Computing*, 52(1):89–96, doi: 10.1007/BF02243398.
- Huff, F. A., and W. L. Shipp (1969), *Spatial Correlations of Storm, Monthly and Seasonal Precipitation*, *Journal of Applied Meteorology*, 8(4):542–550, doi: 10.1175/1520-0450(1969)008<0542:SCOSMA>2.0.CO;2.
- Huffman, G. J., D. T. Bolvin, E. J. Nelkin, D. B. Wolff, R. F. Adler, G. Gu, Y. Hong, K. P. Bowman, and E. F. Stocker (2007), *The TRMM Multisatellite Precipitation Analysis (TMPA): Quasi-Global, Multiyear, Combined-Sensor Precipitation Estimates at Fine Scales*, *Journal of Hydrometeorology*, 8(1):38–55, doi: 10.1175/JHM560.1.
- Hurrell, J. W. (1995), *Decadal Trends in the North Atlantic Oscillation: Regional Temperatures and Precipitation*, *Science*, 269(5224):676–679, doi: 10.1126/science.269.5224.676.
- Jaccard, P. (1901), *Étude comparative de la distribution florale dans une portion des Alpes et du Jura*, *Bulletin de la Société Vaudoise des Sciences Naturelles*, 37:547–579.
- Jaeger, E. B., I. Anders, D. Lüthi, B. Rockel, C. Schär, and S. I. Seneviratne (2008), *Analysis of ERA40-driven CLM simulations for Europe*, *Meteorologische Zeitschrift*, 17(4):349–367, doi: 10.1127/0941-2948/2008/0301.
- Joetzier, E., H. Douville, C. Delire, and P. Ciais (2013), *Present-day and future Amazonian precipitation in global climate models: CMIP5 versus CMIP3*, *Climate Dynamics*, 41(11–12):2921–2936, doi: 10.1007/s00382-012-1644-1.
- Jones, C., and L. M. V. Carvalho (2002), *Active and Break Phases in the South American Monsoon System*, *Journal of Climate*, 15(8):905–914, doi: 10.1175/1520-0442(2002)015<0905:AABPIT>2.0.CO;2.
- Jones, P. W. (1999), *First- and Second-Order Conservative Remapping Schemes for Grids in Spherical Coordinates*, *Monthly Weather Review*, 127(9):2204–2210, doi: 10.1175/1520-0493(1999)127<2204:FASOCR>2.0.CO;2.
- Kalnay, E., M. Kanamitsu, R. Kistler, W. Collins, D. Deaven, L. Gandin, M. Iredell, S. Saha, G. White, J. Woollen, Y. Zhu, A. Leetmaa, R. Reynolds, M. Chelliah, W. Ebisuzaki, W. Higgins, J. Janowiak, K. C. Mo, C. Ropelewski, J. Wang, R. Jenne, and D. Joseph (1996), *The NCEP/NCAR 40-Year Reanalysis Project*, *Bulletin of the American Meteorological Society*, 77(3):437–471, doi: 10.1175/1520-0477(1996)077<0437:TNYRP>2.0.CO;2.
- Kendall, M. G. (1945), *The treatment of ties in ranking problems*, *Biometrika*, 33(3):239–251, doi: 10.1093/biomet/33.3.239.
- Koren, I., L. Oreopoulos, G. Feingold, L. A. Remer, and O. Altaratz (2008), *How small is a small cloud?*, *Atmospheric Chemistry and Physics*, 8(14):3855–3864, doi: 10.5194/acp-8-3855-2008.

- Koster, R. D., and M. J. Suarez (2001), *Soil Moisture Memory in Climate Models*, *Journal of Hydrometeorology*, 2(6):558–570, doi: 10.1175/1525-7541(2001)002<0558:SMMICM>2.0.CO;2.
- Koster, R. D., P. A. Dirmeyer, Z. Guo, G. Bonan, E. Chan, P. Cox, C. T. Gordon, S. Kanae, E. Kowalczyk, D. Lawrence, P. Liu, C.-H. Lu, S. Malyshev, B. McAvaney, K. Mitchell, D. Mocko, T. Oki, K. Oleson, A. Pitman, Y. C. Sud, C. M. Taylor, D. Verseghy, R. Vasic, Y. Xue, and T. Yamada (2004), *Regions of Strong Coupling Between Soil Moisture and Precipitation*, *Science*, 305(5687):1138–1140, doi: 10.1126/science.1100217.
- Lange, S., B. Rockel, J. Volkholz, and B. Bookhagen (2015a), *Regional climate model sensitivities to parametrizations of convection and non-precipitating subgrid-scale clouds over South America*, *Climate Dynamics*, 44(9–10):2839–2857, doi: 10.1007/s00382-014-2199-0.
- Lange, S., J. F. Donges, J. Volkholz, and J. Kurths (2015b), *Local difference measures between complex networks for dynamical system model evaluation*, *PLoS ONE*, 10(4):e0118088, doi: 10.1371/journal.pone.0118088.
- Lau, N.-C. (1981), *A Diagnostic Study of Recurrent Meteorological Anomalies Appearing in a 15-Year Simulation with a GFDL General Circulation Model*, *Monthly Weather Review*, 109(11):2287–2311, doi: 10.1175/1520-0493(1981)109<2287:ADSORM>2.0.CO;2.
- Leicht, E. A., P. Holme, and M. E. J. Newman (2006), *Vertex similarity in networks*, *Physical Review E*, 73:026120, doi: 10.1103/PhysRevE.73.026120.
- Levermann, A. (2014), *Comment: Make supply chains climate-smart*, *Nature*, 506:27–29, doi: 10.1038/506027a.
- Li, Z., F. Brissette, and J. Chen (2013), *Finding the most appropriate precipitation probability distribution for stochastic weather generation and hydrological modelling in Nordic watersheds*, *Hydrological Processes*, 27(25):3718–3729, doi: 10.1002/hyp.9499.
- Liebmann, B., S. J. Camargo, A. Seth, J. A. Marengo, L. M. V. Carvalho, D. Allured, R. Fu, and C. S. Vera (2007), *Onset and End of the Rainy Season in South America in Observations and the ECHAM 4.5 Atmospheric General Circulation Model*, *Journal of Climate*, 20(10):2037–2050, doi: 10.1175/JCLI4122.1.
- Liersch, S., J. Cools, B. Kone, H. Koch, M. Diallo, J. Reinhardt, S. Fournet, V. Aich, and F. F. Hattermann (2012), *Vulnerability of rice production in the Inner Niger Delta to water resources management under climate variability and change*, *Environmental Science & Policy*, 34:18–33, doi: <http://dx.doi.org/10.1016/j.envsci.2012.10.014>.
- Lin, J.-L., T. Shinoda, B. Liebmann, T. Qian, W. Han, P. Roundy, J. Zhou, and Y. Zheng (2009), *Intraseasonal Variability Associated with Summer Precipitation over South America Simulated by 14 IPCC AR4 Coupled GCMs*, *Monthly Weather Review*, 137(9):2931–2954, doi: 10.1175/2009MWR2777.1.
- Lindzen, R. S. (1988), *Some remarks on cumulus parameterization*, *Pure and Applied Geophysics*, 126(1):123–135, doi: 10.1007/BF00876918.
- Liu, X.-D., S. Osher, and T. Chan (1994), *Weighted Essentially Non-oscillatory Schemes*, *Journal of Computational Physics*, 115(1):200–212, doi: 10.1006/jcph.1994.1187.

Bibliography

- Lorenz, E. (1960), *Energy and Numerical Weather Prediction*, *Tellus A*, 12(4), doi: 10.1111/j.2153-3490.1960.tb01323.x.
- Lorrain, F., and H. C. White (1971), *Structural equivalence of individuals in social networks*, *The Journal of Mathematical Sociology*, 1(1):49–80, doi: 10.1080/0022250X.1971.9989788.
- Loveland, T. R., B. C. Reed, J. F. Brown, D. O. Ohlen, Z. Zhu, L. Yang, and J. W. Merchant (2000), *Development of a global land cover characteristics database and IGBP DISCover from 1 km AVHRR data*, *International Journal of Remote Sensing*, 21(6–7):1303–1330, doi: 10.1080/014311600210191.
- Lucarini, V. (2008), *Encyclopedia of Global Warming and Climate Change*, chap. Validation of climate models, pp. 1053–1057, SAGE, Thousand Oaks, CA, USA.
- Lucarini, V., and F. Ragone (2011), *Energetics of Climate Models: Net Energy Balance and Meridional Enthalpy Transport*, *Reviews of Geophysics*, 49(1), doi: 10.1029/2009RG000323.
- Ludescher, J., A. Gozolchiani, M. I. Bogachev, A. Bunde, S. Havlin, and H. J. Schellnhuber (2013), *Improved El Niño forecasting by cooperativity detection*, *Proceedings of the National Academy of Sciences*, 110(29):11742–11745, doi: 10.1073/pnas.1309353110.
- Lutz, J., J. Volkholz, and F.-W. Gerstengarbe (2013), *Climate projections for southern Africa using complementary methods*, *International Journal of Climate Change Strategies and Management*, 5(2):130–151, doi: 10.1108/17568691311327550.
- Lux, T., and M. Marchesi (1999), *Scaling and criticality in a stochastic multi-agent model of a financial market*, *Nature*, 397(6719):498–500, doi: 10.1038/17290.
- Lynall, M.-E., D. S. Bassett, R. Kerwin, P. J. McKenna, M. Kitzbichler, U. Muller, and E. Bullmore (2010), *Functional Connectivity and Brain Networks in Schizophrenia*, *The Journal of Neuroscience*, 30(28):9477–9487, doi: 10.1523/JNEUROSCI.0333-10.2010.
- Madden, R. A., and P. R. Julian (1994), *Observations of the 40-50-Day Tropical Oscillation—A Review*, *Monthly Weather Review*, 122(5):814–837, doi: 10.1175/1520-0493(1994)122<0814:OOTDTC>2.0.CO;2.
- Malik, N., B. Bookhagen, N. Marwan, and J. Kurths (2012), *Analysis of spatial and temporal extreme monsoonal rainfall over South Asia using complex networks*, *Climate Dynamics*, 39(3–4):971–987, doi: 10.1007/s00382-011-1156-4.
- Manabe, S., J. Smagorinsky, and R. F. Strickler (1965), *Simulated Climatology of a General Circulation Model with a Hydrological Cycle*, *Monthly Weather Review*, 93(12):769–798, doi: 10.1175/1520-0493(1965)093<0769:SCOAGC>2.3.CO;2.
- Maraun, D., F. Wetterhall, A. M. Ireson, R. E. Chandler, E. J. Kendon, M. Widmann, S. Brienen, H. W. Rust, T. Sauter, M. Themeßl, V. K. C. Venema, K. P. Chun, C. M. Goodess, R. G. Jones, C. Onof, M. Vrac, and I. Thiele-Eich (2010), *Precipitation downscaling under climate change: Recent developments to bridge the gap between dynamical models and the end user*, *Reviews of Geophysics*, 48(3), doi: 10.1029/2009RG000314.
- Marengo, J., T. Ambrizzi, R. da Rocha, L. Alves, S. Cuadra, M. Valverde, R. Torres, D. Santos, and S. Ferraz (2010), *Future change of climate in South America in the late twenty-first century: inter-comparison of scenarios from three regional climate models*, *Climate Dynamics*, 35:1073–1097, doi: 10.1007/s00382-009-0721-6, 10.1007/s00382-009-0721-6.

- Marengo, J. A., W. R. Soares, C. Saulo, and M. Nicolini (2004), *Climatology of the Low-Level Jet East of the Andes as Derived from the NCEP-NCAR Reanalyses: Characteristics and Temporal Variability*, *Journal of Climate*, 17(12):2261–2280, doi: 10.1175/1520-0442(2004)017<2261:COTLJE>2.0.CO;2.
- Marengo, J. A., R. Jones, L. M. Alves, and M. C. Valverde (2009), *Future change of temperature and precipitation extremes in South America as derived from the PRECIS regional climate modeling system*, *International Journal of Climatology*, 29(15):2241–2255, doi: 10.1002/joc.1863.
- Marengo, J. A., S. C. Chou, G. Kay, L. M. Alves, J. F. Pesquero, W. R. . Soares, D. C. Santos, A. A. Lyra, G. Sueiro, R. Betts, D. J. Chagas, J. L. Gomes, J. F. Bustamante, and P. Tavares (2012a), *Development of regional future climate change scenarios in South America using the Eta CPTEC/HadCM3 climate change projections: climatology and regional analyses for the Amazon, São Francisco and the Paraná River basins*, *Climate Dynamics*, 38(9–10):1829–1848, doi: 10.1007/s00382-011-1155-5.
- Marengo, J. A., B. Liebmann, A. M. Grimm, V. Misra, P. L. Silva Dias, I. F. A. Cavalcanti, L. M. V. Carvalho, E. H. Berbery, T. Ambrizzi, C. S. Vera, A. C. Saulo, J. Noguez-Paegle, E. Zipser, A. Seth, and L. M. Alves (2012b), *Recent developments on the South American monsoon system*, *International Journal of Climatology*, 32(1):1–21, doi: 10.1002/joc.2254.
- Marshall, G. J. (2002), *Trends in Antarctic Geopotential Height and Temperature: A Comparison between Radiosonde and NCEP-NCAR Reanalysis Data*, *Journal of Climate*, 15(6):659–674, doi: 10.1175/1520-0442(2002)015<0659:TIAGHA>2.0.CO;2.
- Matsoukas, C., S. Islam, and I. Rodriguez-Iturbe (2000), *Detrended fluctuation analysis of rainfall and streamflow time series*, *Journal of Geophysical Research: Atmospheres*, 105(D23):29165–29172, doi: 10.1029/2000JD900419.
- McCartney, S. (1999), *ENIAC: The Triumphs and Tragedies of the World's First Computer*, Walker & Company.
- Mechoso, C. R., A. W. Robertson, C. F. Ropelewski, and A. M. Grimm (2005), *The American Monsoon Systems*, in *The Global monsoon system : research and forecast : report of the International Committee of the Third International Workshop on Monsoons (IWM-III) 2-6*, World Meteorological Organization.
- Mellor, G. L., and T. Yamada (1982), *Development of a turbulence closure model for geophysical fluid problems*, *Reviews of Geophysics*, 20(4):851–875, doi: 10.1029/RG020i004p00851.
- Mendes, D., E. P. Souza, J. A. Marengo, and M. C. D. Mendes (2010), *Climatology of extratropical cyclones over the South American-southern oceans sector*, *Theoretical and Applied Climatology*, 100(3–4):239–250, doi: 10.1007/s00704-009-0161-6.
- Miller, R. L., G. A. Schmidt, and D. T. Shindell (2006), *Forced annular variations in the 20th century Intergovernmental Panel on Climate Change Fourth Assessment Report models*, *Journal of Geophysical Research: Atmospheres*, 111(D18), doi: 10.1029/2005JD006323.
- Mironov, D. (2009), *Turbulence in the Lower Troposphere: Second-Order Closure and Mass-Flux Modelling Frameworks*, in *Interdisciplinary Aspects of Turbulence*, vol. 756, edited by W. Hillebrandt and F. Kupka, pp. 1–61, Springer Berlin Heidelberg, doi: 10.1007/978-3-540-78961-1_5.

Bibliography

- Molion, L. C. B. (1993), *Amazonia rainfall and its variability*, pp. 99–111, International Hydrology Series, Cambridge University Press, Cambridge, UK.
- Morcrette, J.-J., H. W. Barker, J. N. S. Cole, M. J. Iacono, and R. Pincus (2008), *Impact of a New Radiation Package, McRad, in the ECMWF Integrated Forecasting System*, *Monthly Weather Review*, 136(12):4773–4798, doi: 10.1175/2008MWR2363.1.
- Murphy, A. H. (1993), *What Is a Good Forecast? An Essay on the Nature of Goodness in Weather Forecasting*, *Weather and Forecasting*, 8(2):281–293, doi: 10.1175/1520-0434(1993)008<0281:WIAGFA>2.0.CO;2.
- Murphy, J. M., D. M. H. Sexton, D. N. Barnett, G. S. Jones, M. J. Webb, M. Collins, and D. A. Stainforth (2004), *Quantification of modelling uncertainties in a large ensemble of climate change simulations*, *Nature*, 430(7001):768–772, doi: 10.1038/nature02771.
- Murray, F. W. (1967), *On the Computation of Saturation Vapor Pressure*, *Journal of Applied Meteorology*, 6(1):203–204, doi: 10.1175/1520-0450(1967)006<0203:OTCOSV>2.0.CO;2.
- Nepstad, D. C., C. R. de Carvalho, E. A. Davidson, P. H. Jipp, P. A. Lefebvre, G. H. Negreiros, E. D. da Silva, T. A. Stone, S. E. Trumbore, and S. Vieira (1994), *The role of deep roots in the hydrological and carbon cycles of Amazonian forests and pastures*, *Nature*, 372(6507):666–669, doi: 10.1038/372666a0.
- Newman, M. (2003), *The Structure and Function of Complex Networks*, *SIAM Review*, 45(2):167–256, doi: 10.1137/S003614450342480.
- Nicolini, M., P. Salio, J. J. Katzfey, J. L. McGregor, and A. C. Saulo (2002), *January and July regional climate simulation over South America*, *Journal of Geophysical Research: Atmospheres*, 107(D22):ACL 12–1–ACL 12–13, doi: 10.1029/2001JD000736.
- Nikulin, G., C. Jones, F. Giorgi, G. Asrar, M. Büchner, R. Cerezo-Mota, O. B. Christensen, M. Déqué, J. Fernandez, A. Hänsler, E. van Meijgaard, P. Samuelsson, M. B. Sylla, and L. Sushama (2012), *Precipitation Climatology in an Ensemble of CORDEX-Africa Regional Climate Simulations*, *Journal of Climate*, 25(18):6057–6078, doi: 10.1175/JCLI-D-11-00375.1.
- Nogués-Paegle, J., and K. C. Mo (1997), *Alternating Wet and Dry Conditions over South America during Summer*, *Monthly Weather Review*, 125(2):279–291, doi: 10.1175/1520-0493(1997)125<0279:AWADCO>2.0.CO;2.
- Nogués-Paegle, J., C. R. Mechoso, R. Fu, E. H. Berbery, W. C. Chao, T.-C. Chen, K. Cook, A. F. Diaz, D. Enfield, R. Ferreira, A. M. Grimm, V. Kousky, B. Liebmann, J. Marengo, K. Mo, J. D. Neelin, J. Paegle, A. W. Robertson, A. Seth, C. S. Vera, and J. Zhou (2002), *Progress in Pan American CLIVAR research: Understanding the South American Monsoon*, *Meteorologica*, 27(1):3–32.
- Nordeng, T. E. (1994), *Extended versions of the convection parametrization scheme at ECMWF and their impact upon the mean climate and transient activity of the model in the tropics*, ECMWF Technical Memorandum, 206.
- Oreskes, N. (1998), *Evaluation (Not Validation) of Quantitative Models*, *Environmental Health Perspectives*, 106(Suppl. 6):1453–1460, doi: 10.1289/ehp.98106s61453.

- Orlowsky, B., F.-W. Gerstengarbe, and P. C. Werner (2008), *A resampling scheme for regional climate simulations and its performance compared to a dynamical RCM*, Theoretical and Applied Climatology, 92(3–4):209–223, doi: 10.1007/s00704-007-0352-y.
- Orlowsky, B., O. Bothe, K. Fraedrich, F.-W. Gerstengarbe, and X. Zhu (2010), *Future Climates from Bias-Bootstrapped Weather Analogs: An Application to the Yangtze River Basin*, Journal of Climate, 23(13):3509–3524, doi: 10.1175/2010JCLI3271.1.
- Panitz, H.-J., A. Dosio, M. Büchner, D. Lüthi, and K. Keuler (2013), *COSMO-CLM (CCLM) climate simulations over CORDEX-Africa domain: analysis of the ERA-Interim driven simulations at 0.44° and 0.22° resolution*, Climate Dynamics, doi: 10.1007/s00382-013-1834-5.
- Parry, M. L., O. F. Canziani, J. P. Palutikof, P. J. van der Linder, and C. E. Hanson (2007), *Climate Change 2007: Impacts, Adaptation and Vulnerability. Contribution of Working Group II to the Fourth Assessment Report of the Intergovernmental Panel on Climate Change*, chap. IPCC, 2007: Summary for Policymakers, pp. 7–22, Cambridge University Press, Cambridge, UK.
- Pearson, K. (1895), *Note on Regression and Inheritance in the Case of Two Parents*, Proceedings of the Royal Society of London, 58(347–352):240–242, doi: 10.1098/rspl.1895.0041.
- Peters, O., C. Hertlein, and K. Christensen (2001), *A Complexity View of Rainfall*, Physical Review Letters, 88:018701, doi: 10.1103/PhysRevLett.88.018701.
- Petkovšek, M., H. S. Wilf, and D. Zeilberger (1996), *A = B*, AK Peters Ltd.
- Phillips, N. A. (1956), *The general circulation of the atmosphere: A numerical experiment*, Quarterly Journal of the Royal Meteorological Society, 82(352):123–164, doi: 10.1002/qj.49708235202.
- Phillips, N. A., and J. Shukla (1973), *On the Strategy of Combining Coarse and Fine Grid Meshes in Numerical Weather Prediction*, Journal of Applied Meteorology, 12(5):763–770, doi: 10.1175/1520-0450(1973)012<0763:OTSOCC>2.0.CO;2.
- Pierce, D. W., T. P. Barnett, B. D. Santer, and P. J. Gleckler (2009), *Selecting global climate models for regional climate change studies*, Proceedings of the National Academy of Sciences, 106(21):8441–8446, doi: 10.1073/pnas.0900094106.
- Pincus, R., C. P. Batstone, R. J. P. Hofmann, K. E. Taylor, and P. J. Glecker (2008), *Evaluating the present-day simulation of clouds, precipitation, and radiation in climate models*, Journal of Geophysical Research: Atmospheres, 113(D14), doi: 10.1029/2007JD009334.
- Plank, V. G. (1969), *The Size Distribution of Cumulus Clouds in Representative Florida Populations*, Journal of Applied Meteorology, 8(1):46–67, doi: 10.1175/1520-0450(1969)008<0046:TSDOCC>2.0.CO;2.
- Popper, K. R. (1937), *The logic of scientific discovery*, Harper Torchbooks, New York, NY, USA.
- Popper, K. R. (1963), *Conjectures and Refutations: The Growth of Scientific Knowledge*, Harper Torchbooks, New York, NY, USA.
- Pritchard, M. S., M. W. Moncrieff, and R. C. J. Somerville (2011), *Orogenic Propagating Precipitation Systems over the United States in a Global Climate Model with Embedded Explicit Convection*, Journal of the Atmospheric Sciences, 68(8):1821–1840, doi: 10.1175/2011JAS3699.1.

Bibliography

- Quiroga, R. Q., T. Kreuz, and P. Grassberger (2002), *Event synchronization: A simple and fast method to measure synchronicity and time delay patterns*, Physical Review E, 66:041904, doi: 10.1103/PhysRevE.66.041904.
- Radebach, A., R. V. Donner, J. Runge, J. F. Donges, and J. Kurths (2013), *Disentangling different types of El Niño episodes by evolving climate network analysis*, Physical Review E, 88:052807, doi: 10.1103/PhysRevE.88.052807.
- Randall, D., M. Khairoutdinov, A. Arakawa, and W. Grabowski (2003), *Breaking the Cloud Parameterization Deadlock*, Bulletin of the American Meteorological Society, 84(11):1547–1564, doi: 10.1175/BAMS-84-11-1547.
- Randall, D. A., R. A. Wood, S. Bony, R. Colman, T. Fichefet, J. Fyfe, V. Kattsov, A. Pitman, J. Shukla, J. Srinivasan, R. J. Stouffer, A. Sumi, and K. E. Taylor (2007), *Climate Change 2007: The Physical Science Basis. Contribution of Working Group I to the Fourth Assessment Report of the Intergovernmental Panel on Climate Change*, chap. Climate Models and Their Evaluation, Cambridge University Press, Cambridge, UK and New York, NY, USA.
- Raschendorfer, M. (2001), *The new turbulence parameterization of LM*, COSMO Newsletter 1, Deutscher Wetterdienst, 90–98.
- Ravasz, E., A. L. Somera, D. A. Mongru, Z. N. Oltvai, and A.-L. Barabási (2002), *Hierarchical Organization of Modularity in Metabolic Networks*, Science, 297(5586):1551–1555, doi: 10.1126/science.1073374.
- Rehfeld, K., N. Molkenthin, and J. Kurths (2014), *Testing the detectability of spatio-temporal climate transitions from paleoclimate networks with the START model*, Nonlinear Processes in Geophysics, 21(3):691–703, doi: 10.5194/npg-21-691-2014.
- Reichler, T., and J. Kim (2008), *How Well Do Coupled Models Simulate Today's Climate?*, Bulletin of the American Meteorological Society, 89(3):303–311, doi: 10.1175/BAMS-89-3-303.
- Reynolds, O. (1894), *On the Dynamical Theory of Incompressible Viscous Fluids and the Determination of the Criterion*, Philosophical Transactions of the Royal Society of London, 186:123–164.
- Rheinwalt, A., N. Marwan, J. Kurths, P. Werner, and F.-W. Gerstengarbe (2012), *Boundary effects in network measures of spatially embedded networks*, Europhysics Letters, 100(2):28002, doi: 10.1209/0295-5075/100/28002.
- Rickenbach, T. M., R. N. Ferreira, J. B. Halverson, D. L. Herdies, and M. A. F. Silva Dias (2002), *Modulation of convection in the southwestern Amazon basin by extratropical stationary fronts*, Journal of Geophysical Research: Atmospheres, 107(D20):LBA 7–1–LBA 7–13, doi: 10.1029/2000JD000263.
- Ritter, B., and J.-F. Geleyn (1992), *A Comprehensive Radiation Scheme for Numerical Weather Prediction Models with Potential Applications in Climate Simulations*, Monthly Weather Review, 120(2):303–325, doi: 10.1175/1520-0493(1992)120<0303:ACRSFN>2.0.CO;2.
- Rockel, B., and B. Geyer (2008), *The performance of the regional climate model CLM in different climate regions, based on the example of precipitation*, Meteorologische Zeitschrift, 17(4):487–498, doi: 10.1127/0941-2948/2008/0297.

- Rockel, B., A. Will, and A. Hense (2008a), *The Regional Climate Model COSMO-CLM (CCLM)*, *Meteorologische Zeitschrift*, 17(4):347–348, doi: 10.1127/0941-2948/2008/0309.
- Rockel, B., C. L. Castro, S. Pielke, Roger A., H. von Storch, and G. Leoncini (2008b), *Dynamical downscaling: Assessment of model system dependent retained and added variability for two different regional climate models*, *Journal of Geophysical Research*, 113(D21):D21107, doi: 10.1029/2007JD009461.
- Rossow, W. B., and R. A. Schiffer (1999), *Advances in Understanding Clouds from ISCCP*, *Bulletin of the American Meteorological Society*, 80(11):2261–2287, doi: 10.1175/1520-0477(1999)080<2261:AIUCFI>2.0.CO;2.
- Runge, J., J. Heitzig, V. Petoukhov, and J. Kurths (2012), *Escaping the Curse of Dimensionality in Estimating Multivariate Transfer Entropy*, *Physical Review Letters*, 108:258701, doi: 10.1103/PhysRevLett.108.258701.
- Salazar, L. F., C. A. Nobre, and M. D. Oyama (2007), *Climate change consequences on the biome distribution in tropical South America*, *Geophysical Research Letters*, 34(9):L09708, doi: 10.1029/2007GL029695.
- Saleska, S. R., H. R. da Rocha, A. R. Huete, A. D. Nobre, P. Artaxo, and Y. E. Shimabukuro (2009), *LBA-ECO CD-32 Brazil Flux Network Integrated Data: 1999–2006. Data set.*, Available on-line: [<http://www.daac.ornl.gov>] from Oak Ridge National Laboratory Distributed Active Archive Center, Oak Ridge, Tennessee, U.S.A. and [<http://lba.cptec.inpe.br/>] from LBA Data and Information System, National Institute for Space Research (INPE/CPTEC), Cachoeira Paulista, São Paulo, Brazil.
- Salio, P., M. Nicolini, and E. J. Zipser (2007), *Mesoscale Convective Systems over Southeastern South America and Their Relationship with the South American Low-Level Jet*, *Monthly Weather Review*, 135(4):1290–1309, doi: 10.1175/MWR3305.1.
- Salton, G. (1989), *Automatic Text Processing: The Transformation, Analysis, and Retrieval of Information by Computer*, Addison-Wesley, Reading, MA, USA.
- Santos e Silva, C. M., S. R. de Freitas, and R. Gielow (2012), *Numerical simulation of the diurnal cycle of rainfall in SW Amazon basin during the 1999 rainy season: the role of convective trigger function*, *Theoretical and Applied Climatology*, 109(3–4):473–483, doi: 10.1007/s00704-011-0571-0.
- Saunders, P. M. (1957), *The thermodynamics of saturated air: A contribution to the classical theory*, *Quarterly Journal of the Royal Meteorological Society*, 83(357):342–350, doi: 10.1002/qj.49708335707.
- Schättler, U., G. Doms, and C. Schraff (2013), *A Description of the Nonhydrostatic Regional COSMO Model, Part VII: User's Guide*, Deutscher Wetterdienst.
- Schewe, J., J. Heinke, D. Gerten, I. Haddeland, N. W. Arnell, D. B. Clark, R. Dankers, S. Eisner, B. M. Fekete, F. J. Colón-González, S. N. Gosling, H. Kim, X. Liu, Y. Masaki, F. T. Portmann, Y. Satoh, T. Stacke, Q. Tang, Y. Wada, D. Wisser, T. Albrecht, K. Frieler, F. Piontek, L. Warszawski, and P. Kabat (2014), *Multimodel assessment of water scarcity under climate change*, *Proceedings of the National Academy of Sciences*, 111(9):3245–3250, doi: 10.1073/pnas.1222460110.

Bibliography

- Schrodin, R., and E. Heise (2001), *The multi-layer version of the DWD soil model TERRA-ML, COSMO Technical Report 2*, Deutscher Wetterdienst.
- Scott, L. S., O. Pascalis, and C. A. Nelson (2007), *A Domain-General Theory of the Development of Perceptual Discrimination*, *Current Directions in Psychological Science*, 16(4):197–201, doi: 10.1111/j.1467-8721.2007.00503.x.
- Seth, A., and M. Rojas (2003), *Simulation and Sensitivity in a Nested Modeling System for South America. Part I: Reanalyses Boundary Forcing*, *Journal of Climate*, 16(15):2437–2453, doi: 10.1175/1520-0442(2003)016<2437:SASIAN>2.0.CO;2.
- Silva Dias, M. A. F., W. Petersen, P. L. Silva Dias, R. Cifelli, A. K. Betts, M. Longo, A. M. Gomes, G. F. Fisch, M. A. Lima, M. A. Antonio, and R. I. Albrecht (2002), *A case study of convective organization into precipitating lines in the Southwest Amazon during the WETAMC and TRMM-LBA*, *Journal of Geophysical Research: Atmospheres*, 107(D20):LBA 46–1–LBA 46–23, doi: 10.1029/2001JD000375.
- Simpson, S. L., F. D. Bowman, and P. J. Laurienti (2013), *Analyzing complex functional brain networks: Fusing statistics and network science to understand the brain*, *Statistics Surveys*, 7:1–36, doi: 10.1214/13-SS103.
- Slingo, J. M. (1987), *The Development and Verification of A Cloud Prediction Scheme For the Ecmwf Model*, *Quarterly Journal of the Royal Meteorological Society*, 113(477):899–927, doi: 10.1002/qj.49711347710.
- Smagorinsky, J. (1960), *On the Dynamical Prediction of Large-Scale Condensation by Numerical Methods*, pp. 71–78, American Geophysical Union, doi: 10.1029/GM005p0071.
- Smiatek, G., B. Rockel, and U. Schättler (2008), *Time invariant data preprocessor for the climate version of the COSMO model (COSMO-CLM)*, *Meteorologische Zeitschrift*, 17(4):395–405, doi: 10.1127/0941-2948/2008/0302.
- Solman, S. A., E. Sanchez, P. Samuelsson, R. P. Rocha, L. Li, J. Marengo, N. L. Pessacg, A. R. C. Remedio, S. C. Chou, H. Berbery, H. Treut, M. Castro, and D. Jacob (2013), *Evaluation of an ensemble of regional climate model simulations over South America driven by the ERA-Interim reanalysis: model performance and uncertainties*, *Climate Dynamics*, 41(5–6):1139–1157, doi: 10.1007/s00382-013-1667-2.
- Sommeria, G., and J. W. Deardorff (1977), *Subgrid-Scale Condensation in Models of Nonprecipitating Clouds*, *Journal of the Atmospheric Sciences*, 34(2):344–355, doi: 10.1175/1520-0469(1977)034<0344:SSCIMO>2.0.CO;2.
- Spearman, C. (1904), *The Proof and Measurement of Association between Two Things*, *The American Journal of Psychology*, 15(1):72–101, doi: 10.2307/1412159.
- Spoormaker, V. I., M. S. Schröter, P. M. Gleiser, K. C. Andrade, M. Dresler, R. Wehrle, P. G. Sämann, and M. Czisch (2010), *Development of a Large-Scale Functional Brain Network during Human Non-Rapid Eye Movement Sleep*, *The Journal of Neuroscience*, 30(34):11379–11387, doi: 10.1523/JNEUROSCI.2015-10.2010.

- Stackhouse Jr., P. W., S. K. Gupta, S. J. Cox, C. Mikovitz, T. Zhang, and L. M. Hinkelman (2011), *The NASA/GEWEX surface radiation budget release 3.0: 24.5-year dataset*, *Tech. rep.*, GEWEX News, 21(1):10–12.
- Steinhaeuser, K., and A. Tsonis (2013), *A climate model intercomparison at the dynamics level*, *Climate Dynamics*, 42(5–6):1665–1670, doi: 10.1007/s00382-013-1761-5.
- Stephens, G. L. (1979), *Optical properties of eight water cloud types*, *Technical Report 36*, CSIRO, Division of Atmospheric Physics, available from Commonwealth Scientific and Industrial Research Organization, Aspendale, Vic, AU.
- Stocker, T. F., D. Qin, G. K. Plattner, M. Tignor, S. K. Allen, J. Boschung, A. Nauels, Y. Xia, V. Bex, and P. M. Midgley (Eds.) (2013), *Climate Change 2013: The Physical Science Basis. Contribution of Working Group I to the Fifth Assessment Report of the Intergovernmental Panel on Climate Change*, chap. Summary for Policymakers, pp. 1–27, Cambridge University Press, Cambridge, UK and New York, NY, USA.
- Stolbova, V., P. Martin, B. Bookhagen, N. Marwan, and J. Kurths (2014), *Topology and seasonal evolution of the network of extreme precipitation over the Indian subcontinent and Sri Lanka*, *Nonlinear Processes in Geophysics*, 21(4):901–917, doi: 10.5194/npg-21-901-2014.
- Stott, P. A., and J. A. Kettleborough (2002), *Origins and estimates of uncertainty in predictions of twenty-first century temperature rise*, *Nature*, 416(6882):723–726, doi: 10.1038/416723a.
- Sundqvist, H. (1978), *A parameterization scheme for non-convective condensation including prediction of cloud water content*, *Quarterly Journal of the Royal Meteorological Society*, 104(441):677–690, doi: 10.1002/qj.49710444110.
- Szoke, E. (2002), *A Skew-T thermodynamic diagram showing areas of positive/negative buoyancy as well as the lifted condensation level, level of free convection, and equilibrium level*, National Oceanic and Atmospheric Administration, Licensed under Public Domain via Wikimedia Commons.
- Taylor, C. M., R. A. M. de Jeu, F. Guichard, P. P. Harris, and W. A. Dorigo (2012), *Afternoon rain more likely over drier soils*, *Nature*, 489(7416):423–426, doi: 10.1038/nature11377.
- Taylor, K. E. (2001), *Summarizing multiple aspects of model performance in a single diagram*, *Journal of Geophysical Research*, 106(D7):7183–7192, doi: 10.1029/2000JD900719.
- Tetens, O. (1930), *Über einige meteorologische Begriffe*, *Zeitschrift für Geophysik*, 6:297–309.
- Thiébaux, H. J., and F. W. Zwiers (1984), *The Interpretation and Estimation of Effective Sample Size*, *Journal of Climate and Applied Meteorology*, 23(5):800–811, doi: 10.1175/1520-0450(1984)023<0800:TIAEOE>2.0.CO;2.
- Tiedtke, M. (1989), *A Comprehensive Mass Flux Scheme for Cumulus Parameterization in Large-Scale Models*, *Monthly Weather Review*, 117(8):1779–1800, doi: 10.1175/1520-0493(1989)117<1779:ACMFSF>2.0.CO;2.
- Tompkins, A. M. (2002), *A Prognostic Parameterization for the Subgrid-Scale Variability of Water Vapor and Clouds in Large-Scale Models and Its Use to Diagnose Cloud Cover*, *Journal of the Atmospheric Sciences*, 59(12):1917–1942, doi: 10.1175/1520-0469(2002)059<1917:APPFTS>2.0.CO;2.

Bibliography

- Toreti, A., P. Naveau, M. Zampieri, A. Schindler, E. Scoccimarro, E. Xoplaki, H. A. Dijkstra, S. Gualdi, and J. Luterbacher (2013), *Projections of global changes in precipitation extremes from Coupled Model Intercomparison Project Phase 5 models*, *Geophysical Research Letters*, 40(18):4887–4892, doi: 10.1002/grl.50940.
- Trenberth, K. E. (1997), *The Definition of El Niño*, *Bulletin of the American Meteorological Society*, 78(12):2771–2777, doi: 10.1175/1520-0477(1997)078<2771:TDOENO>2.0.CO;2.
- Trenberth, K. E., D. P. Stepaniak, J. W. Hurrell, and M. Fiorino (2001), *Quality of Reanalyses in the Tropics*, *Journal of Climate*, 14(7):1499–1510, doi: 10.1175/1520-0442(2001)014<1499:QORITT>2.0.CO;2.
- Tsonis, A. A., and P. J. Roebber (2004), *The architecture of the climate network*, *Physica A: Statistical Mechanics and its Applications*, 333(0):497–504, doi: 10.1016/j.physa.2003.10.045.
- Tsonis, A. A., and K. L. Swanson (2008), *Topology and Predictability of El Niño and La Niña Networks*, *Physical Review Letters*, 100:228502, doi: 10.1103/PhysRevLett.100.228502.
- Tsonis, A. A., K. L. Swanson, and P. J. Roebber (2006), *What Do Networks Have to Do with Climate?*, *Bulletin of the American Meteorological Society*, 87(5):585–595, doi: 10.1175/BAMS-87-5-585.
- van der Mheen, M., H. A. Dijkstra, A. Gozolchiani, M. den Toom, Q. Feng, J. Kurths, and E. Hernandez-Garcia (2013), *Interaction network based early warning indicators for the Atlantic MOC collapse*, *Geophysical Research Letters*, 40(11):2714–2719, doi: 10.1002/grl.50515.
- Vera, C., G. Silvestri, B. Liebmann, and P. González (2006a), *Climate change scenarios for seasonal precipitation in South America from IPCC-AR4 models*, *Geophysical Research Letters*, 33(13):L13707, doi: 10.1029/2006GL025759.
- Vera, C., W. Higgins, J. Amador, T. Ambrizzi, R. Garreaud, D. Gochis, D. Gutzler, D. Lettenmaier, J. Marengo, C. R. Mechoso, J. Nogues-Paegle, P. L. Silva Dias, and C. Zhang (2006b), *Toward a Unified View of the American Monsoon Systems*, *Journal of Climate*, 19(20):4977–5000, doi: 10.1175/JCLI3896.1.
- Vértes, P. E., A. F. Alexander-Bloch, N. Gogtay, J. N. Giedd, J. L. Rapoport, and E. T. Bullmore (2012), *Simple models of human brain functional networks*, *Proceedings of the National Academy of Sciences*, 109(15):5868–5873, doi: 10.1073/pnas.1111738109.
- Viger, F., and M. Latapy (2005), *Efficient and Simple Generation of Random Simple Connected Graphs with Prescribed Degree Sequence*, in *Computing and Combinatorics, Lecture Notes in Computer Science*, vol. 3595, edited by L. Wang, pp. 440–449, Springer Berlin Heidelberg, doi: 10.1007/11533719_45.
- von Storch, H., H. Langenberg, and F. Feser (2000), *A Spectral Nudging Technique for Dynamical Downscaling Purposes*, *Monthly Weather Review*, 128(10):3664–3673, doi: 10.1175/1520-0493(2000)128<3664:ASNTFD>2.0.CO;2.
- Žagar, N., E. Andersson, and M. Fisher (2005), *Balanced tropical data assimilation based on a study of equatorial waves in ECMWF short-range forecast errors*, *Quarterly Journal of the Royal Meteorological Society*, 131(607):987–1011, doi: 10.1256/qj.04.54.

- Žagar, N., G. Skok, and J. Tribbia (2011), *Climatology of the ITCZ derived from ERA Interim reanalyses*, Journal of Geophysical Research: Atmospheres, 116(D15):D15103, doi: 10.1029/2011JD015695.
- Wagner, S., I. Fast, and F. Kaspar (2012), *Comparison of 20th century and pre-industrial climate over South America in regional model simulations*, Climate of the Past, 8(5):1599–1620, doi: 10.5194/cp-8-1599-2012.
- Walker, G. (1928), *World Weather*, Quarterly Journal of the Royal Meteorological Society, 54(226):79–87, doi: 10.1002/qj.49705422601.
- Ward, E., W. Buytaert, L. Peaver, and H. Wheater (2011), *Evaluation of precipitation products over complex mountainous terrain: A water resources perspective*, Advances in Water Resources, 34(10):1222–1231, doi: 10.1016/j.advwatres.2011.05.007.
- Warner, T. T. (1989), *Mesoscale atmospheric modeling*, Earth-Science Reviews, 26(1–3):221–251, doi: 10.1016/0012-8252(89)90023-8.
- Warszawski, L., A. Friend, S. Ostberg, K. Frieler, W. Lucht, S. Schaphoff, D. Beerling, P. Cadule, P. Ciais, D. B. Clark, R. Kahana, A. Ito, R. Keribin, A. Kleidon, M. Lomas, K. Nishina, R. Pavlick, T. T. Rademacher, M. Buechner, F. Piontek, J. Schewe, O. Serdeczny, and H. J. Schellnhuber (2013), *A multi-model analysis of risk of ecosystem shifts under climate change*, Environmental Research Letters, 8(4), doi: 10.1088/1748-9326/8/4/044018.
- Washington, W. M., L. Buja, and A. Craig (2009), *The computational future for climate and Earth system models: on the path to petaflop and beyond*, Philosophical Transactions of the Royal Society of London A: Mathematical, Physical and Engineering Sciences, 367(1890):833–846, doi: 10.1098/rsta.2008.0219.
- Waugh, D. W., and V. Eyring (2008), *Quantitative performance metrics for stratospheric-resolving chemistry-climate models*, Atmospheric Chemistry and Physics, 8(18):5699–5713, doi: 10.5194/acp-8-5699-2008.
- Wechsung, F., and M. Wechsung (2014), *Dryer years and brighter sky – the predictable simulation outcomes for Germany’s warmer climate from the weather resampling model STARS*, International Journal of Climatology, doi: 10.1002/joc.4220.
- Welch, B. L. (1947), *The generalization of ‘Student’s’ problem when several different population variances are involved*, Biometrika, 34(1–2):28–35, doi: 10.1093/biomet/34.1-2.28.
- Werner, P. C., and F.-W. Gerstengarbe (1997), *Proposal for the development of climate scenarios*, Climate Research, 8:171–182, doi: 10.3354/cr008171.
- Wigley, T. M. L., and S. C. B. Raper (2001), *Interpretation of High Projections for Global-Mean Warming*, Science, 293(5529):451–454, doi: 10.1126/science.1061604.
- Wilby, R. L., and T. M. L. Wigley (1997), *Downscaling general circulation model output: a review of methods and limitations*, Progress in Physical Geography, 21(4):530–548, doi: 10.1177/030913339702100403.
- Willmott, C. J. (1981), *On the validation of models*, Physical Geography, 2(2):184–194.

Bibliography

- Wood, R., and P. R. Field (2011), *The Distribution of Cloud Horizontal Sizes*, *Journal of Climate*, 24(18):4800–4816, doi: 10.1175/2011JCLI4056.1.
- Woolley-Meza, O., D. Grady, C. Thiemann, J. P. Bagrow, and D. Brockmann (2013), *Eyjafjallajökull and 9/11: The Impact of Large-Scale Disasters on Worldwide Mobility*, *PLoS ONE*, 8(8):e69829, doi: 10.1371/journal.pone.0069829.
- Xu, C.-Y. (1999), *From GCMs to river flow: a review of downscaling methods and hydrologic modelling approaches*, *Progress in Physical Geography*, 23(2):229–249, doi: 10.1177/030913339902300204.
- Xu, J., and E. E. Small (2002), *Simulating summertime rainfall variability in the North American monsoon region: The influence of convection and radiation parameterizations*, *Journal of Geophysical Research: Atmospheres*, 107(D23):ACL 22–1–ACL 22–17, doi: 10.1029/2001JD002047.
- Yamasaki, K., A. Gozolchiani, and S. Havlin (2008), *Climate Networks around the Globe are Significantly Affected by El Niño*, *Physical Review Letters*, 100:228501, doi: 10.1103/PhysRevLett.100.228501.
- Yanai, M., S. Esbensen, and J.-H. Chu (1973), *Determination of Bulk Properties of Tropical Cloud Clusters from Large-Scale Heat and Moisture Budgets*, *Journal of the Atmospheric Sciences*, 30(4):611–627, doi: 10.1175/1520-0469(1973)030<0611:DOBPOT>2.0.CO;2.
- Zager, L. A., and G. C. Verghese (2008), *Graph similarity scoring and matching*, *Applied Mathematics Letters*, 21(1):86–94, doi: 10.1016/j.aml.2007.01.006.
- Zahn, M., and H. von Storch (2008), *A long-term climatology of North Atlantic polar lows*, *Geophysical Research Letters*, 35(22), doi: 10.1029/2008GL035769.
- Zemp, D. C., M. Wiedermann, J. Kurths, A. Rammig, and J. F. Donges (2014), *Node-weighted measures for complex networks with directed and weighted edges for studying continental moisture recycling*, *Europhysics Letters*, 107(5):58005, doi: 10.1209/0295-5075/107/58005.
- Zhang, D.-L., H.-R. Chang, N. L. Seaman, T. T. Warner, and J. M. Fritsch (1986), *A Two-Way Interactive Nesting Procedure with Variable Terrain Resolution*, *Monthly Weather Review*, 114(7):1330–1339, doi: 10.1175/1520-0493(1986)114<1330:ATWINP>2.0.CO;2.
- Zhou, C., L. Zemanová, G. Zamora, C. C. Hilgetag, and J. Kurths (2006), *Hierarchical Organization Unveiled by Functional Connectivity in Complex Brain Networks*, *Physical Review Letters*, 97:238103, doi: 10.1103/PhysRevLett.97.238103.
- Zhou, J., and K.-M. Lau (1998), *Does a Monsoon Climate Exist over South America?*, *Journal of Climate*, 11(5):1020–1040, doi: 10.1175/1520-0442(1998)011<1020:DAMCEO>2.0.CO;2.

Danksagung

Zuerst und am meisten möchte ich mich bei Jan Volkholz für die tagtägliche Betreuung während der vergangenen drei Jahre bedanken. Wir sind gemeinsam zu so einigen Konferenzen gefahren und haben am PIK durchweg im selben Büro gegessen. Jan hat mich in die Welt der Klimamodellierung eingeführt und mit dem CCLM und dessen Nutzergemeinde bekannt gemacht. Insbesondere beim wissenschaftlichen Schreiben war seine Hilfe von großem Wert. Seine Betreuung beschränkte sich aber nicht nur aufs Wissenschaftliche – vielmehr habe ich durch Gespräche mit Jan auch so einiges über das Leben im weitesten Sinne gelernt. Womöglich werden sich letztere Einsichten auf lange Sicht noch als die wichtigeren erweisen.

Jürgen Kurths danke ich für sein offenes Ohr bei der Diskussion inhaltlicher und organisatorischer Fragen sowie für seine Motivation zur Veröffentlichung und für die konstruktive Kritik der entsprechenden Manuskripte. Zudem bin ich ihm und Allen, die das IRTG 1740 geschaffen und mit Leben erfüllt haben, ausgesprochen dankbar dafür, mir und den anderen Doktoranden des Kollegs eine so interessante Promotion ermöglicht zu haben. David Hansmann sei in diesem Zusammenhang gedankt für vielfache unbürokratische Hilfe bei administrativen Problemen und für die Realisierung der wunderbaren Reise nach Manaus.

Was den erweiterten inoffiziellen Betreuerkreis betrifft, möchte ich mich bei meinen Bürokollegen Sebastian Schubert und Matthias Büchner bedanken, die insbesondere bei Modellfragen und technischen Schwierigkeiten stets unkompliziert halfen. Susanne Grossman-Clarke gebührt in diesem Zusammenhang mein Dank für umsichtige strategische Beratungen in schwierigen Lagen.

Jonathan Friedemann Donges und vor allem Jan Hendrik Feldhoff danke ich für die kollegiale Zusammenarbeit bei der Entwicklung neuer Modellevaluierungsmethoden basierend auf Klimanetzwerken. Für hervorragende Unterstützung bei konzeptionellen und technische Fragen zum CCLM danke ich den Mitgliedern der CLM-Community und insbesondere Burkhardt Rockel. Bodo Bookhagen danke ich für seinen Ideenreichtum, seine Hilfe beim Publizieren und für die freundliche Aufnahme bei meinem Besuch in Santa Barbara. Allen Organisatoren der von mir während der Promotion besuchten Konferenzen sei gedankt dafür, dass sie mir und Anderen einen ganz wichtigen Raum für wissenschaftlichen Austausch boten.

Von meinen Doktorandenkollegen möchte ich mich vor allem bei Ana Cano Crespo, Jan Hendrik Feldhoff und Delphine Zemp für erfrischend abwechslungsreiche gemeinsame Stunden am PIK, in Seminaren an der HU, in Brasilien, im Portugiesischkurs und bei zahlreichen privaten Gelegenheiten danken. Unserem Portugiesischlehrer Carlos Alberto Afonso sei gedankt für Sensibilität, zauberhaft unkonventionellen Unterricht und die Vermittlung interkultureller Erfahrungen.

Sin Chan Chou, Celso von Randow und meinen neuen Freunden aus den Reihen der Masterstudenten und Doktoranden des INPE in Cachoeira Paulista bin ich dankbar für die vielen positiven Erinnerung an meine Aufenthalte in Brasilien. Meinen Stammfrühstücks- und mittagsrunden am PIK danke ich für schöne Stunden bei Speis und Trank.

Zuletzt gebührt mein herzlicher Dank allen alten und neuen Freunden in Potsdam und Berlin, die meine Zeit hier so interessant und warm gemacht haben. Ausgesprochen dankbar bin ich außerdem meiner Familie und insbesondere meinen Eltern für den wohlwollenden Rückhalt, den sie mir während all meiner Abenteuer geben. Dieser war und bleibt ganz wichtig für mich.

Erklärung

Ich erkläre, dass ich die Dissertation selbständig und nur unter Verwendung der von mir gemäß § 7 Absatz 3 der Promotionsordnung der Mathematisch-Naturwissenschaftlichen Fakultät, veröffentlicht im Amtlichen Mitteilungsblatt der Humboldt-Universität zu Berlin Nr. 126/2014 am 18. November 2014 angegebenen Hilfsmittel angefertigt habe.

Ich habe mich nicht anderwärts um einem Doktorgrad im Promotionsfach Physik beworben und besitze keinen Doktorgrad im Promotionsfach Physik.

Die Promotionsordnung der Mathematisch-Naturwissenschaftlichen Fakultät, veröffentlicht im Amtlichen Mitteilungsblatt der Humboldt-Universität zu Berlin Nr. 126/2014 am 18. November 2014 habe ich zur Kenntnis genommen.

Potsdam, den 27. Oktober 2015

Stefan Lange